Research Square

Preprints are preliminary reports that have not undergone peer review.
They should not be considered conclusive, used to inform clinical practice,
or referenced by the media as validated information.

Real-time, macroscopic shortwave infrared Raman imaging for surgical and pre-clinical applications

Oliver Bruns

oliver.bruns@nct-dresden.de

German Cancer Research Center https://orcid.org/0000-0002-5738-0126

Bernardo Arús

German Cancer Research Center https://orcid.org/0000-0001-6132-7793

Joycelyn Yiu

NCT Dresden

Julia Barthel

NCT Dresden

Simon Härtl

National Center for Tumor Diseases https://orcid.org/0009-0007-3843-5850

Julia Correa Remus

NCT Dresden

Rudi Apolle

NCT Dresden

Jakob Lingg

Helmholtz Pioneer Campus, Helmholtz Zentrum München

Anja Hofmann

TUD Dresden University of Technology

Amy Fumo

Helmholtz Zentrum München

Honglei Ji

Helmholtz Zentrum München

Giuseppe Balsamo

NCT Dresden

Carolin Jethwa

Technical University of Munich https://orcid.org/0000-0001-5760-8242

Roy Park

Stanford University

James Henderson

Ludwig-Maximilians-Universität München

Kanuj Mishra

Institute of Biological and Medical Imaging, Helmholtz Zentrum München

Iuliia Mukha
NCT Dresden

Ke Guo
NCT Dresden

Ute Nimtschke
TUD Dresden University of Technology

Kalina Bamberger
NCT Dresden

Andre Stiel
Institute of Biological and Medical Imaging, Helmholtz Zentrum München https://orcid.org/0000-0001-8675-6797

Donato Santovito
Ludwig-Maximilians-University (LMU) Munich https://orcid.org/0000-0003-1811-4746

Christian Weber
Institute for Cardiovascular Prevention, Ludwig-Maximilians-Universität München

Christian Reeps
TUD Dresden University of Technology

Max Kemper
TUD Dresden University of Technology

Rebecca Bütof
NCT Dresden

Martin Wagner
TUD Dresden University of Technology https://orcid.org/0000-0002-9831-9110

Matthias Miederer
NCT Dresden

Maria Rohm
Helmholtz Zentrum Muenchen https://orcid.org/0000-0003-3926-1534

Alexander Bartelt
Technical University of Munich https://orcid.org/0000-0001-7840-3991

Tulio Valdez
Stanford University

Andriy Chmyrov
National Center for Tumor Diseases Dresden (NCT/UCC) https://orcid.org/0000-0003-0265-019X

Biological Sciences - Article

Keywords:

Posted Date: July 22nd, 2026

DOI: https://doi.org/10.21203/rs.3.rs-10374488/v1

License: This work is licensed under a Creative Commons Attribution 4.0 International License.
Read Full License

Additional Declarations: Yes there is potential Competing Interest. O.T.B., B.A.A., A.C., T.A.V., J.Y. and J.G.P.L. filed a patent application. The other authors declare that they have no competing interests.

Real-time, macroscopic shortwave infrared Raman imaging for surgical and pre-clinical applications

Authors: Bernardo A. Arús [1-5,*], Joycelyn Yiu [5], Julia Barthel [1-4,6], Simon Härtl [1-4], Julia C. Remus [1-4], Rudi Apolle [2-4,7], Jakob G. P. Lingg [5], Anja Hofmann [6], Amy R. Fumo [8,9], Honglei Ji [8,9], Giuseppe Balsamo [1-4], Carolin Jethwa [10-13], Roy K. Park [14], James Henderson [10,13], Kanuj Mishra [15,16], Iuliia Mukha [1-4,17], Ke Guo [1-4], Ute Nimtschke [18], Kalina Bamberger [1-4], Andre C. Stiel [15,16,19,20], Donato Santovito [10,13], Christian Weber [10,13,21], Christian Reeps [6], Max Kemper [22], Rebecca Bütof [23-25], Martin Wagner [6,26], Matthias Miederer [2-4,7], Maria Rohm [8,9], Alexander Bartelt [8-13], Tulio A. Valdez [14], Andriy Chmyrov [1-5], Oliver T. Bruns [1-5,*]

[1] Department of Functional Imaging in Surgical Oncology, National Center for Tumor Diseases (NCT/UCC); Dresden, Germany.
[2] German Cancer Research Center (DKFZ); Heidelberg, Germany.
[3] Faculty of Medicine and University Hospital Carl Gustav Carus, TUD Dresden University of Technology; Dresden, Germany.
[4] Helmholtz Zentrum Dresden-Rossendorf (HZDR); Dresden, Germany.
[5] Helmholtz Pioneer Campus, Helmholtz Zentrum München; Neuherberg, Germany.
[6] Department of Visceral, Thoracic and Vascular Surgery, Faculty of Medicine and University Hospital Carl Gustav Carus, TUD Dresden University of Technology; Dresden, Germany.
[7] Department of Translational Imaging in Oncology, National Center for Tumor Diseases (NCT/UCC); Dresden, Germany.
[8] Institute for Diabetes and Cancer (IDC), Helmholtz Zentrum München; Neuherberg, Germany.
[9] German Center for Diabetes Research (DZD); Neuherberg, Germany.
[10] Institute for Cardiovascular Prevention (IPEK), Faculty of Medicine, Ludwig-Maximilians-Universität München (LMU); Munich, Germany.
[11] Chair of Translational Nutritional Medicine, TUM School of Life Sciences, Technical University of Munich; Munich, Germany.
[12] Else Kröner Fresenius Center for Nutritional Medicine, Technical University of Munich; Munich, Germany.
[13] German Center for Cardiovascular Research (DZHK), Partner Site Munich Heart Alliance; Munich, Germany.
[14] Department of Otolaryngology, Head and Neck Surgery, Stanford University; Palo Alto, CA, USA.
[15] Institute of Biological and Medical Imaging, Helmholtz Zentrum München; Neuherberg, Germany.
[16] Chair of Biological Imaging, Central Institute for Translational Cancer Research (TranslaTUM), School of Medicine and Health & School of Computation, Information and Technology, Technical University of Munich, Munich, Germany.
[17] L. V. Pisarzhevskii Institute of Physical Chemistry, National Academy of Science of Ukraine; Kyiv, Ukraine.
[18] Institute of Anatomy, Faculty of Medicine and University Hospital Carl Gustav Carus, TUD Dresden University of Technology; Dresden, Germany.
[19] Faculty of Biology and Pre-Clinical Medicine, University of Regensburg; Regensburg, Germany.
[20] Regensburg Center for Ultrafast Nanoscopy, University of Regensburg; Regensburg, Germany.
[21] Munich Cluster for Systems Neurology (SyNergy); Munich, Germany.
[22] Department of Otolaryngology, Head and Neck Surgery, Faculty of Medicine and University Hospital Carl Gustav Carus, TUD Dresden University of Technology; Dresden, Germany.

[23] OncoRay – National Center for Radiation Research in Oncology, Faculty of Medicine and University Hospital Carl Gustav Carus, TUD Dresden University of Technology; Dresden, Germany.
[24] Helmholtz-Zentrum Dresden-Rossendorf, Institute of Radiooncology – OncoRay; Dresden, Germany.
[25] National Center for Tumor Diseases (NCT/UCC); Dresden, Germany.
[26] Centre for Tactile Internet with Human-in-the-Loop (CeTI), TUD Dresden University of Technology; Dresden, Germany.
*Corresponding authors. Emails: bernardo.arus@nct-dresden.de, oliver.bruns@nct-dresden.de.

Summary paragraph: Optical imaging has transformed biomedical research and clinical practice by revealing tissue identity and function in living organisms and during surgery. In the shortwave infrared (SWIR, 1000-1700 nm), biological tissues exhibit lower scattering and autofluorescence, properties that improve penetration depth and image contrast. Raman scattering imaging is a label-free optical technique that provides chemical information across a wide range of applications, particularly at microscopic and mesoscopic scales. In biological tissues, however, macroscopic Raman imaging has remained challenging because, at visible and near-infrared wavelengths, autofluorescence overwhelms the weak Raman signals. Here we integrate the favorable optical properties of SWIR with the specificity of Raman scattering to establish SWIR Raman imaging for real-time, high-contrast chemical imaging across surgically relevant fields of view. We demonstrate its versatility by monitoring tissue dynamics in living animals, detecting fatty liver disease non-invasively in mice, and identifying calcification and lipids in human atherosclerotic plaques. In surgical settings, SWIR Raman reveals lymph nodes and nerves that are invisible otherwise, providing magnetic-resonance-imaging-like anatomical information directly in the operation field for real-time surgical guidance. SWIR Raman thereby expands the capabilities of optical imaging to applications requiring rapid biochemical identification over large tissue areas and can improve surgical decision-making and patient outcomes.

Main

Biomedical imaging in the shortwave infrared (SWIR) range of 1000 to 1700 nm has rapidly expanded over the past decade, primarily due to its significant optical advantages over the visible (400 to 700 nm) and near-infrared (700 to 1000 nm) regions [1,2]. This wide adoption was made possible by advances and increased availability of novel SWIR-detecting technology. In biological tissues, SWIR imaging offers deeper penetration, reduced autofluorescence, stronger contrast, and higher resolution compared to other optical windows [3,4]. These benefits are particularly evident in animal and clinical studies that compare the SWIR emission tail of indocyanine green, a clinically approved fluorophore, with its near-infrared peak [5-10]. Contrast agent-based approaches utilize these photophysical properties for a number of applications, including multiplexed fluorescence-guided surgery with tumor delineation [11], small metastasis detection [12], blood flow mapping [13,14], high-resolution vascular imaging through mouse skin and skull [15], and multiplexed tissue imaging in freely moving animals [16]. Furthermore, SWIR imaging has demonstrated label-free applications by detecting middle ear pathologies [17,18] and cerebrospinal fluid leaks [19] based on water absorptivity, and monitoring liver disease through endogenous lipofuscin autofluorescence [20,21].

Raman scattering imaging is a well-established label-free technique used to analyze chemical composition in various materials, including biological tissues [22-24]. Coherent and spontaneous Raman methods have demonstrated remarkable capabilities for molecular characterization of tissues and cells in both clinical and pre-clinical settings [25-29]. However, these techniques are predominantly implemented as point- or line-scanning approaches, including fiber probes for *in vivo* interrogation, which maximize signal collection and chemical contrast but limit coverage to small areas [30]. While scanning can be extended to larger fields of view by tiling or raster scanning, an inherent speed-area-resolution trade-off limits practical coverage: areas relevant to surgical or whole-animal applications demand acquisition times of several minutes to tens of minutes, and most approaches require direct tissue contact [31-33]. Wide-field spontaneous Raman imaging can overcome these limitations by acquiring all spatial positions simultaneously from a distance, but conventional near-infrared approaches are fundamentally hindered by tissue autofluorescence, which overwhelms chemical contrast [30,34-36]. Overcoming this barrier would enable comprehensive

chemical analysis of heterogeneous tissues across large fields of view in seconds or less, paving the way for novel applications in whole-body pre-clinical studies and intraoperative guidance [37,38].

Here, we introduce a wide-field SWIR imaging approach that visualizes spontaneous Raman scattering over fields of view approaching 100 cm², at exposure times as short as 0.1 s per Raman channel. By using illumination wavelengths between 892 and 1064 nm, our approach overcomes previous autofluorescence limitations and offers unprecedented chemical contrast without autofluorescence subtraction or spectral unmixing. We showcase the ability of SWIR Raman to non-invasively monitor dynamic physiological and pathological tissue remodeling in mouse models and human tissue. Most notably, we demonstrate the potential of SWIR Raman imaging for intraoperative guidance by enhancing the visibility of low-contrast anatomical structures, such as lymph nodes and nerves embedded in adipose tissue, validated in a living pig and in a human body donor under standard operating room conditions.

Design and *in vitro* validation of wide-field macroscopic SWIR Raman imaging

To image macroscopic spontaneous Raman scattering in the SWIR spectral region, we designed a straightforward imaging system that comprises components similar to those detecting SWIR fluorescence [39]. Raman imaging was achieved by diffusely illuminating the sample with specific wavelengths and filtering the scattered light with narrow band-pass filters (**Figure 1 a**). These filters selectively captured the scattered wavelengths corresponding to the Raman shifts of interest, which were determined as a combination of the illumination wavelength and the wavelength corresponding to the energy shift of specific bonds, according to

$$\lambda[nm] = \frac{1}{\frac{1}{\lambda_{illumination}[nm]} - \frac{Raman\ shift\ [cm^{-1}]}{10^7}}. \qquad (1)$$

As an example, upon 892 nm illumination, the Raman scattering of the CH region between 2800 and 3100 cm^{-1} shifts to the region between 1189 and 1233 nm, while that of the OH region between 3200 and 3600 cm^{-1} shifts to the region between 1248 and 1314 nm (**Figure 1 b** and **Fig. S 1**).

To illustrate and validate the ability of our system to detect specific Raman scattering from different compounds, we imaged water and olive oil, which were spectrally distinguished according to their Raman scattering shifts in the CH and OH regions, respectively (**Figure 1 b** and **Fig. S 1**). By using 892-nm light and sequentially imaging one frame with a narrow band-pass filter selective for the CH region and a second frame with a filter selective for the OH region, we clearly distinguished olive oil and water based on their chemical contrast on a two-phase mixture in a polypropylene tube (**Figure 1 c**). This approach was extended to other illumination wavelengths and Raman bands, including the fingerprint region, enabling the distinction among hydroxyapatite, proteins and lipids after 1064 nm illumination, based on respective Raman scattering in the PO_4^{-3} (imaged between 888 and 1065 cm^{-1}), amide I (imaged between 1555 and 1706 cm^{-1}), and CH region (**Fig. S 2** and **Fig. S 3**). These findings corroborate that SWIR Raman imaging effectively captures distinct chemical components in a wide-field configuration, akin to a straightforward wide-field fluorescence setup. By selecting specific illumination wavelengths and detection filter combinations, chemical contrast is achieved within single frames, with the only necessary image processing being dark current correction.

Throughout this work, two implementations of this imaging concept were employed. The primary system was optimized for maximum signal-to-noise ratio (SNR), using a large-format stationary detector with exposure times of 10-300 s per channel. For intraoperative applications, we

developed a compact, portable implementation designed for real-time acquisition under standard operating-room conditions, capable of delivering a merged dual-channel frame at ~1 fps with 0.1 s per channel exposure. A critical engineering requirement shared by both systems was the suppression of laser stray light to a level significantly below the Raman signal; we estimated that the filter stack must provide a minimum effective optical density of 16-18 to block laser light. The design rationale and technical specifications of both systems are described in the Methods section.

Chemical contrast imaging through skin in whole mice and human hands

Building on the ability to visualize high-contrast Raman scattering across large fields of view in single-frame acquisitions, we investigated whole-body chemical contrast in mice. Through intact skin, fat depots and the xiphoid cartilage, located below the sternum, exhibited strong CH-band contrast, while OH-band signal was distributed throughout the entire body (**Figure 1 d** and **Fig. S 4**). Dissection confirmed both findings: CH contrast followed the subcutaneous fat pads, while OH signal persisted body-wide after skin removal (**Fig. S 5**). Furthermore, subcutaneous lymph nodes were clearly discernible from their surrounding fat pads both in excised tissue (**Fig**. **S 5)** and intact mice (**Fig. S 6**).

CH and OH vibrational modes are present across all biological tissues, and each channel reflects the absolute Raman signal intensity of the corresponding band. In the green-blue pseudocolor composite, the strongest contributor to each channel dominates the perceived contrast: fat pads appear green due to their strong CH signal, while lymph nodes and muscle appear blue because of their relatively stronger OH contribution, consistent with their higher water content (**Supplementary Note 2**). The composite image therefore reveals the dominant tissue composition within the field of view, not the exclusive presence of a molecular class, which is evident in the single-channel images.

Crucially, this chemical contrast distinctly stood out from background autofluorescence, which we imaged by selecting a filter in the Raman-silent region (**Figure 1 d** and **Fig. S 4**). Autofluorescence showed higher signal in skeletal bone, liver, intestine, and skin areas rich in pigmentation, consistent with previous reports [40]. The Raman origin of the image contrast was confirmed by *in vivo* spectroscopy (**Fig. S 7** and **Fig. S 8**).

Moreover, SWIR Raman imaging enabled the visualization of chemical contrast through human skin. We visualized subcutaneous fat pads on the dorsal surface of the hand and fingers by their CH Raman signal, while the OH Raman band highlighted the extensor tendons and adjacent dorsal interossei muscles of the hand (**Figure 1 e-f** and **Fig. S 9**). Notably, the Raman contrast of these structures was observed at depths in the approximate range between 2 and 4 mm below the skin surface (**Supplementary Note 3**). In contrast, autofluorescence predominantly manifested in the skin surface creases.

The sensitivity of the imaging system, assessed by a limit-of-detection analysis using serial dilutions of a lipid emulsion, yielded a detection threshold of ~350 µM for triglycerides (**Fig. S 10**). This concentration (0.015% v/v) is well below the lipid concentrations found even in lipid-poor tissues such as blood, spleen, and muscle, which contain on the order of 0.6-1% lipids [41].

These initial findings highlight the capability of SWIR Raman imaging to non-invasively identify biological tissues based on chemical contrast through skin without contrast agent administration. Importantly, these results were obtained with diffuse illumination within the international laser

safety limits [42], underscoring the compatibility of SWIR Raman imaging with *in vivo* applications in both animal models and humans.

SWIR Raman provides similar contrast to MRI

To represent the relative CH-to-OH balance in a single grayscale image, we calculated a weighted CH/OH ratio (**Fig. S 11**). We validated this contrast cross-modally with magnetic resonance imaging (MRI), acquiring chemically selective fat maps in both mice and humans. Because the wide-field geometry of our imaging approach integrates signal across multiple tissue layers rather than resolving individual slices, we applied a depth-weighted projection to the MRI coronal slices to generate 2D fat maps comparable to the Raman field of view (see Methods section).

In freshly euthanized mice, CH/OH ratio-bright regions aligned spatially with MRI-defined fat depots across the whole body (**Fig. S 12 a-b**). Similarly, in the human hand, the SWIR Raman CH/OH contrast matched the distribution of MRI-defined subcutaneous fat across the dorsal hand (**Fig. S 12 c-e** and **Supplementary Note 3**). This spatial agreement was further supported by line-profile comparisons at anatomically equivalent locations, with Raman-positive regions consistently overlapping with the MRI signal (**Fig. S 13**). Minor residual mismatches between modalities likely reflect small differences in hand positioning between imaging setups, as well as MRI-related immobilization using sandbags, which may have subtly altered superficial vascular appearance. Together, these results support that SWIR Raman imaging generates tissue-compositional contrast similar to MRI.

Dominance of Raman scattering as tissue background at ≥892 nm illumination

To understand the influence of different illumination wavelengths on chemical contrast in tissues and determine their advantages and limitations, we acquired SWIR Raman images from intact mice illuminated from 785 nm, a commonly used wavelength in Raman imaging, to 1064 nm. Our findings revealed that the chemical contrast, particularly that of the CH region in adipose tissue fat depots, became stronger than autofluorescence once the illumination wavelength reached 892 nm, and continued to rise up to 1064 nm (**Figure 2 a-e**, **Fig. S 14** and **Fig. S 15**). *In vivo* spectral measurements further verified these findings, showing that longer excitation wavelengths suppress autofluorescence while enhancing the relative contribution of the CH- and OH-band Raman signals (**Fig. S 8**, **Fig. S 16** and **Fig. S 17**). Mouse skin pigmentation represents a notable exception: even at 938 nm, pigmented patches remained a major source of background, affecting Raman contrast in affected regions (**Supplementary Note 4**).

This increase in Raman-based contrast was evident even when using long-pass filters capturing the Raman-silent region within the same frame, highlighting that the enhancement in chemical contrast at longer illumination effectively overcomes the contribution of autofluorescence even within non-specific broad imaging bands (**Fig. S 18)**. However, longer wavelengths required slower imaging frame rates, emphasizing the need to balance contrast and acquisition speed according to specific application requirements.

Non-invasive SWIR Raman imaging for chemical contrast in mouse disease models

Subsequently, we explored the application of SWIR Raman imaging to non-invasively visualize changes in body composition at the whole-body level in preclinical mouse models. To detect adipose tissue phenotypes, we first imaged genetically obese mice (*ob*/*ob*), which are hyperphagic due to the lack of the satiety hormone leptin, resulting in up to a threefold increase in body weight

compared to age-matched controls [43]. The abundance of adipose tissue fat depots throughout their bodies was highlighted by Raman CH region contrast (**Figure 3 a** and **Fig. S 19**).

Next, we assessed the potential of SWIR Raman imaging for the non-invasive chemical contrast detection of liver steatosis, which is characterized by lipid accumulation in the liver. The label- and contact-free detection of liver steatosis is essential for monitoring liver disease progression, such as metabolic dysfunction-associated steatotic liver disease (MASLD, also called non-alcoholic fatty liver disease, NAFLD), and evaluating treatment effectiveness [44]. We applied our method to visualize MASLD-associated tissue changes induced by a methionine and choline-deficient (MCD) diet [45,46] by conducting macroscopic SWIR Raman imaging of mice following a six-week feeding period. Through intact skin, we detected stronger Raman CH intensity in the livers of the mice fed the MCD diet than in littermates fed a normal diet (**Figure 3 b-d** and **Fig. S 20, Fig. S 21, Fig. S 22**). These findings demonstrate the potential of SWIR Raman imaging as a valuable tool for whole-body, non-invasive monitoring of tissue composition changes during the progression of diseases such as MASLD.

In vivo monitoring of tissue dynamics with whole-body SWIR Raman imaging in mice

Turning to *in vivo* applications, we utilized SWIR Raman imaging to longitudinally monitor tissue dynamics in living mice, showcasing its non-invasive and label-free properties. We explored the ability of our system to track *in vivo* body composition changes in mice exposed to fasting, a process known to swiftly mobilize adipose tissue fat depots, which typically replenish within 48 hours of refeeding [47,48]. Notably, we observed a strong reduction in Raman CH region scattering from adipose tissues following a 24-hour fasting period, which was reversed within 48 h of refeeding (**Figure 3 e** and **Fig. S 23**).

To expand its utilization for longitudinal visualization of whole-body tissue dynamics, we employed SWIR Raman imaging to monitor tissue modifications during tumor growth. To accomplish this, we tracked the development of 4T1 breast cancer cell xenografts implanted subcutaneously in mice. Imaging conducted over a 9-day period after tumor cell implantation revealed tumor-associated edema, distinguishable by OH contrast against the surrounding CH contrast of adipose tissue (**Fig. S 24** and **Fig. S 25**).

Combining SWIR Raman with fluorescence imaging

Furthermore, to validate the orthogonality of SWIR Raman imaging in conjunction with traditional fluorescence for *in vivo* studies, we implanted mice with 4T1 cells engineered to express the fluorescent protein iRFP720. While its emission peak is in the near infrared, the emission tail of iRFP720 can be detected in the SWIR [49]. This dual approach allowed us to monitor both tumor cell fluorescence and whole-body Raman scattering over time (**Fig. S 26**).

These results demonstrate the versatility of wide-field SWIR Raman imaging for monitoring physiological and pathological changes longitudinally, as well as the potential to combine this technique with fluorescence markers for comprehensive *in vivo* studies.

SWIR Raman imaging for *ex vivo* analysis of unfixed tissue composition in health and disease

We next aimed to characterize the application of our system to analyze tissue composition in freshly dissected samples *ex vivo*, a process often entailing time-consuming steps like fixation, decalcification, embedding, slicing and staining, or other procedures that may also alter tissue composition [50,51].

Firstly, we dissected organs from healthy mice, and expanded our *in vivo* findings by detecting stronger OH Raman scattering contrast in skeletal muscle, kidneys, and heart, indicating abundant water content, while contrast of the brain was particularly strong in both the CH and OH regions, reflecting the high content of both lipids and water (**Fig. S 27**). As expected, different adipose tissue fat depots exhibited high CH contrast, and the inguinal lymph nodes also exhibited chemical contrast with the adipose tissue fat depots in which they were embedded. The autofluorescence signal was consistent with the *in vivo* findings, showing stronger contribution in the liver, intestine, and pigmented skin patches. Moreover, SWIR Raman imaging distinguished gray and white matter in the porcine brain, based on their respective OH and CH intensities (**Fig. S 28** and **Fig. S 29**). Interestingly, the sulcus in the cortical regions could be differentiated from the gyrus based on their Amide I contrast.

Turning to pathological conditions, we investigated the application of the technique for measuring lipid content in unfixed tissues, which would enable direct tissue analysis while preserving its native and intact composition. Indeed, we observed stronger CH intensity, indicative of higher lipid content, in livers from genetically obese mice (**Fig. S 30**), as well as from wild-type mice fed either a MCD diet (**Figure 4 a-c** and **Fig. S 31**), or a high-fat diet known to induce obesity and liver steatosis (**Fig. S 32 a-b**). Notably, we successfully imaged up to 24 liver samples from different mice in a single frame, demonstrating the high-throughput capability of SWIR Raman for macroscopic detection of lipid content in unprocessed tissues.

Atherosclerosis is an inflammatory disease prompted by abnormalities in lipoprotein metabolism and characterized by accumulation of lipids and inflammatory cells in the vessel wall [52,53]. Analyzing atherosclerotic plaques presents challenges, as important components for atherosclerosis scoring and risk stratification, such as calcified areas and accumulated lipids, can be lost during sample preparation for traditional histological analysis [54]. To complement microscopic histological assessment, we employed SWIR Raman imaging to visualize heterogeneous tissue composition in unfixed human plaques. Utilizing excised atherosclerotic tissue from carotid or femoral arteries obtained from patients during eversion thromboendarterectomy, we targeted the PO_4^{-3} Raman peak at 960 cm^{-1} to detect atherosclerotic plaque calcification and the CH region to detect lipids [55]. Notably, we observed distinct domains showing Raman features consistent with calcified and lipid-rich regions within plaques, without the need for tissue processing, such as fixation, decalcification, slicing and staining (**Figure 4 d-e** and **Fig. S 33**). We validated the specificity of Raman contrast for calcification by comparing imaging results before and after employing a fixation and decalcification protocol. This protocol eliminated the PO_4^{-3} signal and reduced the CH intensity (**Figure 4 f-g** and **Fig. S 34**). Moreover, the comparison between imaging of the whole biopsy vs. common histological sections revealed the insufficiency of traditional methods to capture the heterogeneity of atherosclerotic plaque composition (**Fig. S 35**).

In conclusion, our results highlight the effectiveness of SWIR Raman imaging for analyzing tissue composition in large and heterogeneous samples *ex vivo*, without the need for tissue processing while preserving its native composition.

Intraoperative surgical guidance using SWIR Raman imaging

Lymph nodes and nerves are critical structures in surgery: enough lymph nodes must be identified for accurate tumor staging [56], while nerves must be preserved to avoid devastating functional loss

[57,58]. Both structures are commonly hidden in adipose tissue and may be indistinguishable from surrounding fat under visible illumination alone. SWIR Raman imaging is well suited to this challenge, as CH- and OH-band contrast exploits the compositional difference between lipid-rich adipose tissue and the comparatively water-rich environment of lymphoid and nerve structures (**Supplementary Note 2**). Accordingly, we observed high contrast from lymph nodes embedded in fat pads in mice (**Fig. S 5** and **Fig. S 6**), and between the facial nerve and surrounding adipose tissue in a porcine model (**Fig. S 36**).

To translate this capability to the operating room, we developed a compact, real-time SWIR Raman imaging platform designed for use in open surgical environments (**Methods**). The system acquires CH- and OH-band images at 0.1 s exposure each using alternating illumination at 892 and 936 nm to shift each Raman band into a single detection window, and renders a merged frame at ~1 fps (**Fig. S 37**).

Real-time acquisition was first evaluated by imaging a freely moving, awake mouse, in which consistent CH- and OH-band contrast was observed across the body despite minor motion artifacts (**Fig. S 38** and **Supplementary Movie 1**). We then revisited facial nerve imaging as proof-of-principle in the porcine model. As adipose tissue was progressively removed, the system continuously visualized the transition from fat-covered to exposed nerve tissue (**Fig. S 39**).

To evaluate lymph node identification under realistic surgical conditions, we deployed the system on a medical arm in an operating room (**Figure 5 a-b**) and imaged post-mortem porcine tissue across two anatomical regions: head and neck and mesenteric. Tissue from the neck region was obtained from a slaughterhouse; the mesenteric specimen was imaged in situ in a freshly euthanized animal. Across all three, chemical contrast highlighted lymph nodes embedded in adipose tissue that were not visible under white-light illumination (**Figure 5 c-d**, **Fig. S 40**, **Supplementary Movie 2** and **Supplementary Movie 3**). Other OH-presenting structures, including muscle, vessels, and bowel, were macroscopically distinguishable under visible light and did not confound surgical interpretation.

We then performed intraoperative imaging in a living pig, a particularly demanding scenario given its young age (2.2 months) and lean body composition (37.1 kg), compounded by continuous respiratory motion and active peristalsis. Even under these conditions, Raman contrast readily identified mesenteric lymph nodes that were poorly visible under white light, enabling direct localization and surgical resection (**Figure 5 e**, **Fig. S 41**, **Supplementary Movie 4** and **Supplementary Movie 5**).

Extending the approach to human anatomy, lymph node identification was performed in the inguinal region of a human body donor in the same operating-room setting. SWIR Raman contrast identified the target lymph node with image quality comparable to the porcine experiments (**Figure 6**, **Fig. S 42**, **Supplementary Movie 6** and **Supplementary Movie 7**). The identity of all lymph nodes was confirmed histologically by a senior pathologist.

Taken together, these results demonstrate that SWIR Raman imaging can reveal anatomical structures that are difficult to identify under conventional surgical illumination. The technique provides real-time chemical contrast over fields of view relevant to surgical procedures, without exogenous contrast agents, and under standard operating-room conditions. These findings

establish wide-field SWIR Raman imaging as a practical strategy for intraoperative identification of critical anatomical structures and a promising platform for label-free surgical guidance.

Discussion

In this work, we unveil a novel Raman scattering-based imaging method that delivers high chemical contrast across a wide field of view (~100 cm^2) in just 0.1 s, without autofluorescence subtraction or spectral unmixing. Our findings reveal that Raman scattering-based chemical contrast overcomes autofluorescence when tissues are illuminated with wavelengths of 892 nm and longer. This suggests that wide-field Raman imaging should employ these wavelengths for optimal chemical contrast, thereby requiring SWIR Raman scattering detection. In addition to autofluorescence suppression, SWIR Raman imaging capitalizes on the optical benefits inherent to this wavelength range, such as deeper tissue penetration and stronger imaging contrast [2,3]. The illumination irradiances used throughout this work fall within established laser safety limits for non-ionizing radiation [42], an important consideration for translation toward clinical use.

While it is conventionally conceived that spontaneous Raman detection requires long exposure times [30], our results show that meaningful chemical contrast can be achieved at exposure times as short as 0.1 s per channel with sufficient signal-to-noise ratio (SNR) to identify relevant anatomical structures in surgical scenarios with minimal motion artifacts. While the bulk of this work employed a stationary large-format camera in an enclosed dark environment with exposure times of 10-300 s per channel to maximize SNR for the system's characterization, we further developed a compact real-time platform rendering two-channel images at ~ 1 fps, without dark-room requirements. The physical plausibility of detecting the inherently low photon flux of spontaneous Raman scattering under wide-field illumination is supported by a photon-budget model (**Supplementary Note 5**). Employing more sensitive SWIR detectors, which are currently being developed, will enable even higher SNR and could achieve video-rate exposure times.

The ability of SWIR Raman to image live and unfixed tissues with chemical contrast has significant implications for both pre-clinical and clinical settings. Compared to conventional modalities, like MRI, computed tomography (CT), and ultrasound [59-61], SWIR Raman imaging offers distinctive advantages. CT and ultrasound provide anatomical information but lack chemical contrast. In turn, MRI can provide fat/water contrast, but requires magnetic fields, large infrastructure, and specialized facilities. Notably, cross-modal validation against MRI fat maps, acquired in both mice and humans, showed that the SWIR Raman CH/OH ratio spatially recapitulates MRI-defined fat depots, demonstrating that equivalent tissue-compositional contrast can be obtained with a compact optical system. Unlike intraoperative MRI, which interrupts the surgical procedure and requires magnetic precautions for instruments [62], SWIR Raman setups require no specialized facilities and can be used for guidance directly at the surgical table, being compatible with standard workflows. Its optical configuration is akin to fluorescence imaging, a well-established modality in surgery [63], which should facilitate its clinical translation. These characteristics will facilitate the implementation of SWIR imaging in peri- and intraoperative settings in the future.

SWIR Raman imaging not only broadens the applications of Raman imaging to the macroscopic scale, but also expands the overall capabilities of biomedical imaging. By remaining orthogonal to classical fluorescence imaging, this straightforward approach supports multimodal strategies, thereby opening new avenues for pre-clinical and clinical applications. In surgical settings, the technique identified lymph nodes and nerves concealed within fatty tissue and invisible under

white-light illumination. Accurate lymph node identification improves tumor staging; nerve preservation prevents devastating functional loss. SWIR Raman imaging addresses both – in real time, without exogenous agents – holding direct promise for improving patient outcomes.

Acknowledgments: The authors thank Dr. Thomas Bischof for critical discussions related to this manuscript, Martin Warmer for help in setting up hardware, Hannes Rolbieski for assistance with animal handling and tumor cell culture, Vivien William for mouse MRI data acquisition, Pamela Sabarstinski for processing of arterial biopsies, Dr. Anke Witt and Antje Weißenberger for organization of the experimental operating room at NCT/UCC Dresden and assistance with porcine experiments, and Dr. Mirko Schmidt from the Institute of Anatomy at the TUD Dresden University of Technology for access to human body donor material. The authors also thank Dr. Georg Heinrich Klose from the Institute of Pathology at the University Hospital Carl Gustav Carus for performing the histological analysis.

Funding:

Helmholtz Zentrum München core funding (O.T.B)

National Center for Tumor Diseases (NCT) core funding (O.T.B)

Deutsche Forschungsgemeinschaft (DFG) Emmy Noether program no. BR 5355/2-1 (O.T.B)

German Federal Ministry of Education and Research (BMBF) project BetterView (O.T.B)

National Center for Tumor Diseases (NCT) PoC grant project SATISFIES (O.T.B)

Helmholtz Imaging Project grant ZT-I-PF-4-038 (O.T.B)

Chan Zuckerberg Initiative (CZI) Deep Tissue Imaging grants DTI0000000248 and DTI2-0000000206 (O.T.B, A.C.)

Deutsche Forschungsgemeinschaft (DFG) SFB1123-B10 (O.T.B., A.B.)

Deutsche Forschungsgemeinschaft (DFG) SPP2306 BA4925/2-1 (A.B.)

Deutsches Zentrum für Herz-Kreislauf-Forschung (DZHK) (A.B.)

European Research Council (ERC) Starting Grant PROTEOFIT (A.B.)

Else Kröner Fresenius Stiftung (A.B.)

European Research Council (ERC) under the European Union's Horizon 2020 research and innovation program # 101002646 (Switch2See) (A.C.S.)

European Research Council (ERC) under the European Union's Horizon 2020 research and innovation program # 101046667 (SWOPT) (A.C.S.)

Deutsche Forschungsgemeinschaft (DFG) GZ: STI 656/1-1 (Sorting Sounds) (A.C.S., K.M.)

Deutsche Forschungsgemeinschaft (DFG) SFB1123-B5 (D.S.)

Bundesministerium für Bildung und Forschung (BMBF) (D.S.)

Free State of Bavaria (LMU Excellence strategy) (D.S.)

German Centre for Cardiovascular Research (DZHK) grants 81Z0600203 and 81X2600269 (D.S.)

European Research Council (ERC) under the European Union's Horizon 2020 research and innovation program # 949017 (M.R.)

Helmholtz Association - Initiative and Networking Fund (M.R.)

EFSD/Novo Nordisk Foundation Future Leaders Award (M.R.)

German Research Foundation (DFG, Deutsche Forschungsgemeinschaft) as part of Germany's Excellence Strategy – EXC 2050/2 – Project ID 390696704 – Cluster of Excellence "Centre for Tactile Internet with Human-in-the-Loop" (CeTI) of TUD Dresden University of Technology (M.W.)

European Stroke Research Foundation (ESRF) (A.H., C.R.)

Philipp Schwartz Initiative of the Alexander von Humboldt Foundation (I.M.)

Joachim Herz Foundation (J.G.P.L)

Author contributions: B.A.A., A.C. and O.T.B. conceived and designed the study, which T.A.V. helped to guide. B.A.A. and J.Y. performed imaging experiments. J.G.P.L. built the customized spectrometer setup, while B.A.A., J.Y., J.G.P.L., I.M and K.B. performed spectroscopic measurements. A.H., J.H., D.S., C.W. and C.R. provided clinical arterial biopsies and histology, while C.J., H.J., A.R.F., M.R., M.K., R.K.P., T.A.V. and A.B. provided other biological samples. J.B. performed the porcine and human body donor surgeries. M.W. coordinated the porcine surgeries, while U.N. coordinated the body donor experiment. S.H. and J.C.R. developed the software for real-time imaging. G.B. processed and prepared samples for histological analysis. R.A. and M.M. designed and executed the human MRI validation, including acquisition protocols and image processing. R.B. provided guidance for mouse MRI data acquisition. K.G. performed the theoretical modeling. K.M. and A.C.S. engineered the 4T1-iRFP720 cell line. I.M. and B.A.A. designed the illustrations. B.A.A., A.B., A.C. and O.T.B. drafted the manuscript, to which all authors contributed. All authors approved the submitted version.

Competing interests: O.T.B., B.A.A., A.C., T.A.V., J.Y. and J.G.P.L. filed a European patent application. The other authors declare that they have no competing interests.

Data and materials availability: All data are available in the main text or the supplementary materials.

References

1 Schmidt, E. L. *et al.* Near-infrared II fluorescence imaging. *Nature Reviews Methods Primers* **4**, 23 (2024). https://doi.org/10.1038/s43586-024-00301-x

2 Wang, F., Zhong, Y., Bruns, O., Liang, Y. & Dai, H. In vivo NIR-II fluorescence imaging for biology and medicine. *Nature Photonics* (2024). https://doi.org/10.1038/s41566-024-01391-5

3 Carr, J. A. *et al.* Absorption by water increases fluorescence image contrast of biological tissue in the shortwave infrared. *Proc Natl Acad Sci U S A* **115**, 9080-9085 (2018). https://doi.org/10.1073/pnas.1803210115

4 Cosco, E. D. *et al.* Shortwave infrared polymethine fluorophores matched to excitation lasers enable non-invasive, multicolour in vivo imaging in real time. *Nature chemistry* **12**, 1123-1130 (2020). https://doi.org/10.1038/s41557-020-00554-5

5 Hu, Z. *et al.* First-in-human liver-tumour surgery guided by multispectral fluorescence imaging in the visible and near-infrared-I/II windows. *Nat Biomed Eng* **4**, 259-271 (2020). https://doi.org/10.1038/s41551-019-0494-0

6 Carr, J. A. *et al.* Shortwave infrared fluorescence imaging with the clinically approved near-infrared dye indocyanine green. *Proc Natl Acad Sci U S A* **115**, 4465-4470 (2018). https://doi.org/10.1073/pnas.1718917115

7 Wu, Y. *et al.* First clinical applications for the NIR-II imaging with ICG in microsurgery. *Front Bioeng Biotechnol* **10**, 1042546 (2022). https://doi.org/10.3389/fbioe.2022.1042546

8 Wang, F. *et al.* Guiding esophagectomy with intraoperative NIR-II fluorescence video imaging and rapid computation. *Proc Natl Acad Sci U S A* **122**, e2517785122 (2025). https://doi.org/10.1073/pnas.2517785122

9 Mi, J. *et al.* Comparative Study of Indocyanine Green Fluorescence Imaging in Lung Cancer with Near-Infrared-I/II Windows. *Ann Surg Oncol* **31**, 2451-2460 (2024). https://doi.org/10.1245/s10434-023-14677-9

10 Cao, C. *et al.* First Clinical Investigation of Near-Infrared Window IIa/IIb Fluorescence Imaging for Precise Surgical Resection of Gliomas. *IEEE Trans Biomed Eng* **69**, 2404-2413 (2022). https://doi.org/10.1109/TBME.2022.3143859

11 Bandi, V. G. *et al.* Targeted multicolor in vivo imaging over 1,000 nm enabled by nonamethine cyanines. *Nat Methods* **19**, 353-358 (2022). https://doi.org/10.1038/s41592-022-01394-6

12 Wang, P. *et al.* NIR-II nanoprobes in-vivo assembly to improve image-guided surgery for metastatic ovarian cancer. *Nat Commun* **9**, 2898 (2018). https://doi.org/10.1038/s41467-018-05113-8

13 Bruns, O. T. *et al.* Next-generation in vivo optical imaging with short-wave infrared quantum dots. *Nat Biomed Eng* **1** (2017). https://doi.org/10.1038/s41551-017-0056

14 Wang, F. *et al.* Light-sheet microscopy in the near-infrared II window. *Nat Methods* (2019). https://doi.org/10.1038/s41592-019-0398-7

15 Hong, G. *et al.* Through-skull fluorescence imaging of the brain in a new near-infrared window. *Nat Photonics* **8**, 723-730 (2014). https://doi.org/10.1038/nphoton.2014.166

16 Arús, B. A. *et al.* Shortwave infrared fluorescence imaging of peripheral organs in awake and freely moving mice. *Front Neurosci* **17**, 1135494 (2023). https://doi.org/10.3389/fnins.2023.1135494

17 Carr, J. A., Valdez, T. A., Bruns, O. T. & Bawendi, M. G. Using the shortwave infrared to image middle ear pathologies. *Proc Natl Acad Sci U S A* **113**, 9989-9994 (2016). https://doi.org/10.1073/pnas.1610529113

18 Valdez, T. A. *et al.* Initial findings of shortwave infrared otoscopy in a pediatric population. *International journal of pediatric otorhinolaryngology* **114**, 15-19 (2018). https://doi.org/10.1016/j.ijporl.2018.08.024

19 Klein, T. W. *et al.* Development of a shortwave infrared sinuscope for the detection of cerebrospinal fluid leaks. *J Biomed Opt* **28**, 094803 (2023). https://doi.org/10.1117/1.JBO.28.9.094803

20 Saif, M. *et al.* Non-invasive monitoring of chronic liver disease via near-infrared and shortwave-infrared imaging of endogenous lipofuscin. *Nat Biomed Eng* **4**, 801-813 (2020). https://doi.org/10.1038/s41551-020-0569-y

21 He, H. *et al.* Label-free tissue NIR-II autofluorescence imaging for visualization of human liver malignancy. *Nat Biomed Eng* (2026). https://doi.org/10.1038/s41551-025-01593-4

22 Cialla-May, D., Schmitt, M. & Popp, J. Theoretical principles of Raman spectroscopy. *Physical Sciences Reviews* **4** (2019). https://doi.org/doi:10.1515/psr-2017-0040

23 Hu, F., Shi, L. & Min, W. Biological imaging of chemical bonds by stimulated Raman scattering microscopy. *Nat Methods* **16**, 830-842 (2019). https://doi.org/10.1038/s41592-019-0538-0

24 Butler, H. J. *et al.* Using Raman spectroscopy to characterize biological materials. *Nat Protoc* **11**, 664-687 (2016). https://doi.org/10.1038/nprot.2016.036

25 Freudiger, C. W. *et al.* Label-free biomedical imaging with high sensitivity by stimulated Raman scattering microscopy. *Science* **322**, 1857-1861 (2008). https://doi.org/10.1126/science.1165758

26 Orringer, D. A. *et al.* Rapid intraoperative histology of unprocessed surgical specimens via fibre-laser-based stimulated Raman scattering microscopy. *Nat Biomed Eng* **1** (2017). https://doi.org/10.1038/s41551-016-0027

27 Kong, K., Kendall, C., Stone, N. & Notingher, I. Raman spectroscopy for medical diagnostics--From in-vitro biofluid assays to in-vivo cancer detection. *Adv Drug Deliv Rev* **89**, 121-134 (2015). https://doi.org/10.1016/j.addr.2015.03.009

28 Palonpon, A. F. *et al.* Raman and SERS microscopy for molecular imaging of live cells. *Nat Protoc* **8**, 677-692 (2013). https://doi.org/10.1038/nprot.2013.030

29 Nicolson, F., Kircher, M. F., Stone, N. & Matousek, P. Spatially offset Raman spectroscopy for biomedical applications. *Chem Soc Rev* **50**, 556-568 (2021). https://doi.org/10.1039/d0cs00855a

30 Krafft, C., Schie, I. W., Meyer, T., Schmitt, M. & Popp, J. Developments in spontaneous and coherent Raman scattering microscopic imaging for biomedical applications. *Chem Soc Rev* **45**, 1819-1849 (2016). https://doi.org/10.1039/c5cs00564g

31 Thomas, G. *et al.* Evaluating feasibility of an automated 3-dimensional scanner using Raman spectroscopy for intraoperative breast margin assessment. *Sci Rep* **7**, 13548 (2017). https://doi.org/10.1038/s41598-017-13237-y

32 Daoust, F. *et al.* Handheld macroscopic Raman spectroscopy imaging instrument for machine-learning-based molecular tissue margins characterization. *J Biomed Opt* **26** (2021). https://doi.org/10.1117/1.JBO.26.2.022911

33 Mosca, S., Conti, C., Stone, N. & Matousek, P. Spatially offset Raman spectroscopy. *Nature Reviews Methods Primers* **1** (2021). https://doi.org/ARTN 21 10.1038/s43586-021-00019-0

34 Wei, D., Chen, S., Ong, Y. H., Perlaki, C. & Liu, Q. Fast wide-field Raman spectroscopic imaging based on simultaneous multi-channel image acquisition and Wiener estimation. *Optics letters* **41**, 2783-2786 (2016). https://doi.org/10.1364/OL.41.002783

35 Papour, A. *et al.* Wide-field Raman imaging for bone detection in tissue. *Biomed Opt Express* **6**, 3892-3897 (2015). https://doi.org/10.1364/BOE.6.003892

36 Yang, S., Li, B., Akkus, A., Akkus, O. & Lang, L. Wide-field Raman imaging of dental lesions. *The Analyst* **139**, 3107-3114 (2014). https://doi.org/10.1039/c4an00164h

37 Wilson, B. C., Jermyn, M. & Leblond, F. Challenges and opportunities in clinical translation of biomedical optical spectroscopy and imaging. *J Biomed Opt* **23**, 1-13 (2018). https://doi.org/10.1117/1.JBO.23.3.030901

38 Stevens, O., Iping Petterson, I. E., Day, J. C. & Stone, N. Developing fibre optic Raman probes for applications in clinical spectroscopy. *Chem Soc Rev* **45**, 1919-1934 (2016). https://doi.org/10.1039/c5cs00850f

39 Arteaga Cardona, F. *et al.* Preventing cation intermixing enables 50% quantum yield in sub-15 nm short-wave infrared-emitting rare-earth based core-shell nanocrystals. *Nat Commun* **14**, 4462 (2023). https://doi.org/10.1038/s41467-023-40031-4

40 del Rosal, B., Thomas, G., Mahadevan-Jansen, A. & Stoddart, P. R. in *Near Infrared-Emitting Nanoparticles for Biomedical Applications* (eds Antonio Benayas, Eva Hemmer, Guosong Hong, & Daniel Jaque) 21-47 (Springer International Publishing, 2020).

41 Woodard, H. Q. & White, D. R. The composition of body tissues. *Br J Radiol* **59**, 1209-1218 (1986). https://doi.org/10.1259/0007-1285-59-708-1209

42 International Commission on Non-Ionizing Radiation, P. ICNIRP Guidelines on Limits of Exposure to Laser Radiation of Wavelengths between 180 nm and 1,000 mum. *Health Phys* **105**, 271-295 (2013). https://doi.org/10.1097/HP.0b013e3182983fd4

43 Wang, B., Chandrasekera, P. C. & Pippin, J. J. Leptin- and leptin receptor-deficient rodent models: relevance for human type 2 diabetes. *Curr Diabetes Rev* **10**, 131-145 (2014). https://doi.org/10.2174/1573399810666140508121012

44 Brunt, E. M. *et al.* Nonalcoholic fatty liver disease. *Nature Reviews Disease Primers* **1**, 15080 (2015). https://doi.org/10.1038/nrdp.2015.80

45 Matsumoto, M. *et al.* An improved mouse model that rapidly develops fibrosis in non-alcoholic steatohepatitis. *Int J Exp Pathol* **94**, 93-103 (2013). https://doi.org/10.1111/iep.12008

46 Wolff, G. *et al.* Hepatocyte-specific activity of TSC22D4 triggers progressive NAFLD by impairing mitochondrial function. *Mol Metab* **60**, 101487 (2022). https://doi.org/10.1016/j.molmet.2022.101487

47 Li, G. *et al.* Intermittent Fasting Promotes White Adipose Browning and Decreases Obesity by Shaping the Gut Microbiota. *Cell Metab* **26**, 672-685 e674 (2017). https://doi.org/10.1016/j.cmet.2017.08.019

48 Tang, H. N. *et al.* Plasticity of adipose tissue in response to fasting and refeeding in male mice. *Nutr Metab (Lond)* **14**, 3 (2017). https://doi.org/10.1186/s12986-016-0159-x

49 Chen, M. *et al.* Long-term monitoring of intravital biological processes using fluorescent protein-assisted NIR-II imaging. *Nat Commun* **13**, 6643 (2022). https://doi.org/10.1038/s41467-022-34274-w

50 Mehlem, A., Hagberg, C. E., Muhl, L., Eriksson, U. & Falkevall, A. Imaging of neutral lipids by oil red O for analyzing the metabolic status in health and disease. *Nat Protoc* **8**, 1149-1154 (2013). https://doi.org/10.1038/nprot.2013.055

51 Saini, R. K., Prasad, P., Shang, X. & Keum, Y. S. Advances in Lipid Extraction Methods-A Review. *Int J Mol Sci* **22** (2021). https://doi.org/10.3390/ijms222413643

52 Libby, P. The changing landscape of atherosclerosis. *Nature* **592**, 524-533 (2021). https://doi.org/10.1038/s41586-021-03392-8

53 Giroud, M., Jodeleit, H., Prentice, K. J. & Bartelt, A. Adipocyte function and the development of cardiometabolic disease. *J Physiol* **600**, 1189-1208 (2022). https://doi.org/10.1113/JP281979

54 Cai, J. M. *et al.* Classification of human carotid atherosclerotic lesions with in vivo multicontrast magnetic resonance imaging. *Circulation* **106**, 1368-1373 (2002). https://doi.org/10.1161/01.cir.0000028591.44554.f9

55 You, A. Y. F. *et al.* Raman spectroscopy imaging reveals interplay between atherosclerosis and medial calcification in the human aorta. *Sci Adv* **3**, e1701156 (2017). https://doi.org/10.1126/sciadv.1701156

56 Marino, M. A., Avendano, D., Zapata, P., Riedl, C. C. & Pinker, K. Lymph Node Imaging in Patients with Primary Breast Cancer: Concurrent Diagnostic Tools. *Oncologist* **25**, e231-e242 (2020). https://doi.org/10.1634/theoncologist.2019-0427

57 Stanford, J. L. *et al.* Urinary and sexual function after radical prostatectomy for clinically localized prostate cancer: the Prostate Cancer Outcomes Study. *JAMA* **283**, 354-360 (2000). https://doi.org/10.1001/jama.283.3.354

58 Sood, A. J., Houlton, J. J., Nguyen, S. A. & Gillespie, M. B. Facial nerve monitoring during parotidectomy: a systematic review and meta-analysis. *Otolaryngology--head and neck surgery : official journal of American Academy of Otolaryngology-Head and Neck Surgery* **152**, 631-637 (2015). https://doi.org/10.1177/0194599814568779

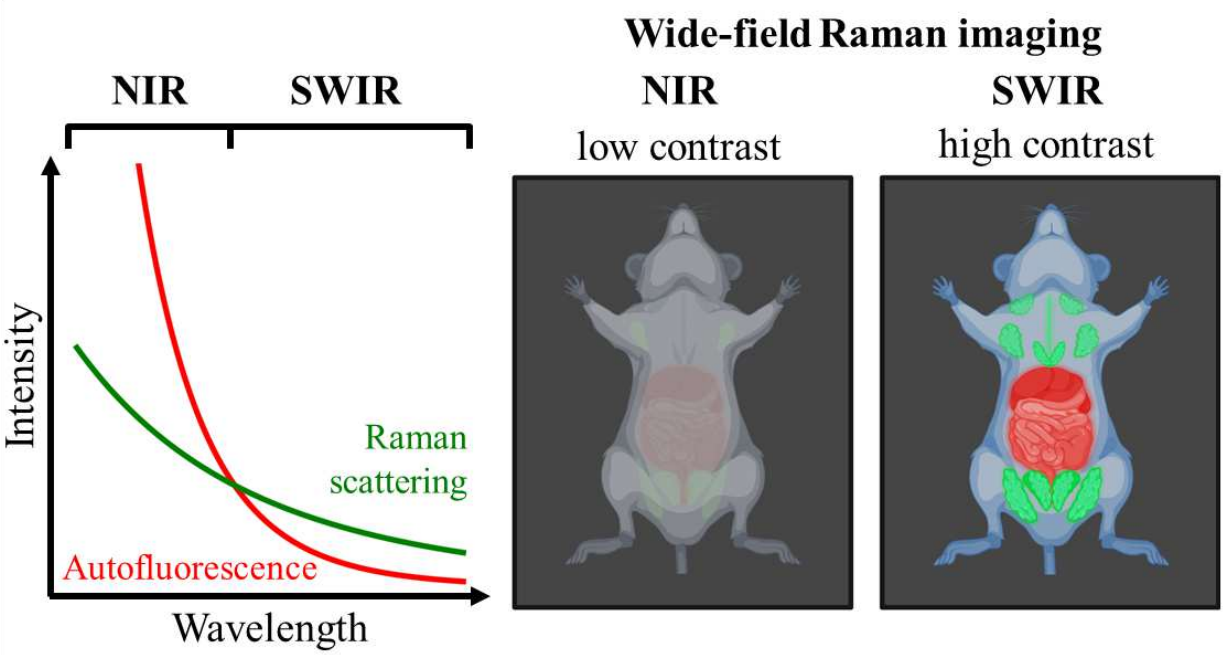
59 Du, H., Dardzinski, B. J., O'Brien, K. J. & Donnelly, L. F. MRI of fat distribution in a mouse model of lysosomal acid lipase deficiency. *AJR Am J Roentgenol* **184**, 658-662 (2005). https://doi.org/10.2214/ajr.184.2.01840658

60 Marzola, P., Boschi, F., Moneta, F., Sbarbati, A. & Zancanaro, C. Preclinical In vivo Imaging for Fat Tissue Identification, Quantification, and Functional Characterization. *Front Pharmacol* **7**, 336 (2016). https://doi.org/10.3389/fphar.2016.00336

61 Weijers, G. *et al.* Noninvasive Staging of Hepatic Steatosis Using Calibrated 2D US with Liver Biopsy as the Reference Standard. *Radiology* **306**, e220104 (2023). https://doi.org/10.1148/radiol.220104

62 Hou, Y. & Tang, J. Advantages of Using 3D Intraoperative Ultrasound and Intraoperative MRI in Glioma Surgery. *Front Oncol* **12**, 925371 (2022). https://doi.org/10.3389/fonc.2022.925371

63 Preziosi, A. *et al.* State of the art medical devices for fluorescence-guided surgery (FGS): technical review and future developments. *Surg Endosc* **38**, 6227-6236 (2024). https://doi.org/10.1007/s00464-024-11236-5



Graphical abstract. Left: Schematic representation of tissue autofluorescence (red) and Raman scattering intensity (green) as a function of illumination wavelength, derived from empirical data (**Supplementary Note 1**). These parameters are tissue-specific and should not be interpreted as a universal model. Right: illustration of the increased Raman imaging contrast achieved by shifting signal detection from the near-infrared (NIR) to the shortwave infrared (SWIR) window in whole-body mice.

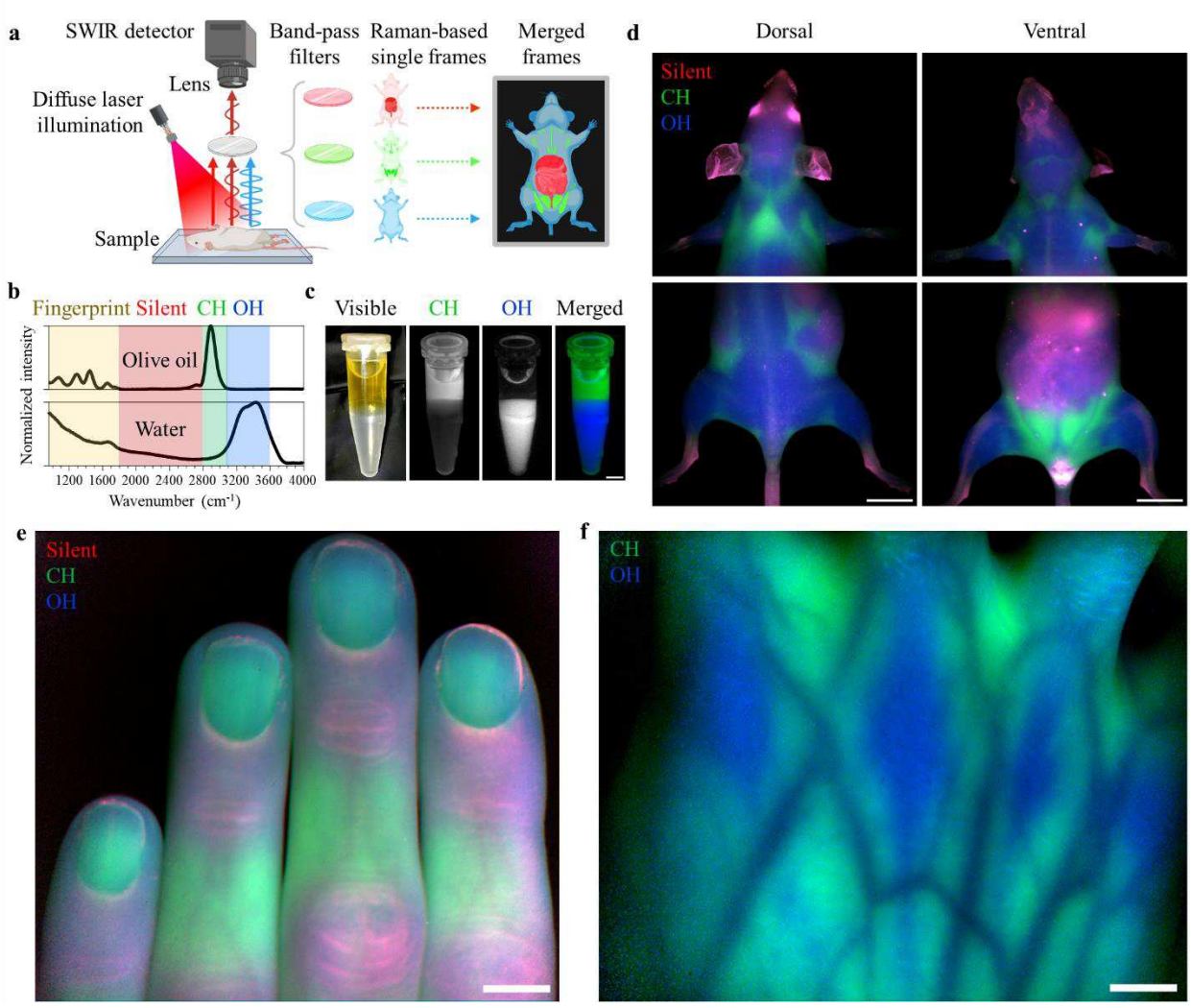


Figure 1. Wide-field macroscopic SWIR Raman imaging system design, *in vitro* validation, and initial biological demonstrations. a) Schematic representation of a SWIR Raman imaging setup. Samples are diffusely illuminated with a laser, and the resulting Raman scattering photons pass through specific band-pass filters and arrive at an InGaAs detector sensitive to shortwave infrared (SWIR) wavelengths. Individual bands are acquired sequentially, have pseudocolors assigned, and are displayed merged. **b)** Raman scattering spectra of pure olive oil and water. The four major Raman scattering regions are labeled. **c-f)** Wide-field SWIR Raman imaging of (c) a two-phase mixture of olive oil and water in a 1.5-mL polypropylene tube, (d) an intact healthy C57BL/6J mouse, (e) the dorsal surface of the left fingers of a human volunteer, and (f) the dorsal surface of the stretched right hand of the same volunteer in panel (e). The Raman-silent, CH and OH regions are shown in red, green or blue, respectively. The displayed contrast was optimized separately for each scattering band; individual scattering bands with corresponding intensity bars are displayed in Fig. S 4 and Fig. S 9. All panels were acquired using System 1 in free-run mode. Imaging parameters: (c) 892 nm illumination (152 mW/cm²), 30 s per-frame exposure; band-pass (BP) filters: BP1200-25 (CH), and BP1300-25 (OH). (d) as (c), 10 s, with the addition of BP1150-25 (silent). (e) 938 nm illumination (115 mW/cm²), 30 s exposure; filters: BP1200-25 (silent), BP1287.5-25 (CH), BP1350-50 (OH). (f) as (e), 10 s exposure. Scale bars: (c) 0.5 cm; (d)-(f) 1 cm.

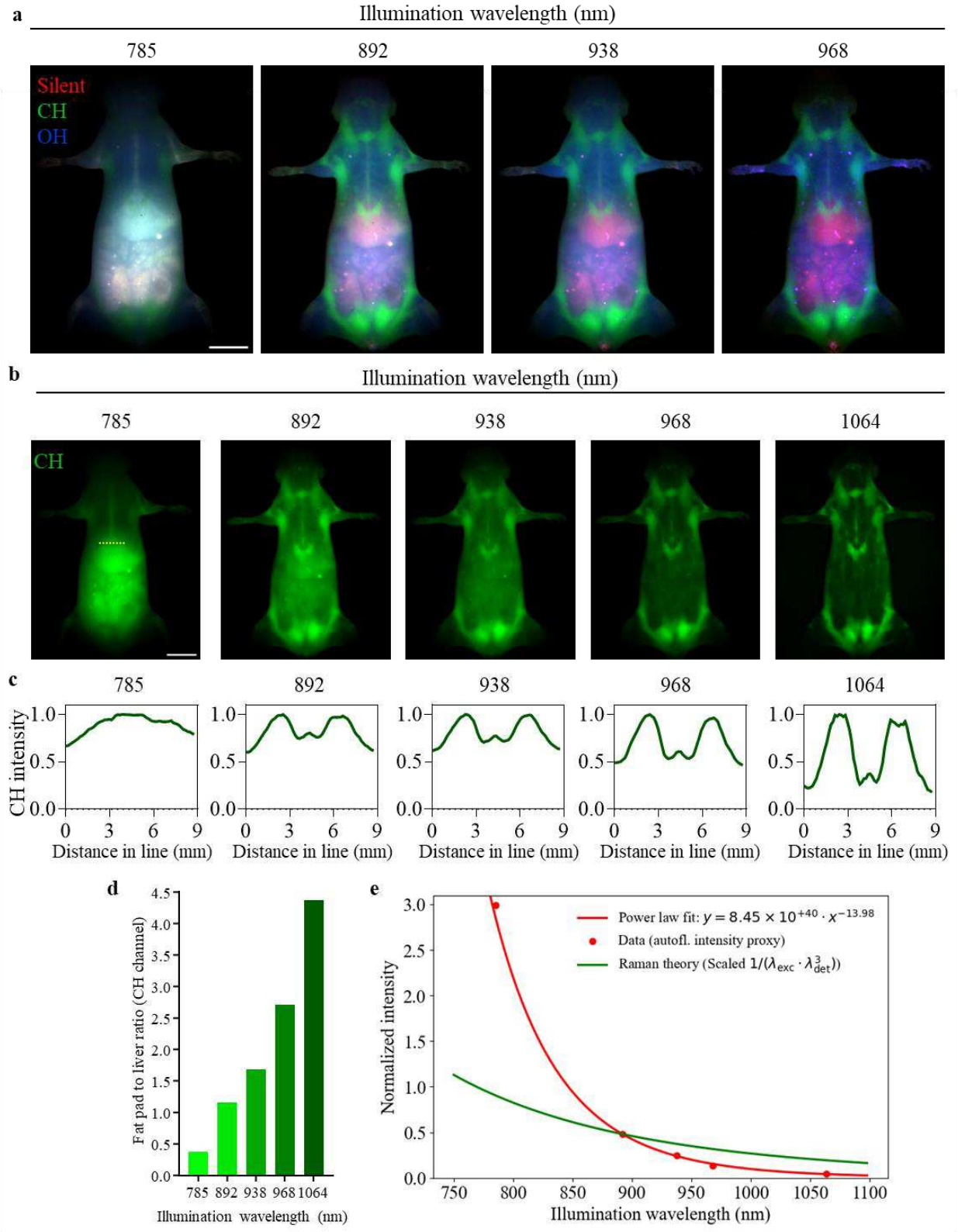


Figure 2. Dominance of Raman scattering as the main source of tissue background in wide-field imaging with illumination wavelengths equal or above 892 nm. a) Wide-field SWIR Raman imaging of an intact healthy C57BL/6J mouse at illumination wavelengths of 785, 892, 938 or 968 nm. The Raman-silent, CH and OH regions are displayed in red, green or blue,

respectively. **b)** Individual CH region frames for the merged images in panel (a), with the addition of 1064 nm illumination. **c)** Pixel intensity profile along a line crossing the xiphoid cartilage on the mouse chest, extracted from the CH region images in panel (b). **d)** Ratio of mean CH intensity between fat pad and liver, measured for each illumination wavelength, serving as a chemical contrast metric. **e)** Empirically derived autofluorescence (red) and Raman scattering (green) intensity trends as a function of excitation wavelength, extracted from the dataset in panel (b); see Supplementary Note 1 for a full description of the derivation**.** The displayed contrast was optimized separately for each scattering band. Individual images with corresponding intensity bars are displayed in Fig. S 14, while the regions of interest (ROIs) drawn to extract the line profile in panel (c) and the fat pad to liver ratio in panel (d) are displayed in Fig. S 15. All panels were acquired using System 1 in free-run mode. Imaging parameters: 785 nm illumination (138 mW/cm²), 10 s per-frame exposure; band-pass (BP) filters: BP962.5-25 (silent), BP1012.5-25 (CH), and BP1062.5-25 (OH); 892 nm illumination (145 mW/cm²), 30 s exposure; filters: BP1150-25 (silent), BP1200-25 (CH), BP1300-25 (OH); 938 nm illumination (153 mW/cm²), 30 s exposure; filters: BP1175-50 (silent), BP1300-50 (CH), BP1350-50 (OH); 968 nm illumination (152 mW/cm²), 45 s exposure; filters: BP1212.5-25 (silent), BP1350-50 (CH), BP1450-50 (OH); 1064 nm illumination (178 mW/cm²), 60 s exposure; filters: BP1400-50 (silent), BP1550-50 (CH), BP1600-50 (OH). Data are representative of two mice. Scale bars: 1 cm.

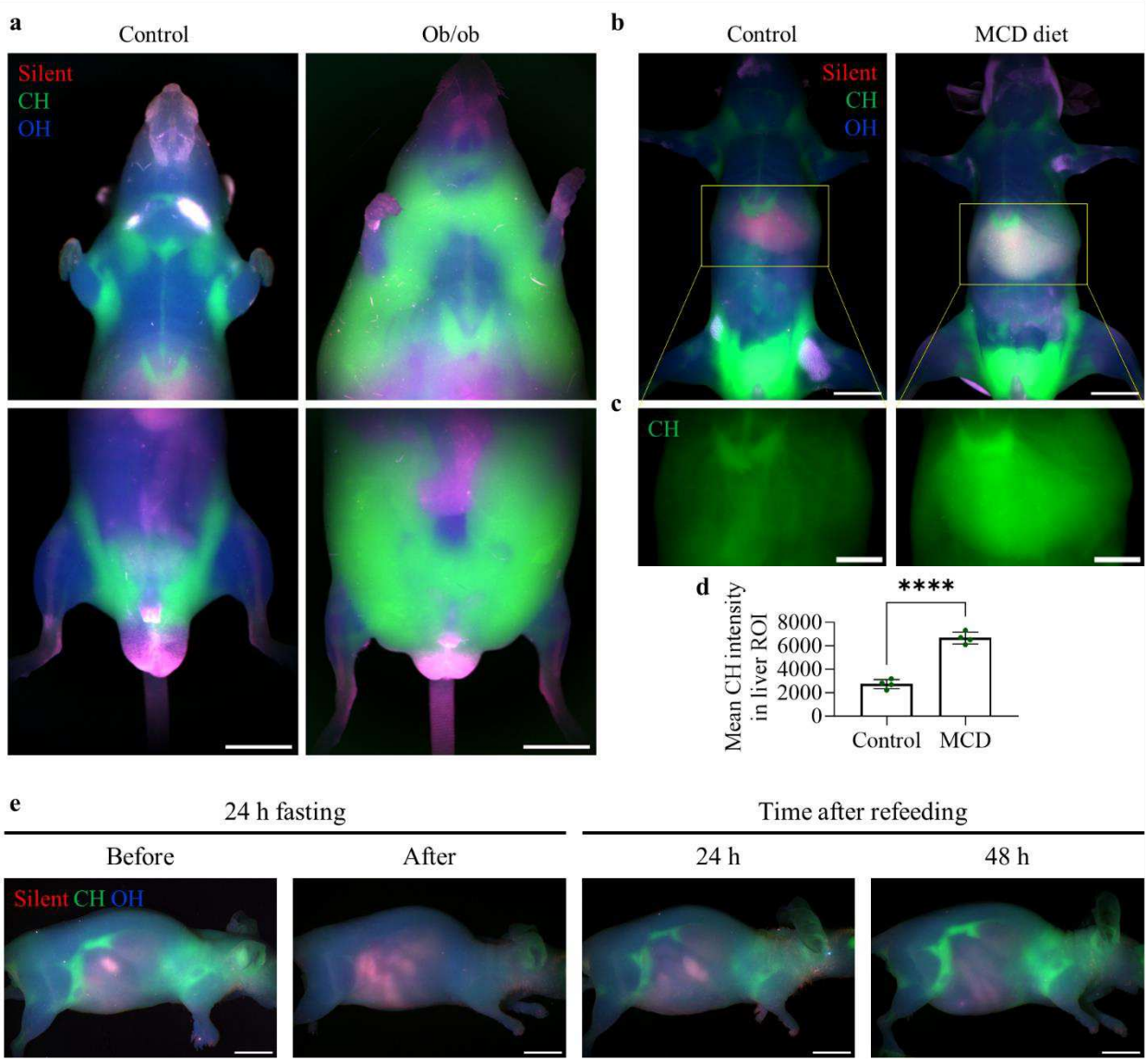


Figure 3. Non-invasive *in vivo* SWIR Raman imaging of chemical contrast in mouse pathophysiology. a) SWIR Raman imaging of a genetically obese mouse (ob/ob) and an age-matched lean C57BL/6J control mouse, representative of 2 mice per genotype. **b-c)** SWIR Raman imaging of a C57BL/6N mouse after 6 weeks on a diet deficient in methionine and choline (MCD) or a normal diet (control), representative of 4 mice per group. (b) Whole-body view. (c) Cropped view of the liver region displaying only the CH region. Note that the mice in panels (a)-(c) are from pigmented strains, and pigment-derived autofluorescence can introduce measurement artifacts (see Supplementary Note 4). **d)** Quantification of mean CH Raman intensity values (counts/min) in a liver region of interest (ROI) extracted from the MCD and control mice. Differences between the groups were statistically analyzed using an unpaired, two-tailed t test. **** indicates P-value < 0.0001. **e)** *In vivo* imaging of body composition changes in anesthetized nude mice after fasting and refeeding. Animals were imaged at baseline (before), after 24 h of fasting, then after 24 and 48 h of refeeding. Results are representative of two animals. The Raman-silent, CH and OH regions are displayed in red, green or blue, respectively. The displayed contrast was optimized for each scattering band, and, except for panel (a), the same intensity values are

displayed for each image within a panel to enable direct comparison. Individual images with corresponding intensity bars are displayed in Fig. S 19, Fig. S 20, and Fig. S 23, while Fig. S 21 displays the biological replicates of panels (b)-(d), and Fig. S 22 shows the ROIs drawn to extract the mean values in panel (d). All panels were acquired using System 1 in free-run mode. Imaging parameters: (a) 892 nm illumination (152 mW/cm²), 30 s per-frame exposure; band-pass (BP) filters: BP1150-25 (silent), BP1200-25 (CH), and BP1300-25 (OH). (b-c) 938 nm illumination (159 mW/cm²), 45 s exposure; filters: BP1200-25 (silent), BP1287.5-25 (CH), BP1350-25 (OH). (e) 938 nm illumination (143 mW/cm²), 30 s exposure; filters: BP1143.75-12.5 (silent), BP1287.5-25 (CH), BP1362.5-25 (OH). Scale bars: (a)-(b) 1 cm; (c) 0.5 cm; (e) 1 cm.

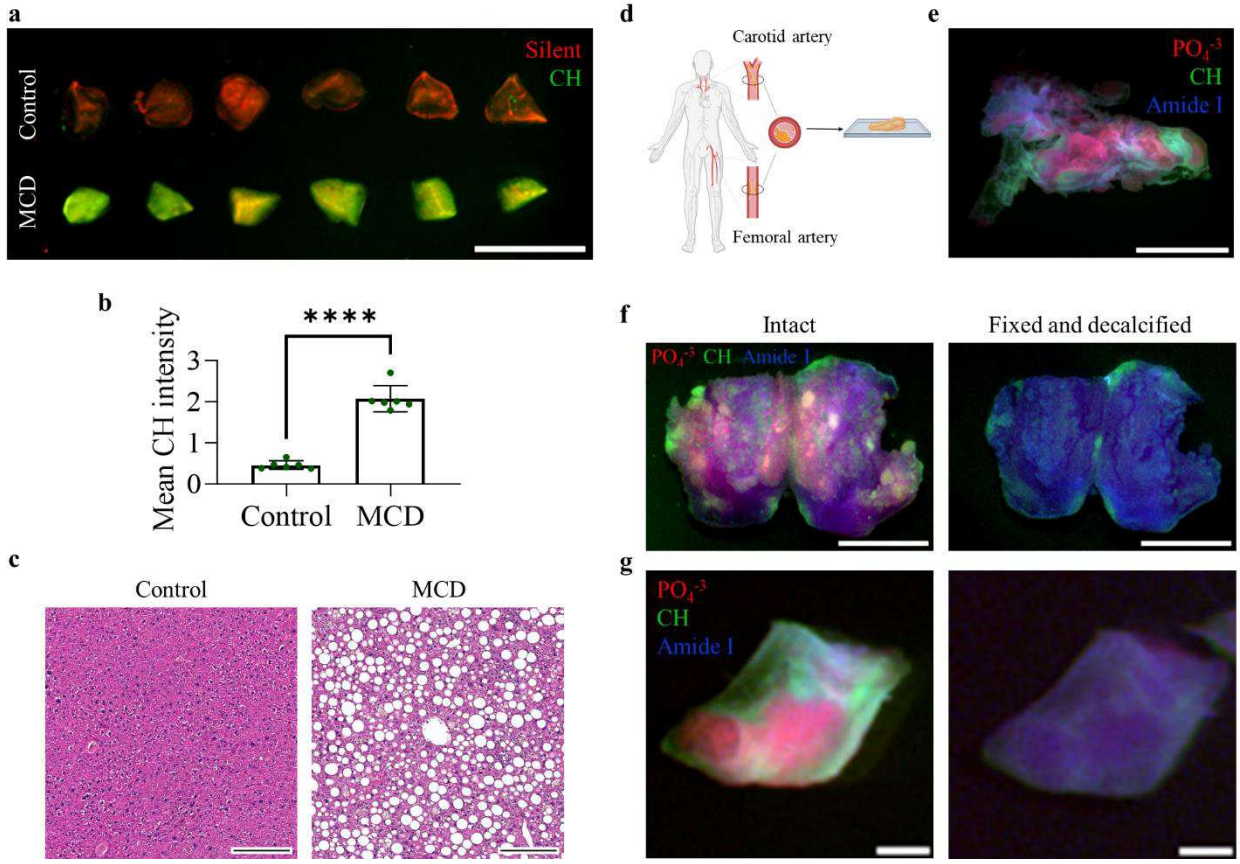


Figure 4. SWIR Raman imaging for *ex vivo* analysis of tissue composition in unfixed samples from mice and humans. a-c) Analysis of livers excised from C57BL/6N mice after 7 weeks on a diet deficient in methionine and choline (MCD) or on a normal diet (control). Liver samples (n = 6 per group) were analyzed in terms of (a) SWIR Raman imaging with illumination at 1064 nm, and (b) quantitation of mean CH Raman intensity [counts/min/(mW/cm^2)] based on the image in panel (a). Differences between the groups were statistically analyzed using an unpaired, two-tailed t test. **** indicates P-value < 0.0001. The Raman-silent and CH regions are displayed in red and green, respectively. (c) Representative histological analysis of the liver samples in panel (a) with hematoxylin and eosin staining. **d-g)** SWIR Raman tissue analysis of human atherosclerotic plaques from carotid and femoral artery surgeries. (d) Schematic representation of the surgical biopsy. The plaque is removed from the artery, and the intact specimen is subjected to imaging. (e) Atherosclerotic plaque excised from a human femoral artery, imaged in the SWIR Raman imaging regions corresponding to calcification-associated PO_4^{-3} (red), protein-associated amide I (blue) and lipid-associated CH (green). (f)-(g) Comparison between Raman images of intact atherosclerotic plaque specimens (left) and after a fixation and decalcification protocol (right) of a clinical specimen from a (f) femoral artery and (g) a carotid artery. The displayed contrast was optimized for each scattering band; in panels (f)-(g), both frames within each panel display the same intensity values to enable direct comparison. Individual images with corresponding intensity bars are displayed in Fig. S 31, Fig. S 33 and Fig. S 34. All panels were acquired using System 1 in free-run mode. Imaging parameters: (a) 1064 nm illumination (115 mW/cm²), 600 s per-frame exposure; band-pass (BP) filters: BP1337.5-25 (silent) and BP1550-50 (CH). (e) 1064 nm

illumination (177 mW/cm²), 300 s exposure; filters: BP1187.5-25 (PO_4^{-3}), BP1287.5-25 (Amide I), and BP1550-50 (CH). **(f-g)** 1064 nm illumination (163 mW/cm²), 300 s exposure; same filtering parameters as (e). Scale bars: (a) 1 cm; (c) 200 µm; (e)-(f) 1 cm; (g) 0.2 cm.

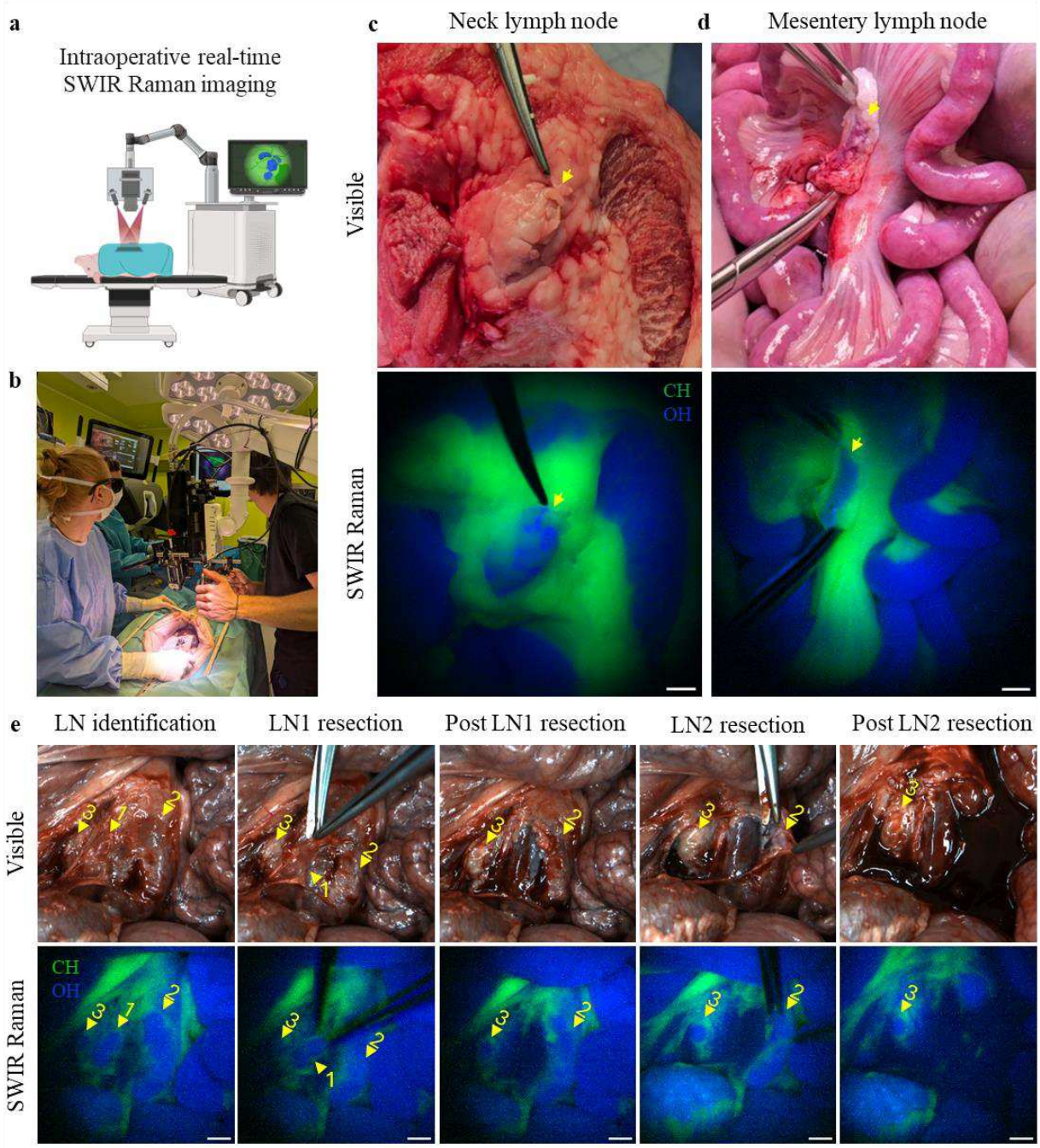


Figure 5. Real-time intraoperative SWIR Raman imaging for surgical guidance. a-b) Intraoperative imaging platform. The imaging system is mounted on a medical arm and positioned over the open surgical field. (a) Schematic. (b) Photograph of the system deployed in an operating room during intraoperative imaging of a living pig. Live multicolor SWIR Raman and white-light video streams are displayed on bedside monitors, enabling continuous visualization of tissue contrast during surgery. **c-d)** SWIR Raman imaging of post-mortem porcine lymph nodes across two anatomical regions: (c) neck and (d) mesentery. Yellow arrowheads indicate the lymph node in each panel. **e)** Intraoperative identification and resection of mesenteric lymph nodes in a living pig, with images are shown at five stages of the procedure. Three lymph nodes (LN1-LN3) are initially identified within the surgical field. Subsequent images capture resection of LN1, the

resulting resection cavity, resection of LN2, and the surgical field after LN2 removal. Individual images with corresponding intensity bars are displayed in Fig. S 40 and Fig. S 41. Panels (c) - (e) display the visible-light image (top) and the merged SWIR Raman image with CH-band in green and OH-band in blue (bottom). All panels were acquired using System 2 in triggered mode (10% duty cycle, 0.1 s exposure per channel); single band-pass filter: BP1275-50. Illumination parameters: (c) OH: 892 nm, 600 mW/cm² peak (60 mW/cm² time-averaged); CH: 936 nm, 600 mW/cm² peak (60 mW/cm² time-averaged). (d)-(e) OH: 892 nm, 700 mW/cm² peak (70 mW/cm² time-averaged); CH: 936 nm, 465 mW/cm² peak (46.5 mW/cm² time-averaged). Scale bars: 1 cm.

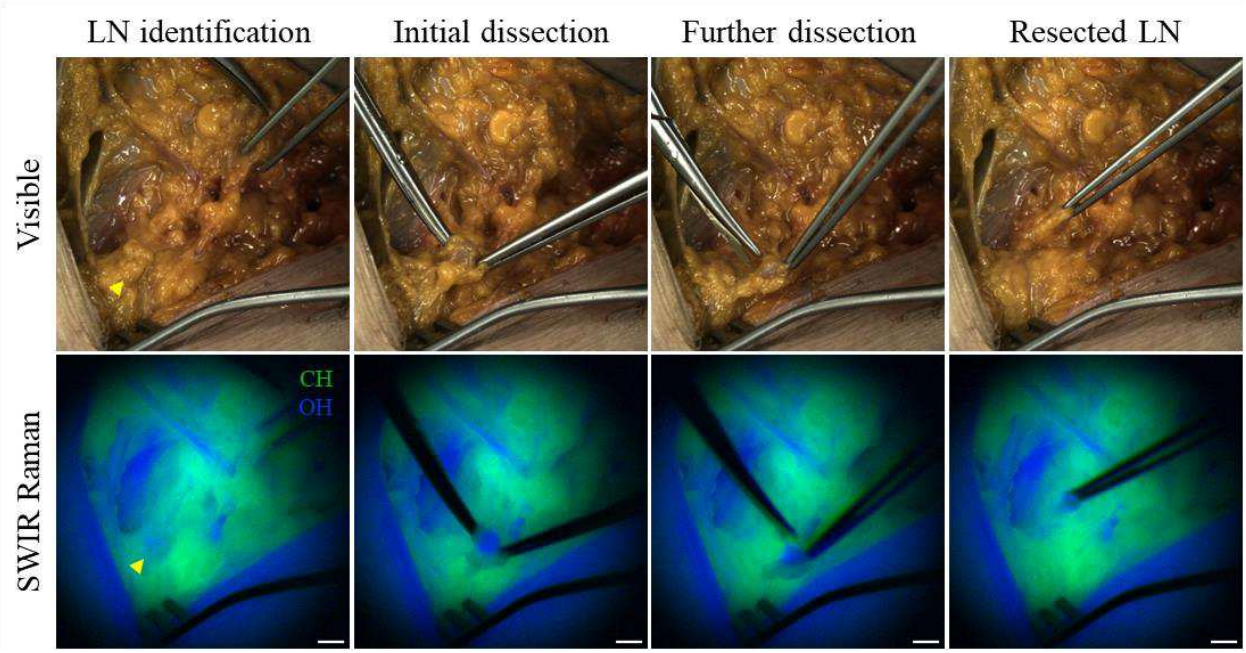


Figure 6. Real-time SWIR Raman-guided lymph node identification and resection in a human body donor. White-light images (top) and merged CH-band (green) and OH-band (blue) Raman images (bottom) acquired during identification, dissection, manipulation, and resection of an inguinal lymph node (LN). The lymph node (yellow arrowhead) remains readily distinguishable from surrounding adipose tissue throughout the procedure, demonstrating that the chemical contrast observed in porcine studies translates to human anatomy under operating room conditions. Individual images with corresponding intensity bars are displayed in Fig. S 42. Images were acquired using System 2 in triggered mode (15% duty cycle, 0.15 s exposure per channel); single band-pass filter: BP1275-50. Imaging parameters: OH: 892 nm, 524 mW/cm² peak (78.6 mW/cm² time-averaged); CH: 936 nm, 384 mW/cm² peak (57.6 mW/cm² time-averaged). Scale bars: 1 cm.

Methods

Ethics statement

All animal experiments were performed in conformity with institutional and national regulations following approval by the government of Upper Bavaria and Saxony. Studies involving human tissue were conducted in accordance with relevant institutional and national regulations and the principles of the Declaration of Helsinki, with institutional ethics approval from the Technische Universität Dresden and Ludwig-Maximilians-Universität München, and informed consent, where applicable.

Materials

Chemicals and laboratory consumables were purchased from either Sigma-Aldrich (Taufkirchen, Germany), Merck (Darmstadt, Germany), Carl Roth (Karlsruhe, Germany), Thermo Fisher Scientific (Roskilde, Denmark). Optical and optomechanical components were purchased from Edmund Optics (York, United Kingdom), Thorlabs (Bergkirchen, Germany), Qioptic (Göttingen, Germany), Lumics (Berlin, Germany), Schneider-Kreuznach (Bad Kreuznach, Germany), NKT Photonics (Birkerød, Denmark), First Light Imaging (Meyreuil, France), or Teledyne Princeton Instruments (Trenton, NJ, USA). Mouse chow was purchased from Research Diets (New Brunswick, NJ, USA) or Altromin (Lage, Germany).

Systems for wide-field macroscopic imaging based on SWIR Raman scattering

Two imaging systems were developed for this work, sharing the same optical design principle but optimized for different operating conditions: a stationary system for high-signal-to-noise-ratio (SNR) imaging and long exposures, and a portable system for real-time intraoperative use. Both systems follow a design similar to that of systems developed for SWIR fluorescence detection, which we adapted for Raman scattering imaging by selecting illumination and detection wavelengths corresponding to specific Raman bands, and by using low-noise, InGaAs-based cameras capable of detecting faint SWIR signals.

The lasers used in this work have a typical spectral width of 5-10 nm, which does not affect chemical specificity since the targeted CH, OH, and silent Raman regions are broad relative to this width. Our main engineering challenge was stray light suppression, arising from the angle-dependent transmission of the detection filters: small deviations from normal incidence shift the filter passband toward shorter wavelengths, allowing out-of-band laser light to reach the detector. This was mitigated by placing an absorbing filter between the band-pass filters, and by empirically optimizing the inter-filter spacing until stray light was minimized and the Raman signal could be detected. The minimum OD required from the filter stack was estimated as $\log_{10}(\frac{N_{Laser}}{N_{Raman}})$, where $N_{Laser}$is the number of incident laser photons per pixel during a single exposure and N_{Raman} is the number of Raman photons detected at the sensor from the same pixel area. This ratio defines how many orders of magnitude the filter stack must suppress the laser so that leaked laser light remains below the detected Raman signal. Using gWAT ROI (**Fig. S 49**) photon budget from **Supplementary Note 5** as the signal reference, we estimated a required minimum of OD 16-18.

The same angle-dependent passband shift that necessitates this degree of stray light suppression also limits spectral resolution, as the effective transmission window of each filter broadens with the angle distribution. For the broad Raman bands targeted here this is negligible, but fingerprint-

region applications requiring resolution of closely spaced vibrational features would need to account for these tolerances or adopt designs enforcing stricter collimation.

SWIR Raman System 1: stationary system for high-SNR imaging

Samples were illuminated using the following lasers (Lumics) to obtain the wavelengths indicated in the figure legends: 672 nm, LU0680D010-E10FH; 785 nm, LU0785D250-U70AN; 892 nm, LU0890D400-U10AF; 938 nm, LU0940D250-U70AF; 968 nm, LU0980D350-U30AF; and 1064 nm, LU1064D350-U70AF. Lasers were connected to a 7 x 1 fan-out fiber-optic bundle (catalog no. BF76LS01, Thorlabs) with a core diameter of 600 μm. The laser light traveled from the common end of the multi-fiber bundle into an excitation cube (catalog no. KCB1EC/M, Thorlabs), was reflected off a mirror (catalog no. BBE1-E03, Thorlabs), and passed through a positive achromat (catalog no. AC254-050-B, Thorlabs). The wavelength of the laser output was cleaned up using appropriate short-pass filters to prevent detection of the laser light, for example a 900-nm short-pass filter for illumination at 892 nm. From the achromat, the laser light passed through an engineered diffuser (catalog no. ED1-S20-MD, Thorlabs) to provide uniform illumination across the field of view.

Depending on the experiment, the maximum laser power density varied roughly between 50 and 150 mW/cm^2, as measured using a PM100D power meter equipped with a S130C sensor (Thorlabs). These irradiances densities remained within international exposure limits [42].

A nitrogen-cooled camera (NIRvana LN, Princeton Instruments) was mounted on a rail carriage (catalog no. G026428000, Qioptic) parallel to an optical table (catalog nos. SDR7590 and B7590L, Thorlabs). This camera was chosen because of its deep cooling (-190 ^{o}C), low dark current, and low read noise, which provide high signal-to-noise ratios at long exposures in a single frame. An f/2.8, 50-mm lens capable of transmitting SWIR radiation (SWIRON 2.8/50, Schneider-Kreuznach) was attached to the camera using an F-mount adapter. Three 30-mm cage plates with removable holders (catalog no. CFH2/M, Thorlabs) for 1-inch optical filters (filter slots 1-3) were positioned in front of the camera lens to facilitate filter changes. A silver mirror in a right-angle kinematic elliptical holder (catalog nos. KCB1EC/M and PFE10-P01, Thorlabs) was mounted on the cage plate farthest from the lens in order to direct the laser light towards the optical table. A 60-mm cage plate with a removable holder for 2-inch optical filters (catalog no. LCFH2/M, Thorlabs) was attached to the side of the kinematic elliptical holder closer to the sample. Of the four filter positions, the one closest to the camera lens and the one closest to the sample (slots 1 and 4, respectively) were usually occupied by long-pass filters, which eliminated stray light from the laser; for example, the filters were 1000-nm long-pass filters when samples were illuminated at 968 nm. The two central filter positions were typically occupied by band-pass filters to define the detection band. This configuration yielded fields of view of approximately 56 cm^2, however a different choice of optics could enable larger or smaller fields of view, reflecting the scale-spanning character of wide-field imaging. All optical components were covered with black aluminum foil (catalog no. BKF12, Thorlabs), and the system was enclosed within black nylon (catalog no. BK5, Thorlabs). All imaging with this system was performed in a dark room, with typical per-channel exposure times of 10-60 s, occasionally extending to 300 s depending on the sample and illumination wavelength.

SWIR Raman System 2: portable system for real-time intraoperative imaging

A second wide-field SWIR Raman imaging system was developed to enable portable operation, larger fields of view, increased light throughput, and real-time imaging under operating-room

conditions. Illumination followed the same general optical design as System 1, but employed two independent illumination units positioned symmetrically around the imaging field. Each illumination unit consisted of a fiber-coupled laser source, spectral cleanup filters, an achromatic lens, and an engineered diffuser. Unlike System 1, the excitation cube and mirror assembly were omitted. This configuration provided more homogeneous illumination over a larger field of view and enabled operation of two laser diodes of the same wavelength in parallel to increase irradiance when required.

Detection was performed using a water-cooled InGaAs camera (C-RED 2 SWIR, First Light Imaging) operated at −40 °C. The camera was used with a 35-mm f/1.4 camera lens (catalog no. SWIR35, Navitar), providing 4-fold greater light collection efficiency than the f/2.8 lens used in System 1. Depending on the working distance and optical configuration, fields of view of up to approximately 100 cm² were obtained, offering a further ~3-fold increase in photon throughput per pixel at the cost of spatial sampling resolution.

As in System 1, four filter positions were located in front of the camera lens. Unlike System 1, all positions accepted 1-inch filters. Dielectric long-pass filters were typically placed in the first and fourth positions for laser rejection, with one band-pass filter in the third position to define the detection window. In several configurations, an absorptive long-pass filter (e.g. SCHOTT RG1000 filter, catalog no. 32-760, Edmund Optics) was placed in the second position between reflective interference filters to improve suppression of scattered excitation light.

A white-light video stream was acquired in parallel using a visible camera (Alvium 1800-U240c, Allied Vision) equipped with a 750-nm short-pass filter (catalog no. FESH0750, Thorlabs) to suppress residual laser light. The system was mounted on a medical monitor arm (catalog no. FPMA-HAW100HC, Neomounts), which could be operated either in a fixed configuration for benchtop imaging experiments or in a freely articulated configuration for intraoperative imaging.

Free-run data acquisition mode

Both Systems 1 and 2 could be operated in a continuous free-run acquisition mode for experiments not requiring synchronized multi-channel acquisition. This mode was used for all experiments acquired with System 1 and for selected experiments acquired with System 2, including the *in* vivo mouse measurements used for spectral comparison.

Data acquisition for System 1 was performed using Lightfield 6.15.1.2112 (Teledyne Princeton Instruments). Raman scattering in different bands was imaged sequentially with manual filter changes. Specific laser and filter specifications for each imaging experiment can be found in the figure captions. An illustrative data acquisition workflow for SWIR Raman imaging using 892-nm illumination consisted of the following: the laser was turned on, a first frame was acquired using the band-pass filter combination 1150-25 (center wavelength - width) to detect the Raman-silent region (**Figure 1 a**), the laser was turned off and the filter was changed. The laser was then turned back on and a second frame was acquired with the filter combination 1200-25 to detect the CH region. This process was repeated to acquire a third frame with the filter combination 1300-25 to detect the OH band. For data processing, dark frames were captured for each exposure time and flatfield images were captured for each laser configuration.

Data were processed using Python 3 and Fiji (ImageJ 1.54f, US National Institutes of Health, Bethesda, MD, USA). First, dark and flatfield frames were generated by averaging 5-10 frames.

Then, all image acquisitions had their corresponding dark frames subtracted, after which they were further corrected for exposure time and divided by the power density map, which was obtained by multiplying together the flatfield frame and the maximum power density in the field of view. These processing steps yielded data in the form of counts/min/(mW/cm^2). Given the three-dimensional nature of *in vivo* imaging, flatfield correction was not applied to *in vivo* datasets; these images are therefore represented in counts/min. Image quantification was performed using manually defined regions of interest, from which mean intensities or integrated signals were extracted.

Triggered real-time acquisition mode

For intraoperative imaging experiments and other experiments requiring real-time display, the portable System 2 was operated in a synchronized dual-wavelength acquisition mode.

Illumination was provided by the same laser diode models used in System 1, centered at 892 nm (LU0890D400-U10AF, Lumics) and 936 nm (LU0940D250-U70AF, Lumics). For each excitation wavelength, two laser diodes were typically operated in parallel and individually temperature-tuned to achieve the desired output wavelengths. This configuration increased irradiance at the sample surface by approximately 4- to 6-fold relative to System 1 while simultaneously increasing the illuminated area. The increased irradiance enabled exposure times as short as 100 ms while maintaining sufficient Raman signal for anatomical visualization. A laser-off delay was introduced to compensate for the increase in instantaneous irradiance, maintaining the average irradiance within laser safety limits (details in the next section).

The excitation wavelengths were selected such that the OH-band Raman signal under 892 nm illumination and the CH-band Raman signal under 936 nm illumination were both shifted into the transmission window of a single 1275-50 band-pass filter. For this acquisition mode, filter slot 1 contained an 1100-nm long-pass filter (catalog no. FELH1100, Thorlabs), slot 2 contained a 1000-nm absorbing long-pass filter (catalog no. 32-760, Edmund Optics), slot 3 contained the 1275-50 band-pass filter (catalog no. 87-865, Edmund Optics), and slot 4 contained a second 1100-nm long-pass filter. Excitation wavelengths were spectrally cleaned using 950-nm short-pass filters (catalog no. FESH0950, Thorlabs).

Because exposure times were fixed across experiments performed in triggered acquisition mode, image intensities acquired with this mode are reported as detector counts unless otherwise specified.

Acquisition control, synchronization, and real-time display (triggered mode)

Image acquisition and system control were implemented through a custom software interface written in Python. The software communicated with the camera through the manufacturer's application programming interface and controlled laser triggering through an Arduino UNO microcontroller connected via a serial interface.

The Arduino generated synchronized trigger signals for both the camera and laser sources. The trigger pulse width determined both the camera exposure time and the illumination duration of the corresponding laser. A resistor was inserted to lower the default 5V output of the Arduino down to ~3V to match the trigger input requirements of the C-RED 2 camera.

A typical acquisition cycle consisted of four sequential 100-ms exposures: $\mathrm{background}_1$, $\mathrm{raw}_{\mathrm{OH}}$, $\mathrm{raw}_{\mathrm{CH}}$, $\mathrm{background}_2$, separated by short readout intervals between frames. Following acquisition of the four frames, an additional delay was applied to maintain a total cycle duration of 1 s (**Fig. S 37 b**). Background frames were captured with the lasers off to correct for detector dark current and occasional ambient-light leakage. Raw frames were acquired under targeted illumination at 892 and 936 nm to capture the OH and CH Raman bands, respectively. Background correction was performed by subtracting the temporally nearest laser-off frame from each Raman image; for specific experiments, only one background frame was acquired per cycle. The resulting 1-s acquisition cycle produced a dual-channel Raman image per second. The laser-off intervals regulated the average laser irradiance to remain within laser safety limits while still permitting high instantaneous irradiance during active Raman frame integration.

Background subtraction, channel assignment, image merging, and display were performed automatically by the acquisition software immediately after completion of each acquisition cycle. Corrected CH- and OH-band images were rendered as green and blue channels, respectively, combined into a pseudocolor image, and displayed to the operator in real time. For intraoperative applications, this SWIR Raman stream was displayed continuously on operating-room monitors alongside the visible-light camera feed, providing direct real-time guidance for the surgeon.

SWIR Raman imaging of isolated compounds

Olive oil (catalog no. 8873.1, Carl Roth) and water (0.75 mL of each) were transferred into a 1.5-mL microcentrifuge tube, and imaged in the wide-field SWIR Raman imaging setup upon 892 nm illumination. Powders from the isolated compounds, palmitic acid (catalog no. P0500, Sigma-Aldrich), cholesterol (catalog no. C8667, Sigma-Aldrich), hydroxyapatite (catalog no. 289396, Sigma-Aldrich), collagen from calf skin (catalog no. C9791, Sigma-Aldrich), and elastin from bovine neck ligament (catalog no. E1625, Sigma-Aldrich) were placed in a black polystyrene 96-well plate (catalog no. 237108, Thermo Fisher Scientific), and imaged in the same setup at 1064 nm illumination.

Raman spectroscopy of isolated compounds

The isolated compounds were added to a black quartz cuvette (catalog no. Z801607, Merck), and spectra were acquired using the liquid nitrogen-cooled InGaAs line detector Pylon-IR 1024-1.7 (Teledyne Princeton Instruments) connected to a Czerny-Turner spectrograph (catalog no. HRS-300, Teledyne Princeton Instruments). A super-continuum white light laser (SuperK-Extreme, NKT Photonics) filtered with a tunable filter (SR-Extended-8HP LLTF Contrast, NKT Photonics) was used as excitation source. Spectra were acquired with illumination at 892 or 1064 nm, then cleaned up with, respectively, a 900-nm short-pass filter (catalog no. FESH0900, Thorlabs) or the combination of a band-pass filter 1064-10 nm (catalog no. FLH1064-10, Thorlabs) and 1100-nm short-pass filter (catalog no. 64-339, Edmund Optics). The photoemission was collected using a pair of silver-coated off-axis parabolic mirrors (catalog nos. MPD269-P01 and MPD269-P01-H, Thorlabs), which focus the light onto a 400-µm multimode fiber (catalog no. M28L01, Thorlabs) connected to the spectrograph. Either a 950-nm or two 1100-nm long-pass filters (catalog nos. FELH0950 and FELH1100, Thorlabs) were positioned in front of the fiber to further block the excitation light. Intensity correction takes were acquired with a calibration lamp (catalog no. SLS201L/M, Thorlabs). Background takes were also acquired. Background and intensity corrections were performed using Python3.

Sensitivity characterization

The instrumental sensitivity of the imaging setup was assessed by a limit-of-detection (LOD) analysis using serial dilutions of a lipid emulsion (Intralipid 20%, catalog no. I141, Sigma-Aldrich) in distilled water. Dilutions were prepared gravimetrically using a high-precision balance (Sartorius Cubis II) from an intermediate 2.0% stock, targeting nominal concentrations between 0.01% and 2.0% (v/v). Three independent replicates (n = 3) were prepared for each concentration and loaded into glass Petri dishes (catalog no. 5058541, Normax; 60 mm diameter, 15 mL per dish). Evaporation during imaging was assessed gravimetrically and confirmed to be negligible (<0.35% mass loss). Samples were imaged in the SWIR Raman imaging under 892 nm illumination (~450 mW/cm², 10 s exposure) with a CH-band bandpass filter (BP 1200-25). Signal was quantified from circular regions of interest drawn within each dish; a background region of equivalent size accounted for detector noise and residual laser bleed-through. At concentrations above ~0.1% (v/v), multiple scattering attenuates the incident irradiance through the sample depth, introducing nonlinearity in the concentration-signal relationship. The LOD was therefore calculated from the linear low-concentration regime (0.01-0.1%), where attenuation is negligible and the full sample depth is interrogated. A linear calibration curve was fitted to this range, and the LOD was calculated as $3.3 \times \sigma_blank / slope$, where σ_blank denotes the standard deviation of the background region.

Mouse experiments

Experiments were carried out using four mouse strains: C57BL/6J, C57BL/6N, athymic nude, and Ob/Ob (all purchased from Charles River Laboratories, Germany). Animals were housed at a temperature of 23 °C and relative humidity of 45-65% on a 12/12 h light/dark cycle. Animals were imaged either after anesthesia with isoflurane at 4% in oxygen for induction and 1.5-2% for maintenance, or after euthanasia. During imaging of live animals, the mouse temperature was maintained between 35 and 37 ºC. Organ dissections were performed after animal euthanasia. For the awake mouse demonstration, a nude mouse that had undergone an anesthetized imaging session was allowed to recover and subsequently imaged after waking.

In vivo Raman spectroscopy

In vivo spectra were acquired from anesthetized athymic mice (24-week-old females, n=2) using the same spectrograph, light source, and InGaAs detector described above. Illumination wavelengths of 785, 892, and 938 nm were used. For 785 nm illumination, an 800-nm short-pass filter (catalog no. FESH0800, Thorlabs) was used for excitation clean-up, and a 900-nm long-pass filter (catalog no. FELH0900, Thorlabs) was used as an emission filter. For 892 and 938 nm illumination, a 950-nm short-pass filter and a 1000-nm long-pass emission filter were used (catalog nos. FESH0950 and FELH1000, Thorlabs).

Spectra were collected from two anatomical regions per animal: skin overlying inguinal white adipose tissue (iWAT, Region A) and skin overlying hindlimb skeletal muscle (Region B), identified based on anatomical landmarks. Background and intensity corrections were applied as described above. Autofluorescence background was estimated by fitting a single exponential function to spectral regions outside the Raman bands (785 nm: 910-980 nm and 1125-1200 nm; 892 nm: 1050-1170 nm and 1350-1475 nm; 938 nm: 1050-1225 nm and 1440-1475 nm). The fitted background was subsequently subtracted from the measured spectrum to isolate the residual Raman signal. All spectral processing and analysis were performed in Python 3.

Ex vivo skin Raman spectroscopy

Skin patches from pigmented and unpigmented regions were dissected from an 8-week-old C57BL/6J female mouse. Spectra were acquired under 938 nm illumination using the same spectrograph, light source, and InGaAs detector described above. Excitation clean-up and emission filtering followed the same configuration as for 938 nm *in vivo* measurements (950-nm short-pass and 1000-nm long-pass filters).

Ex vivo imaging of whole mice and excised organs

Male or female C57BL/6J mice were euthanized at 6 weeks old, had their hair removed, and were imaged in different positions using illumination at 892 nm, after which numerous tissues and organs were excised and imaged *ex vivo*. A similar procedure was used to image male and female 6-week-old C57BL/6J mice and Ob/Ob mice and their excised livers. To image lymph nodes in adipose tissue, a male 6-week-old C57BL/6J mouse was euthanized and imaged using illumination at 938 nm.

The Raman contrast of CH and OH was compared to autofluorescence by euthanizing male and female 4-week-old C57BL/6J mice, then imaging them followed by imaging their excised organs after illumination at 785, 892, 938, 968, or 1064 nm. Specific filters used in combination with these lasers are listed in the figure captions.

In vivo imaging of changes in mouse adipose tissue induced by fasting and refeeding

Female 8-week-old athymic mice had *ad libitum* access to food, whereupon they were anesthetized as described above and imaged using illumination at 938 nm. Then animals were returned to their home cages and fasted for 24 h. The animals were imaged again, returned to their cages and given *ad libitum* access to food. At 24 and 48 h later, the animals were imaged.

Ratiometric CH/OH contrast mapping

To visualize the local balance between CH- and OH-rich regions, a signal-weighted CH/OH contrast image was generated from the two Raman-band images. Prior to ratio calculation, both the CH and OH images (I_{CH} and I_{OH}, respectively) were processed using a 3x3 median filter (equivalent to a radius of 1 pixel in ImageJ) to reduce noise while preserving spatial boundaries.

A pixel-wise unweighted CH/OH ratio (R) was calculated as:

$$R = \frac{I_{CH}}{I'_{OH}}$$

where I'_{OH} represents the intensity of the OH image matrix conditioned to avoid division-by-zero errors in background regions, such that $I'_{OH} = I_{OH}$ for all pixels where $I_{OH} \geq 10^{-6}$, and $I_{OH} = 10^{-6}$ otherwise.

To further suppress noise amplification in low-intensity regions, a well-documented artifact of ratiometric imaging in which division by small numbers causes deceptively large ratio values [64], this initial ratio image was weighted by the normalized combined signal intensity of both bands. The weighting factor was defined as:

$$w = \left(\frac{I_{CH} + I_{OH}}{\max\,(I_{CH} + I_{OH})}\right)^{0.5}$$

where the exponent of 0.5 corresponds to square-root weighing, and the denominator represents the global maximum pixel intensity found across the combined image matrix. The square-root

weighting was selected empirically to attenuate ratio values arising from weak signals, while avoiding the abrupt exclusion of pixels associated with threshold-based methods.

The final signal-weighted contrast ratio (WR) image was obtained by element-wise multiplication of the two matrices:

$$WR = R \cdot w$$

Finally, the resulting WR image was subjected to a second 3x3 median filtering step to further suppress residual pixel-level noise. Any non-finite values arising from numerical edge cases within the array were subsequently replaced with zero. All image processing and matrix manipulations were performed in Python using NumPy and SciPy.

Mouse MRI data acquisition

Whole-mouse MRI was performed on two freshly anesthetized mice (46- and 51-week-old female athymic nude) using a BioSpec 30/18 small-animal scanner (Bruker BioSpin MRI GmbH, Ettlingen, Germany) operating at 2.998 T (^{1}H Larmor frequency: 127.6 MHz). Images were acquired using a T2-weighted turbo RARE sequence with the following parameters: repetition time 3446 ms, echo time 50 ms, echo train length 8, number of averages 4, slice thickness 2.0 mm, inter-slice spacing 0.25 mm, in-plane resolution 0.219 × 0.323 mm (acquisition matrix 192 × 192, field of view 42 × 62 mm). A dedicated rodent RF coil (RF RES 128 1H 10) was used for signal reception. Water- and fat-dominated images were obtained using the modified two-point Dixon water-fat separation method (TurboRARE_fws sequence). Image reconstruction included estimation of local B0 field inhomogeneity (off-resonance frequency shifts) and correction of the associated phase errors during post-processing in ParaVision 360 (Bruker BioSpin), resulting in separate water-only and fat-only image datasets for subsequent comparison with SWIR Raman imaging data acquired in the same animals.

Human hand MRI acquisition and pre-processing

MRI of the human hand was acquired on a 3 T whole-body scanner (Biograph mMR, Siemens Healthineers, Erlangen, Germany) using a four-channel receive coil. The subject's left hand was positioned palm-down on the coil and immobilized with straps and sandbags to maintain a constant pose throughout the session. This immobilization, together with repositioning of the hand between MRI and Raman imaging setups, may have introduced minor differences in anatomical orientation. MRI images were acquired in both coronal and axial slice orientations and reconstructed at a slice thickness of 1.2 mm and an in-plane resolution of 0.43 mm. Coronal images match the view orientation of SWIR Raman imaging and sample the entire depth of the hand without gap. Axial slices were acquired with a 0.12 mm inter-slice gap (10%). Pixel bandwidth was 330 Hz/pixel with frequency encoding along the lateral direction in both orientations.

Fat and water images were obtained using a clinical two-point Dixon sequence, which exploits the small difference in resonance frequency of ^{1}H nuclei when they are bound in either water or lipid molecules. This shift is approximately 3.5 ppm between these two environments [65]; at 3 T it corresponds to approximately 440 Hz. The sequence was based on a T1-weighted spin echo readout (repetition time 750 ms, echo time 14 ms). A first signal was acquired approximately at the in-phase condition of water and the dominant fat resonance. A second echo was induced 1.1 ms later, when fat and water magnetization have attained roughly opposite phase (≈ 1/(2 × 440) s). Both water and fat contribute to the first image intensity (in-phase), while the second intensity (opposed phase) corresponds to their difference. Individual water and fat images were then

reconstructed by forming the sum and difference of in-phase and opposed phase images, respectively. It should be noted that their separation is approximate due to the multi-peak fat spectrum and the multitude of technical and subject-specific factors influencing the homogeneity of the magnetic field.

A chemical shift correction was applied to the fat images to correct for the spatial misregistration inherent to the Dixon acquisition. The difference in resonance frequency between fat and water protons causes a displacement along the frequency-encoding direction proportional to the ratio of frequency shift to pixel bandwidth. Given the configured pixel bandwidth of 330 Hz/pixel, the expected shift is approximately 1-2 pixels. Fat images were corrected by shifting them by two voxel widths in the lateral direction for both axial and coronal acquisitions. The correction magnitude was chosen by optimizing the visual correspondence of spongious bone (fat-dominated) and surrounding musculature (water-dominated), constrained to integer voxel shifts to avoid interpolation artefacts.

Dixon MRI intensity calibration

Voxel intensities in the Dixon MRI images were calibrated to approximate fractional water and fat content using a phantom consisting of five tubes filled with defined agarose/peanut oil mixtures (**Fig. S 43**). The phantom was scanned immediately after the hand using the same Dixon sequence. Measured intensities in both channels showed an approximately linear relationship to the nominal fractional content, allowing a linear calibration to be applied to the *in vivo* images. This calibration was used to define a 10% fat fraction threshold for isolating adipose tissue in both the segmentation and the projection steps, and to guide the visual interpretation of tissue composition.

MRI surface reconstruction and depth-weighted projection

A surface representation of the imaged tissue volume was constructed to enable depth estimation for any voxel in the image volumes. The exterior surface was segmented from axial water images by applying an inclusive intensity threshold followed by manual cleanup. A smoothed mesh was generated in MITK Workbench (German Cancer Research Center, Heidelberg, Germany; v2018.04) by Gaussian blurring of the binary mask ($\sigma \approx 0.25$ voxel widths) and sampling into surface triangles using the Marching Cubes algorithm, which ultimately were decimated to 50% of their number. Binary surface volumes were then regenerated in the voxel geometries of both the axial and coronal images. For the coronal surface volume, the smoothed mesh was sampled at a vertical resolution of 0.1 mm (finer than the coronal slice thickness) to reduce discretization error in depth assignments while the coronal in-plane resolution was preserved.

Tissue depth beneath the surface (d) was defined for each voxel as the vertical distance to the topmost surface voxel directly above it. Depth-weighted projection images were computed from the coronal stack by assigning each voxel an exponential weight $w = \exp(-d/\lambda)$, with a decay length $\lambda = 2.5$ mm chosen to approximate the effective attenuation of the excitation-emission path in wide-field imaging. Weighted intensity sums were accumulated over all coronal slices separately for water and fat channels, yielding two-dimensional projection images. Water and fat projections underwent independent contrast adjustments to optimize visual correspondence with SWIR Raman data. This procedure was applied identically to human and mouse MRI data.

MRI structure segmentation

Subcutaneous fat deposits and surface blood vessels were segmented in axial images to serve as anatomical landmarks identifiable in both MRI and SWIR Raman imaging. All segmentations

were performed in MITK Workbench. Subcutaneous fat was delineated in calibrated fat images using the 10% fat fraction threshold with subsequent removal of spongious bone signal. Bone was segmented using a visually adjusted intensity threshold with manual anatomical refinement, then isotropically dilated by two voxel widths to fully encompass the cortical boundary and suppress spongious fat signal within the mask. The dilated bone mask was subtracted from the threshold-based fat segmentation to yield the final subcutaneous fat label (**Fig. S 44**). Surface blood vessels were identified in axial water images as small, approximately circular regions of elevated signal or signal void, consistent with flow enhancement or saturation of inflowing blood, respectively (**Fig. S 44**). Pulsation artefacts, represented as ghosting of vessel signal along the phase-encoding direction, provided an additional detection cue. Only structures traceable through at least three contiguous axial slices in both the proximal and distal directions were retained to reject spurious detections.

Cell culture conditions

The cell line 4T1 was purchased from the American Type Culture Collection (ATCC) (catalog no. CRL-2539). The cells were cultured in RPMI 1640 medium (catalog no. 11875093, Thermo Fisher Scientific) supplemented with 10% fetal bovine serum (catalog no. F4135, Sigma-Aldrich), 100 units ml^{-1} penicillin and 100 µg ml^{-1} streptomycin, at 37 °C in an atmosphere of 20% O_2 and 5% CO_2.

Generation of 4T1-iRFP720 cell line

Cultured 4T1 cells underwent an antibiotic kill curve assay employing varying concentrations of Geneticin G418 antibiotic (catalog no. 2039.2, Carl Roth) to determine the optimal selection conditions (G418 concentration ranging from 0 to 1000 µg/ml). The concentration resulting in complete cell death within a week (200 µg/ml) was selected. Subsequently, the cells were transfected with pCDNA3.0-iRFP720, which contains a neomycin gene conferring resistance to G418. The iRFP720 construct, optimized for mammalian codons, was obtained from Thermo Fisher Scientific and subcloned into pCDNA3.0. Transfection was performed using the Neon transfection system (Thermo Fisher Scientific). Following transfection, the cells were exposed to G418 for 7 days to select for those successfully incorporating the cassette. Afterwards, the cells were cultivated, and single-cell sorting was performed by gating the top 10% of 4T1 cells exhibiting high fluorescent intensity using a FACS Aria III (BD Bioscience). Selected cells were expanded for 2 weeks. Subsequently, individual clones were analyzed for the highest fluorescent intensity using a fluorescence microscope, and the superior clone was selected for further expansion. Once expanded, the chosen clone was cryopreserved in 5% dimethyl sulfoxide complete RPMI freezing medium (catalog no. R8758, Sigma-Aldrich).

Imaging of tumor growth in mice

For the tumor cell implantation, 4×10^5 cultured 4T1 or 4T1-iRFP cells were resuspended in 50 µL phosphate-buffered saline, and injected subcutaneously onto the flank of 7-week-old female athymic nude mice. After implantation, the mice were anesthetized and imaged in the wide-field SWIR Raman imaging setup upon 892 nm illumination. For iRFP excitation, 672 nm was used, and its emission tail was detected in the same setup using an 1100-nm long-pass filter. Imaging was performed daily.

Whole-body imaging of mice fed a choline-deficient high fat diet

Four male 7-week old C57BL/6N mice were fed a diet deficient in methionine and choline (catalog no. A06071302, Research Diets) for 6 weeks, at the end of which the mice were euthanized and their corpses were frozen at -80 ºC until analysis. Four littermates were fed standard chow as a control (catalog no. 1314, Altromin). The corpses were thawed, had their hair removed, positioned in the SWIR Raman imaging setup, and imaged using 938 nm illumination.

Imaging of dissected fatty liver from mice

Male 8-week old C57BL/6N mice were fed either a diet deficient in methionine and choline (catalog no. A06071302, Research Diets) for 7 weeks or a diet containing 60% kcal% fat (catalog no. D12492, Research Diets) for 16 weeks. As controls, mice were fed standard chow. Six mice per group were utilized. Mice were euthanized at the end of the diet protocol, after which the ones from the group receiving a high-fat diet and the corresponding controls were perfused with phosphate-buffered saline. Livers were removed from all animals and a piece of tissue was excised, weighed, snap-frozen in liquid nitrogen, and stored at -80 ºC until analysis. Livers were thawed on ice and imaged using illumination at 1064 nm. Images were flatfield-corrected. In the CH region images, we drew regions of interest covering the entire sample and, in order to subtract background laser counts, four regions of interest covering areas surrounding the sample.

Imaging of atherosclerotic plaques in human arteries

Surgical biopsies from women 72-81 years old with high-grade stenosis who underwent carotid or iliofemoral endarterectomy were obtained. Biopsies were placed in ice-cold phosphate-buffered saline, excised at the largest site of the plaque, snap-frozen in liquid nitrogen and stored at -80 ºC until analysis. Samples were thawed and imaged using illumination at 1064 nm.

To assess the specificity of the calcification signal, surgical biopsies were imaged before and after 10% neutral buffered formalin fixation (catalog no. HT501128, Merck), followed by 14-day decalcification with Osteosoft (catalog no. 101728, Sigma-Aldrich).

Histological analysis

Mouse liver specimens were fixed in 4 % (w/v) neutrally buffered formalin, embedded in paraffin, and cut into 3 µm sections. Human atherosclerotic lesions were fixed in 4 % (w/v) phosphate-buffered paraformaldehyde, decalcified, embedded in paraffin, and cut into 5 µm sections. Sections from both types of tissues were stained with hematoxylin and eosin (HE), using a HistoCore SPECTRA ST automated slide stainer (Leica Biosystems) according to the manufacturer's instructions. Stained tissue sections were scanned with an AxioScan 7 digital slide scanner (Zeiss, Oberkochen, Germany) equipped with a 20x magnification objective.

Statistical analysis

Differences between groups were statistically analyzed using an unpaired, two-tailed t test. $P < 0.05$ was considered significant. All analyses were performed using GraphPad Prism v. 10.2.2. Data are represented as mean ± SD.

Porcine tissue and animal procedures

Porcine tissue was obtained from two sources. Head and neck specimens (obtained as a single anatomical piece) and brain samples were obtained from a local slaughterhouse and kept at 4°C. For the facial nerve experiments, the nerve was carefully exposed *in situ* and subsequently subjected to imaging either in the laboratory or in the experimental operating room at NCT/UCC

Dresden. For intraoperative setting validation, a freshly euthanized minipig, used in an unrelated terminal study, was imaged directly after euthanasia in the experimental operating room at NCT/UCC Dresden. Resected lymph nodes were subsequently processed for histological analysis.

Live animal experiments were performed on a female Deutsche Landrasse pig (2.2 months, 37.1 kg). After anesthesia, the animal was positioned on the operating table and the abdomen was opened for intraoperative imaging in an open surgical model. Surgical procedures including mesenteric lymph node resection were performed during the imaging session.

Human body donor

Lymph node identification in the inguinal region was performed on a human body donor in the experimental operating room at NCT/UCC Dresden, under the same imaging conditions as the porcine experiments.

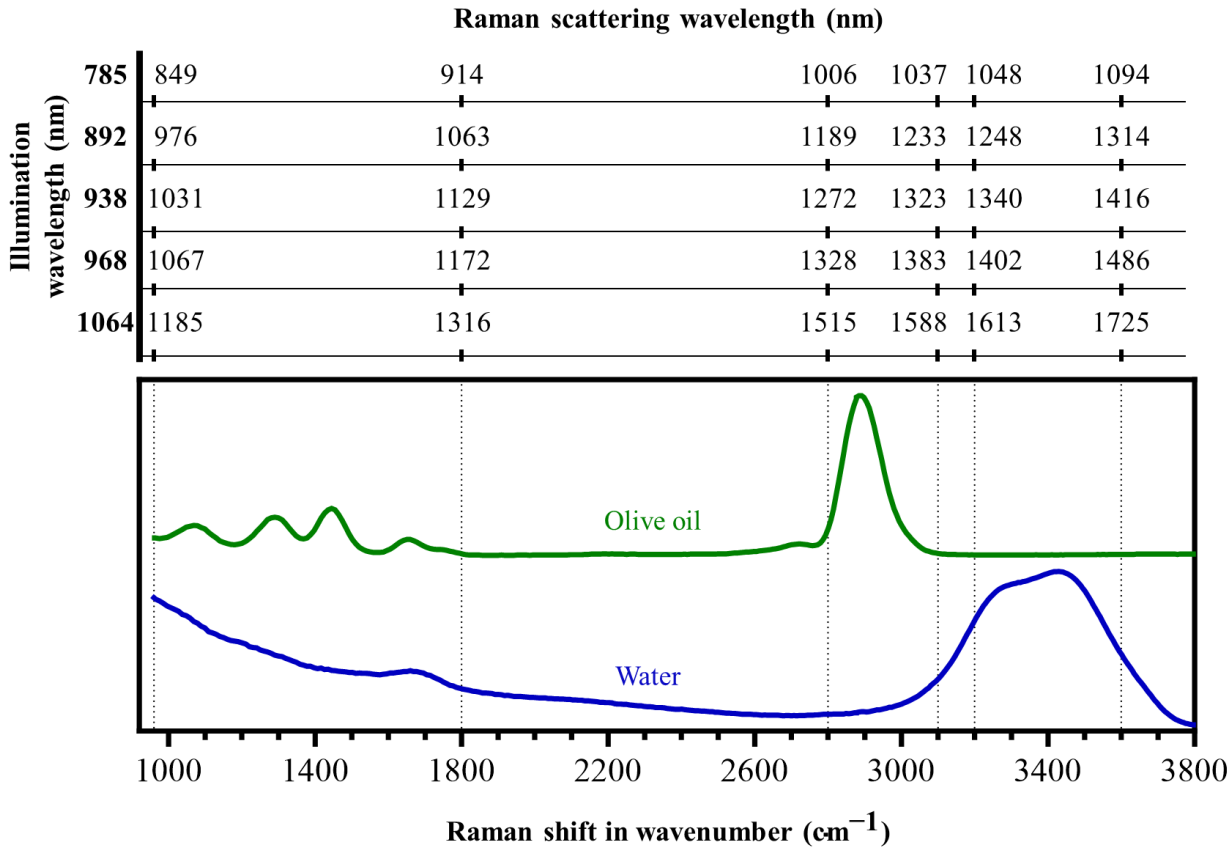


Fig. S 1. Raman shift conversion from wavenumber to wavelength. Raman spectrum of olive oil and water acquired with 892 nm illumination and represented in wavenumbers in the lower (primary) x-axis. Following Equation 1, the primary x-axis was converted to the Raman wavelength shift for each illumination wavelength used in this work and displayed in the upper (secondary) x-axis. Arbitrary boundaries of the fingerprint (960 to 1800 cm^{-1}), silent (1800 to 2800 cm^{-1}), CH (2800 to 3100 cm^{-1}), and OH (3200 to 3600 cm^{-1}) Raman regions were selected (dashes vertical lines) to illustrate the shifts in wavelengths.

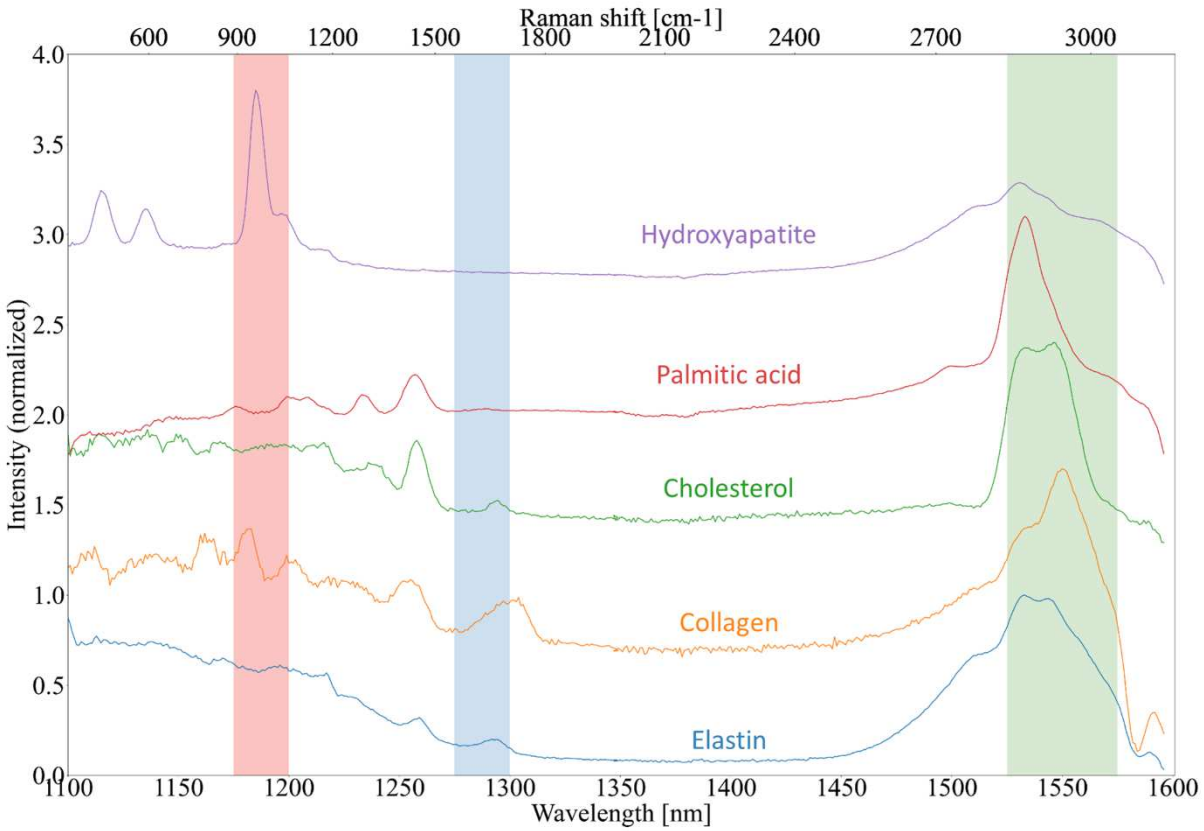


Fig. S 2. Raman spectra of calcification-associated hydroxyapatite, the lipids palmitic acid and cholesterol, as well as the proteins collagen and elastin measured using illumination at 1064 nm. The primary (lower) x-axis displays the spectra in the detected wavelength regime, whereas the secondary (upper) x-axis represents the Raman shift upon 1064 nm illumination. The full-width at half-maximum of the band-pass filters used in Fig. S 3 to detect the PO_4^{-3}, Amide I, and CH bands are labeled in red, green, and blue, respectively.

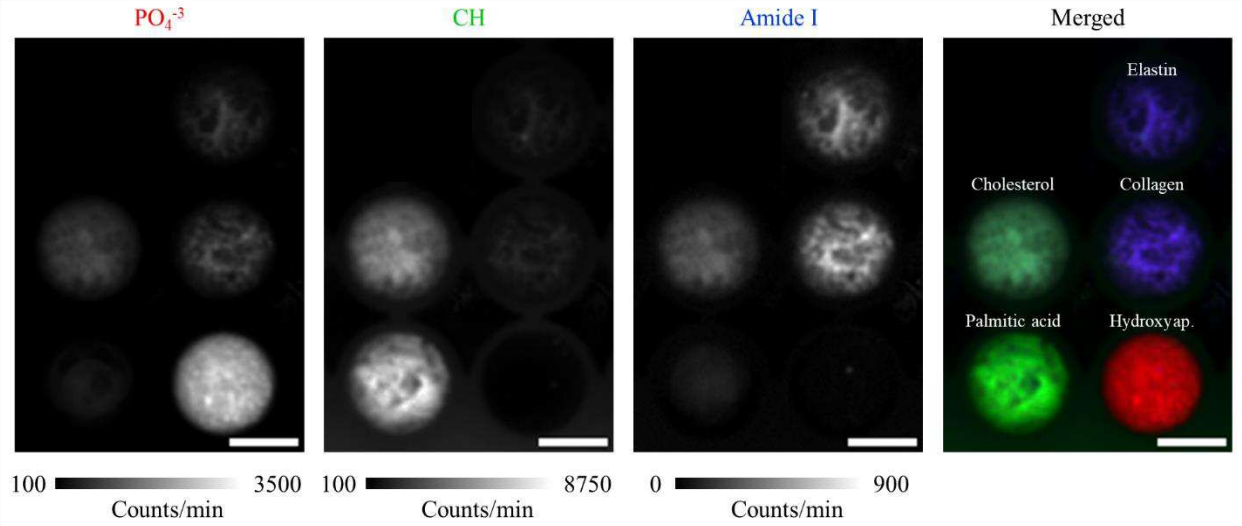


Fig. S 3. SWIR Raman imaging of the compounds from Fig. S 2. The powder compounds were placed into a black polystyrene 96-well plate, and imaged in the SWIR Raman setup upon illumination at 1064 nm. Hydroxyap.: hydroxyapatite. Images were acquired using System 1 in free-run mode. Imaging parameters: 1064 nm (177 mW/cm²) illumination, 300 s per-frame exposure; band-pass filters: PO_4^{3-}: BP1187.5-25, Amide I: BP1287.5-25, CH: BP1550-50. Scale bars: 0.5 cm.

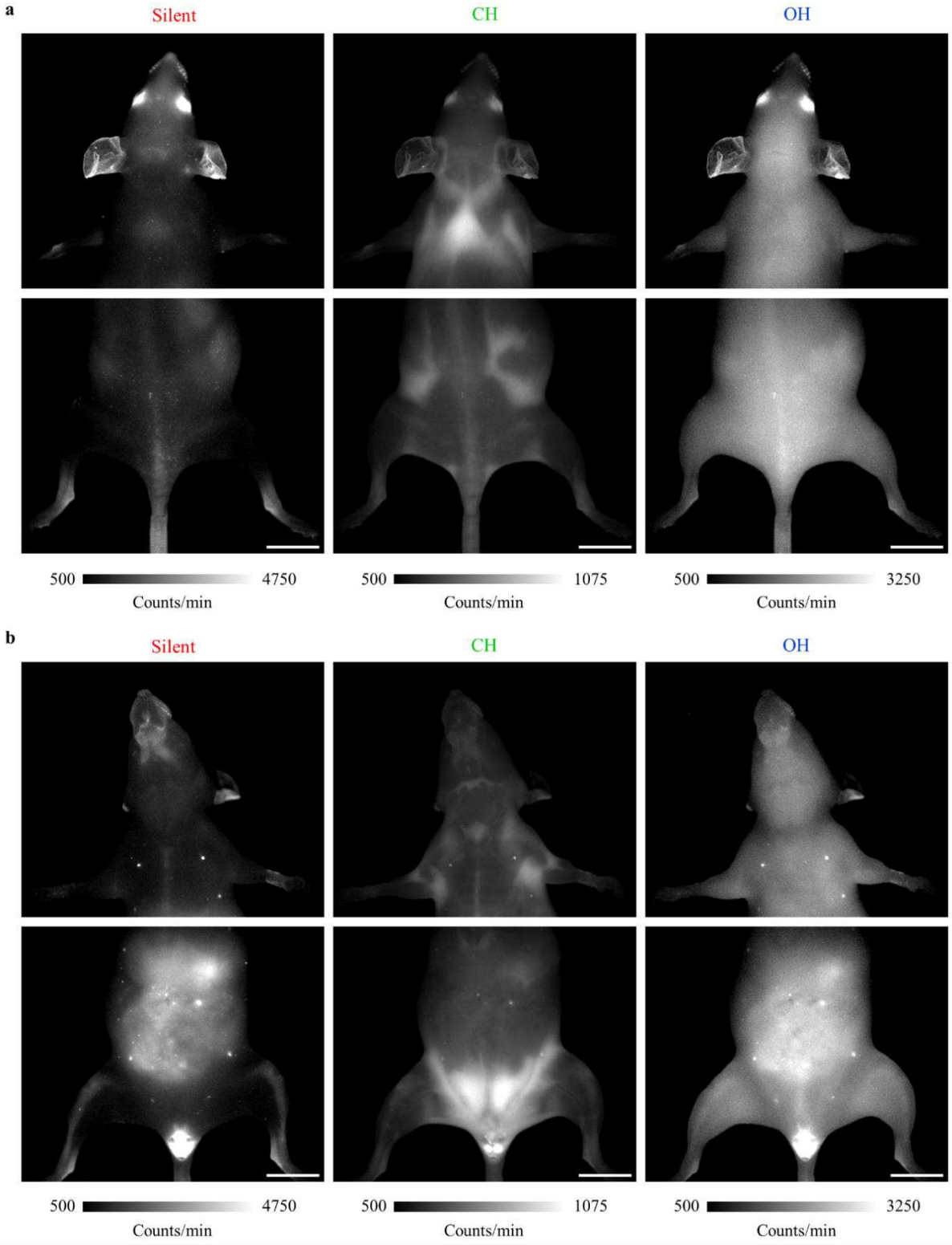


Fig. S 4. Single-band images of the **(a)** dorsal and **(b)** ventral views of the mouse shown in Figure 1 d. Images were acquired using System 1 in free-run mode. Imaging parameters: 892 nm (152 mW/cm²) illumination, 10 s per-frame exposure; band-pass filters: silent: BP1150-25, CH: BP1200-25, OH: BP1300-25. Scale bars: 1 cm.

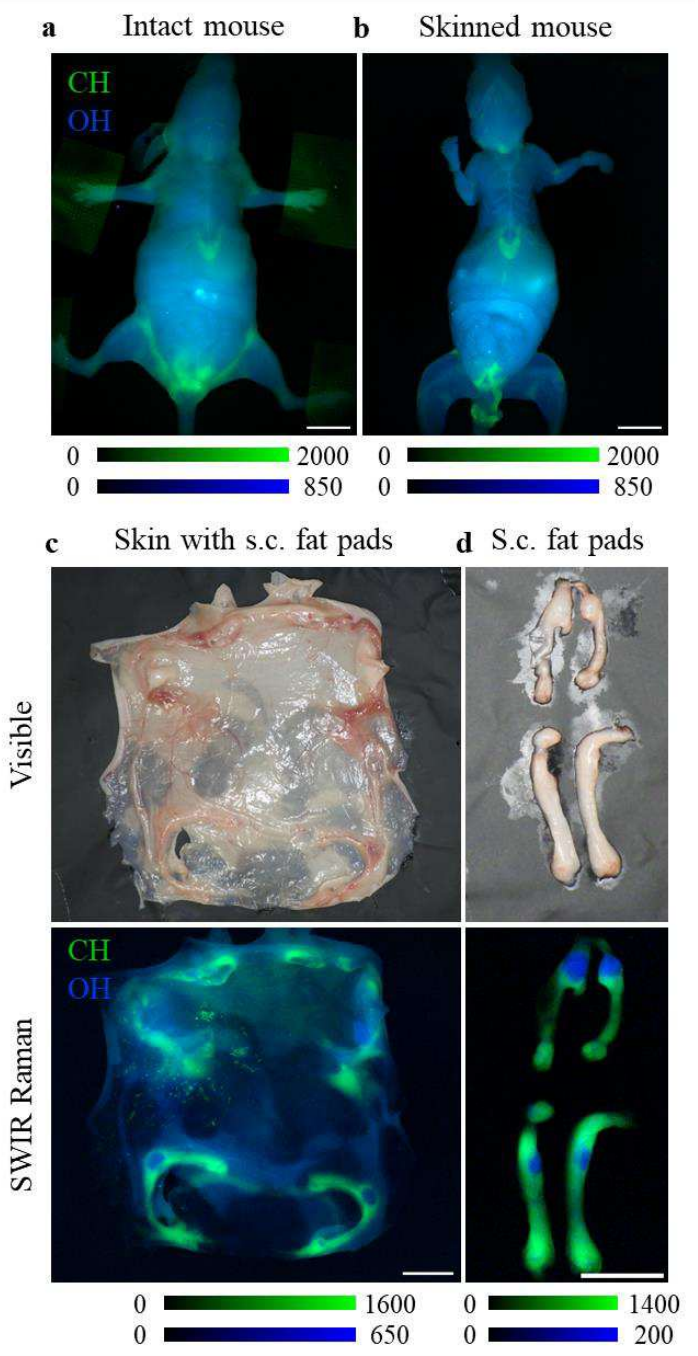


Fig. S 5. Dissection confirms CH contrast co-localizes with subcutaneous adipose tissue. **a-b)** SWIR Raman images of an intact mouse (a) and the same animal after skin removal (b), showing that subcutaneous CH-high regions disappear upon skin removal while OH signal persists body-wide. **c-d)** Visible-light photographs (top) and corresponding SWIR Raman images (bottom). (c) Excised skin with attached subcutaneous fat pads. (d) Isolated fat depots after separation from the skin. Lymph nodes embedded in the fat pads are also visualized based on their OH contrast in panel (d). Images were acquired using System 1 in free-run mode. Imaging parameters: 938 nm (96 mW/cm²) illumination, 60 s per-frame exposure; band-pass filters: CH: BP1287.5-25, OH: BP1362.5-25. Scale bars: 1 cm.

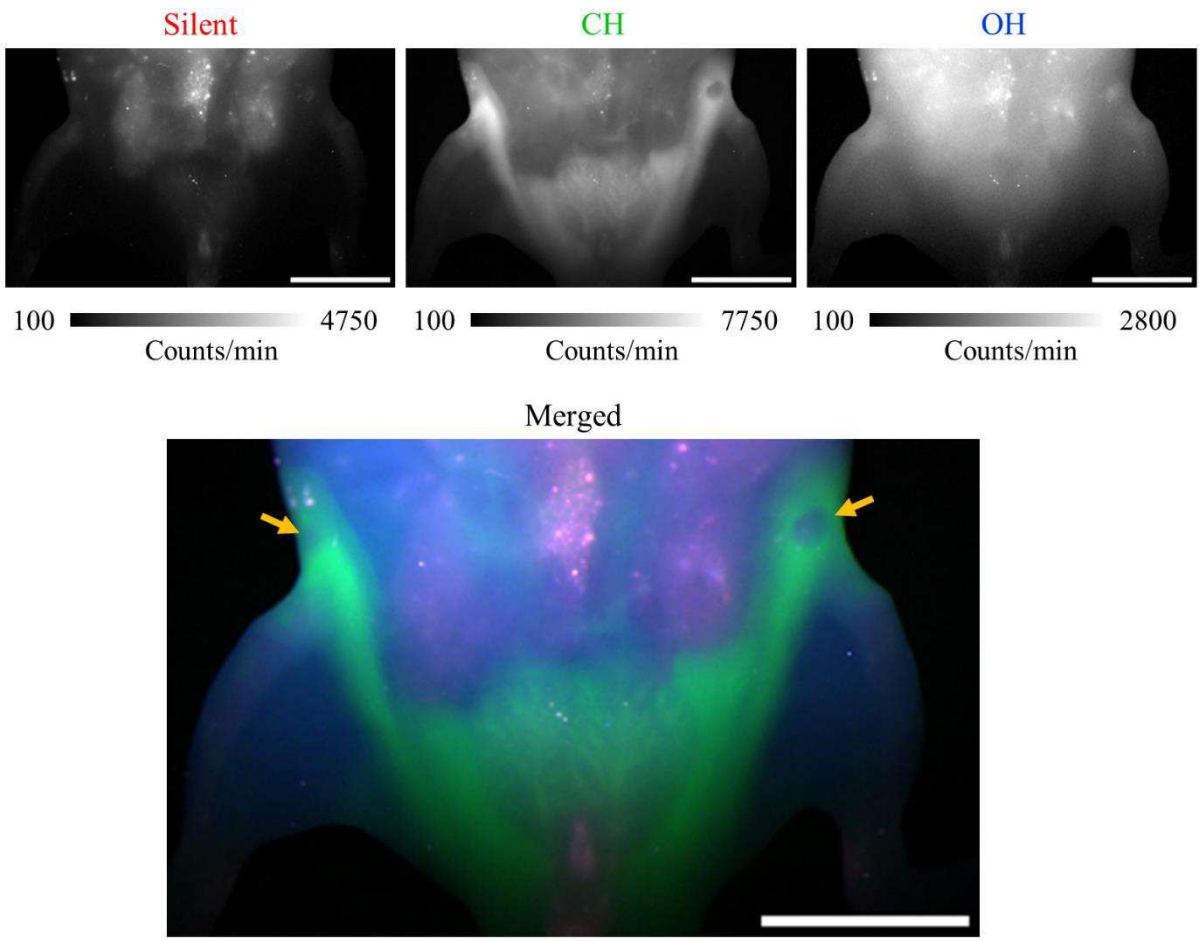


Fig. S 6. Non-invasive inguinal lymph node (indicated by the yellow arrows) visualization in an intact C57BL/6J mouse based (ventral view) on SWIR Raman chemical contrast upon 938 nm illumination. Images were acquired using System 1 in free-run mode. Imaging parameters: 938 nm (153 mW/cm²) illumination, 30 s per-frame exposure; band-pass filters: silent: BP1175-50, CH: BP1300-50, OH: BP1350-50. Scale bars: 1 cm.

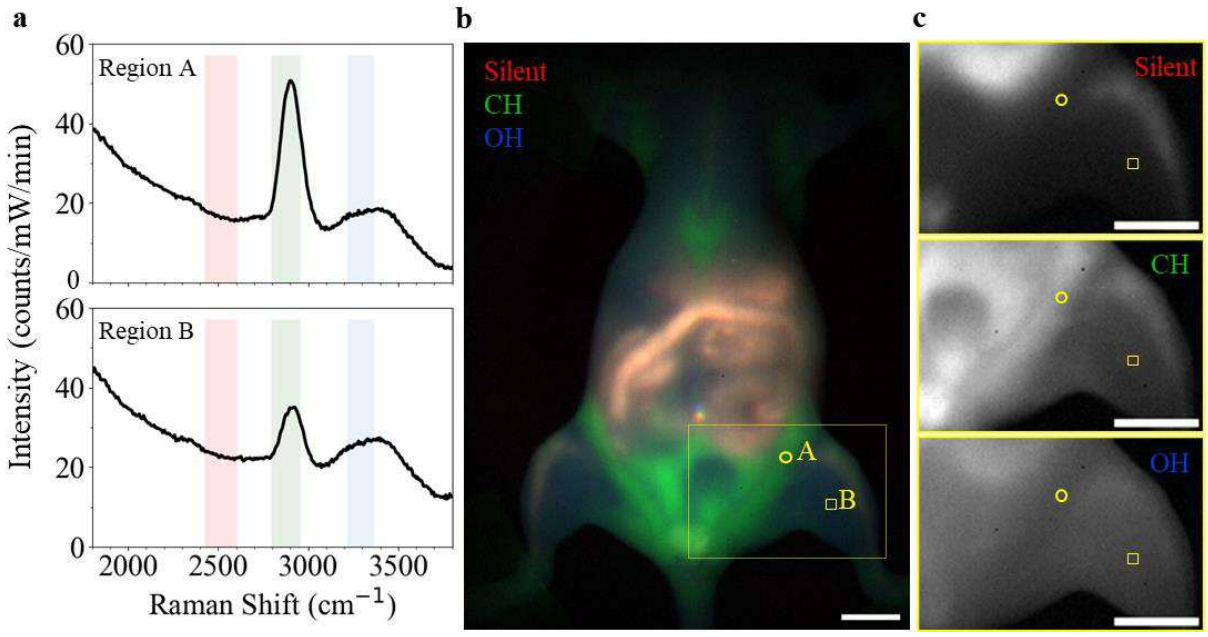


Fig. S 7. *In vivo* spectra confirm the Raman scattering origin of SWIR image contrast. **a)** Emission spectra acquired from two anatomical regions in an anesthetized mouse at 892 nm excitation and InGaAs detection. Region A (circle) overlies subcutaneous inguinal white adipose tissue (iWAT); Region B (square) overlies hindlimb skeletal muscle. Both regions include the contribution of Raman signal from skin in addition to the subcutaneous target tissue. Shaded bands indicate the transmission windows of the band-pass filters used in the wide-field imaging system. Region A shows a prominent CH-band peak (~2900 cm^{-1}) consistent with lipid-rich adipose tissue; Region B exhibits a dominant OH-band (between ~3200-3500 cm^{-1}) signal consistent with the high-water content of muscle. **b-c)** Wide-field SWIR Raman images of the same mouse acquired in the silent, CH, and OH bands, shown as (b) a composite overlay and (c) as individual grayscale channel images. The inset box (yellow) indicates the zoomed region shown in the single-channel panels. Circles and squares denote spectral acquisition locations corresponding to Regions A and B. Images were acquired using System 2 in free-run mode. Imaging parameters: 892 nm (233 mW/cm²) illumination, 1000 ms per-frame exposure; band-pass filters: silent: BP1150-25, CH: BP1200-25, OH: BP1262.5-25. Scale bars: 1 cm.

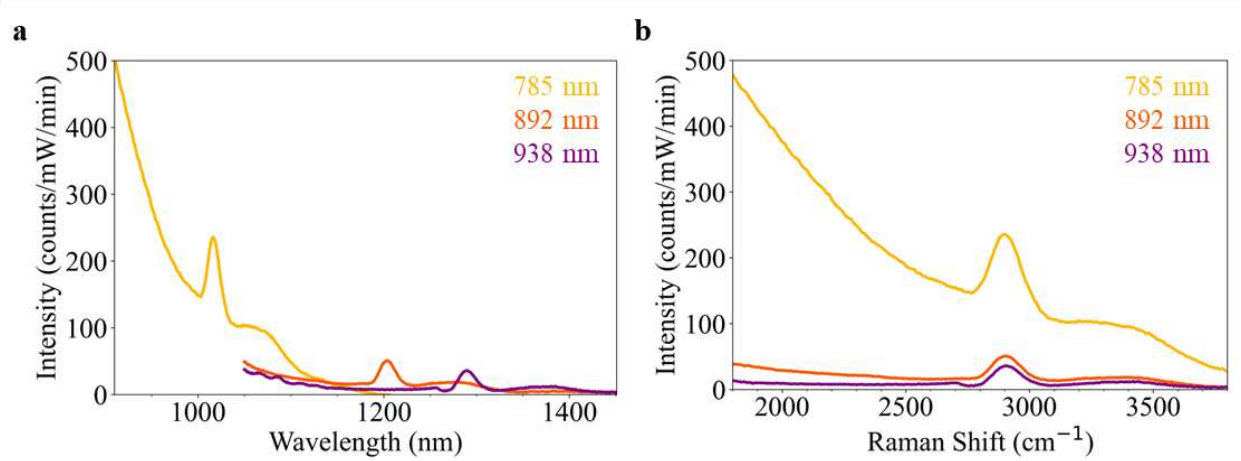


Fig. S 8. Raman spectra from skin overlying adipose tissue across three excitation wavelengths. **a)** Emission spectra acquired from Region A of Fig. S 7 (skin overlying iWAT) at 785, 892 and 938 nm excitation, plotted as a function of emission wavelength. The CH and OH Raman bands shift to longer wavelengths with increasing excitation, as expected for Raman scattering, confirming their Raman rather than fluorescence origin. **b)** The same spectra replotted in Raman shift (cm^{-1}), where Raman bands align across excitation wavelengths. At 785 nm, a strong broadband autofluorescence background dominates the emission, which is suppressed at 892 and 938 nm.

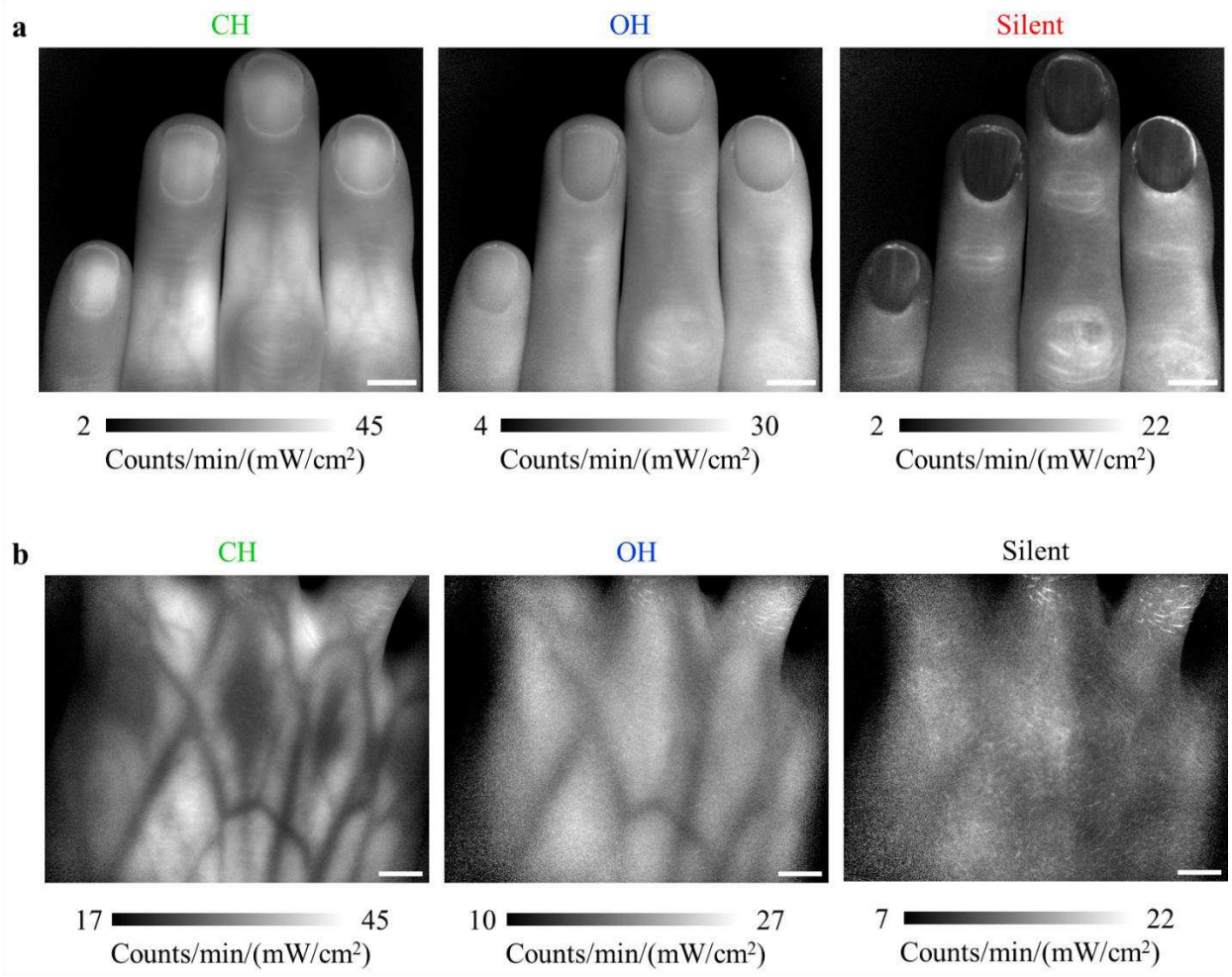


Fig. S 9. Single-band images of the human hands shown in **(a)** Figure 1 e and **(b)** Figure 1 f. The silent region of panel (b) was not shown in Figure 1 f because the autofluorescence mostly originated from the skin surface, thus impairing the visualization of the subcutaneous structures from the CH and OH Raman bands in the multicolor image. Images were acquired using System 1 in free-run mode. Imaging parameters: (a) 938 nm illumination (115 mW/cm²), 30 s exposure; filters: BP1200-25 (silent), BP1287.5-25 (CH), BP1350-50 (OH). (b) as (a), 10 s exposure. Scale bars: 1 cm.

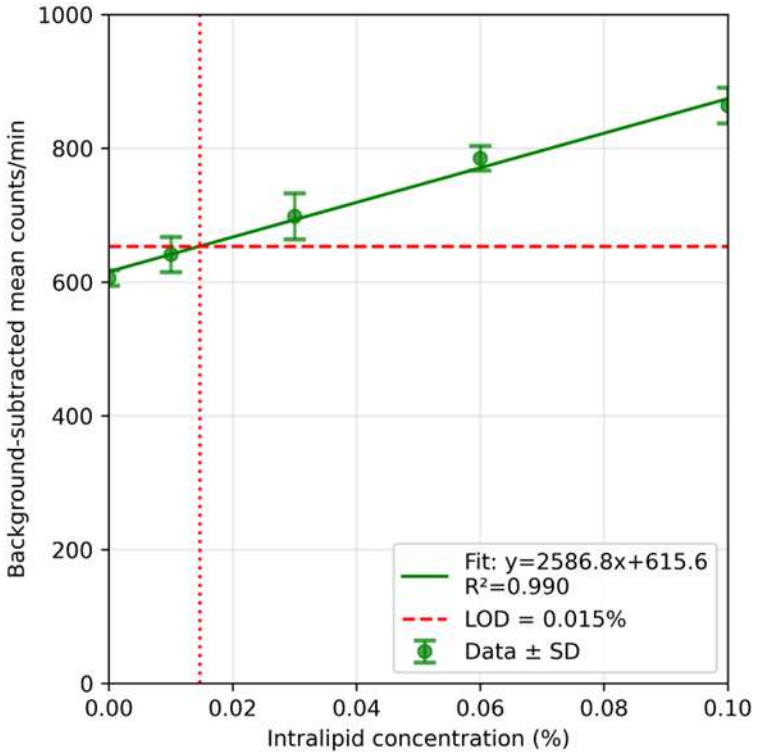


Fig. S 10. Sensitivity characterization of SWIR Raman imaging. Background-subtracted CH-band signal (BP 1200-25, 892 nm excitation) as a function of Intralipid concentration across the linear regime (0-0.1% v/v) where sample attenuation is negligible. A linear fit ($R^2 = 0.990$) was used to calculate the limit of detection (LOD) as $3.3 \times \sigma_{blank} / slope$, where σ_{blank} is the standard deviation of the water blank, yielding LOD = 0.015% (v/v). Considering an average molar mass of a triglyceride as 850 g/mol, this corresponds to a lipid concentration on the order of 350 µM. Error bars represent standard deviation across three independent replicates (n = 3).

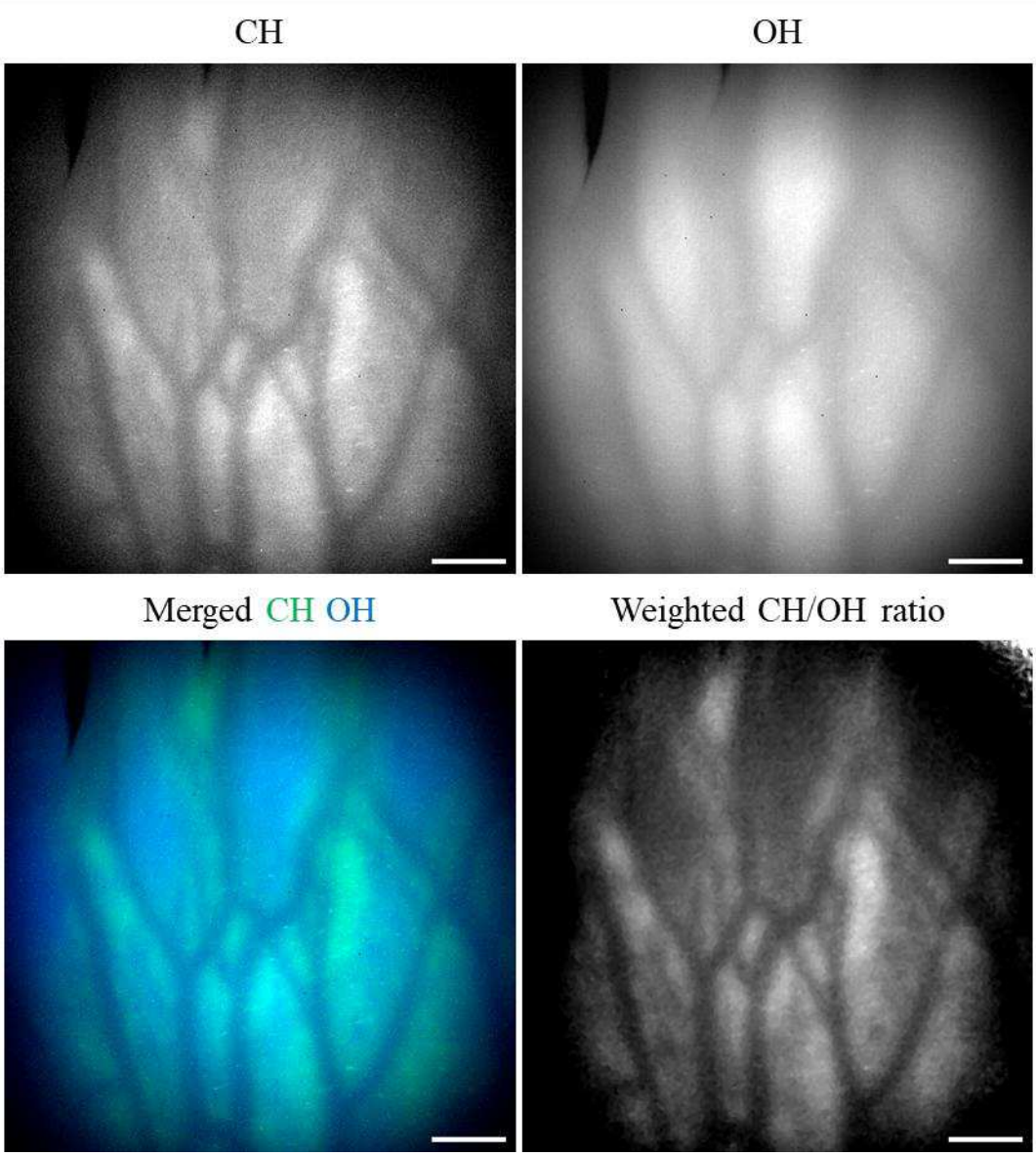


Fig. S 11. Single-channel and ratiometric CH/OH images of the human hand. SWIR Raman images of the dorsal surface of a human hand. Top row: single-channel images of the CH and OH bands, showing that both signals are present throughout the imaged area. In the CH channel, subcutaneous fat pads are brighter than tendons; in the OH channel, tendons and muscles are brighter than fat pads, but the contrast between tissue types is less immediately apparent in either channel alone. Bottom left: merged CH and OH channels, in which the relative dominance of each band per tissue type becomes visually apparent. Bottom right: weighted CH/OH ratio image, which provides a single grayscale representation of the CH contrast observed in the merged image, and enhances the visibility of tissue boundaries that are ambiguous in the individual channels. Images were acquired using System 2 in free-run mode. Imaging parameters: CH: 936 nm (300 mW/cm²) illumination, 1 s per-frame exposure; band-pass filter: BP1275-50; OH: 892 nm (300 mW/cm²) illumination, 1 s exposure; filter: BP1275-50. Scale bars: 1 cm.

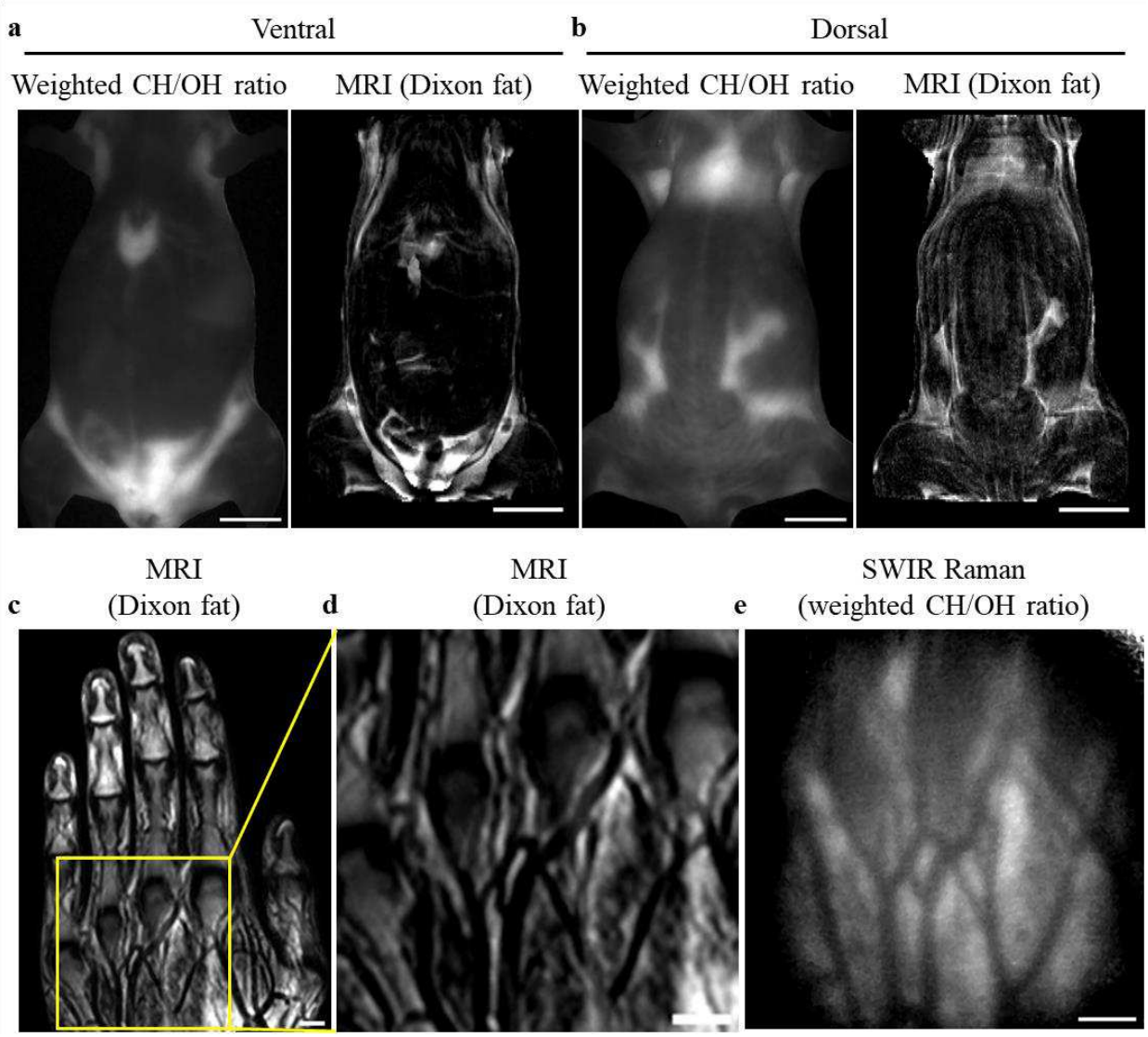


Fig. S 12. Cross-modality comparison of SWIR Raman and MRI in mice and humans. **a-b)** Weighted CH/OH ratio images of the (a) ventral and (b) dorsal surfaces of a freshly euthanized mouse alongside corresponding depth-weighted 2D fat projections from coronal MRI slices. **c-d)** 2D fat projection of coronal MRI slices of the human hand. (c) Full hand view. (d) Zoomed-in view of the indicated region in panel (c). **e)** Corresponding SWIR Raman weighted CH/OH ratio image acquired over the same anatomical region as in panel (d). CH/OH-bright regions in the Raman image match the distribution of fat-selective MRI signal across the dorsal hand. Minor differences in the apparent orientation of subcutaneous vessels between modalities likely reflect slight changes in hand positioning. The broad distribution of CH/OH-bright regions is nonetheless consistent across modalities. The original SWIR Raman images in panel (a) were acquired using System 1 in free-run mode: 938 nm (116 mW/cm²) illumination; band-pass (BP) filters: BP1287.5-25 (CH, 30 s exposure) and BP1350-50 (OH, 45 s exposure). For panel (b), images were acquired using System 2 in free-run mode: 1 s per-frame exposure with a single BP1275-50 filter used for both CH (936 nm illumination at 289 mW/cm²) and OH (892 nm at 258 mW/cm²) bands. Scale bars: 1 cm.

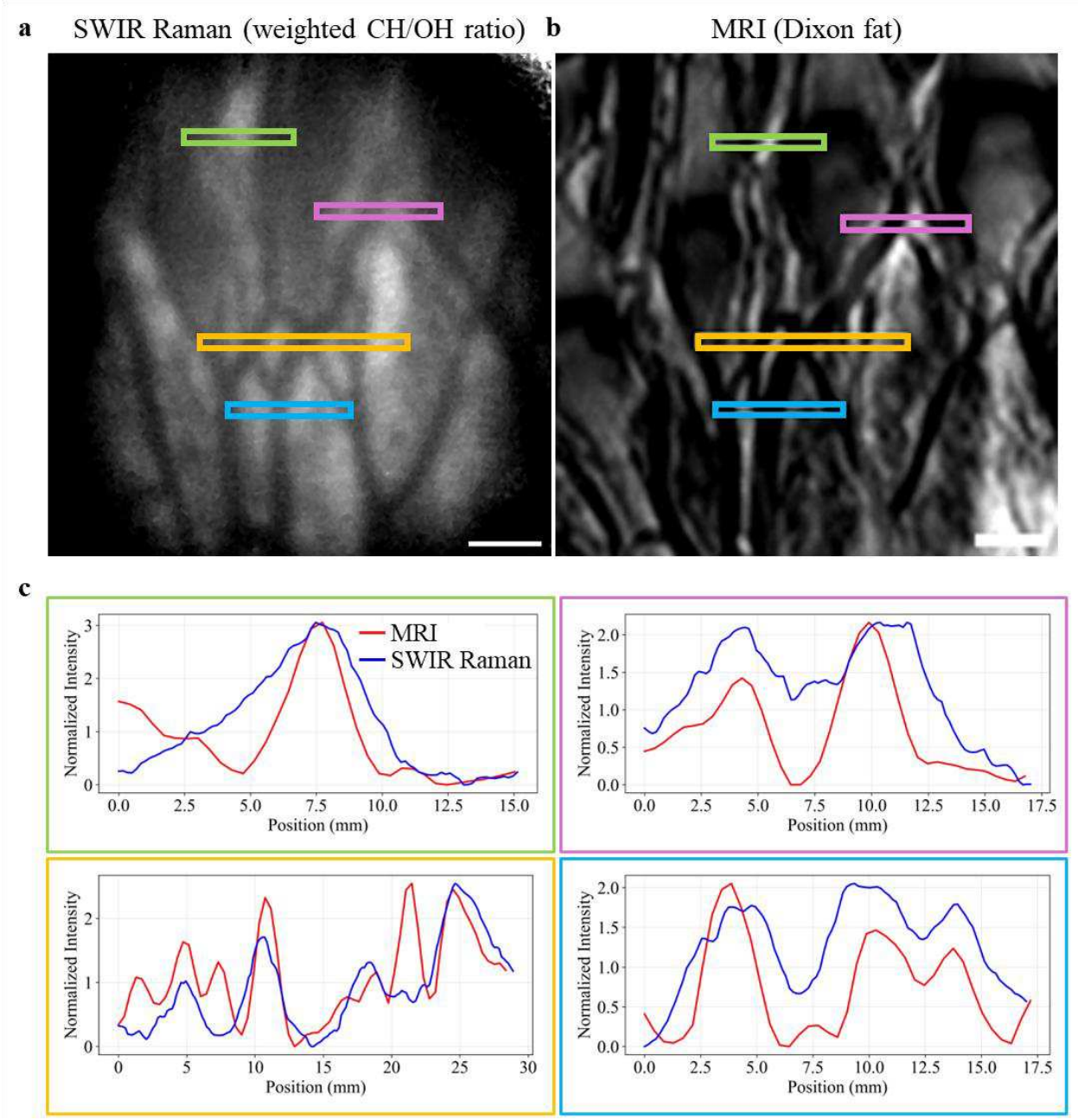


Fig. S 13. Line-profile comparison between MRI and SWIR Raman in the human hand. **a-c)** (a) Depth-weighted 2D fat projection of coronal MRI slices of the human hand. (b) CH/OH ratio image acquired over an equivalent field of view of the same hand, with four rectangular regions indicated (green, magenta, orange, cyan), from which the line profiles in panel (c) were extracted. Scale bars: 1 cm.

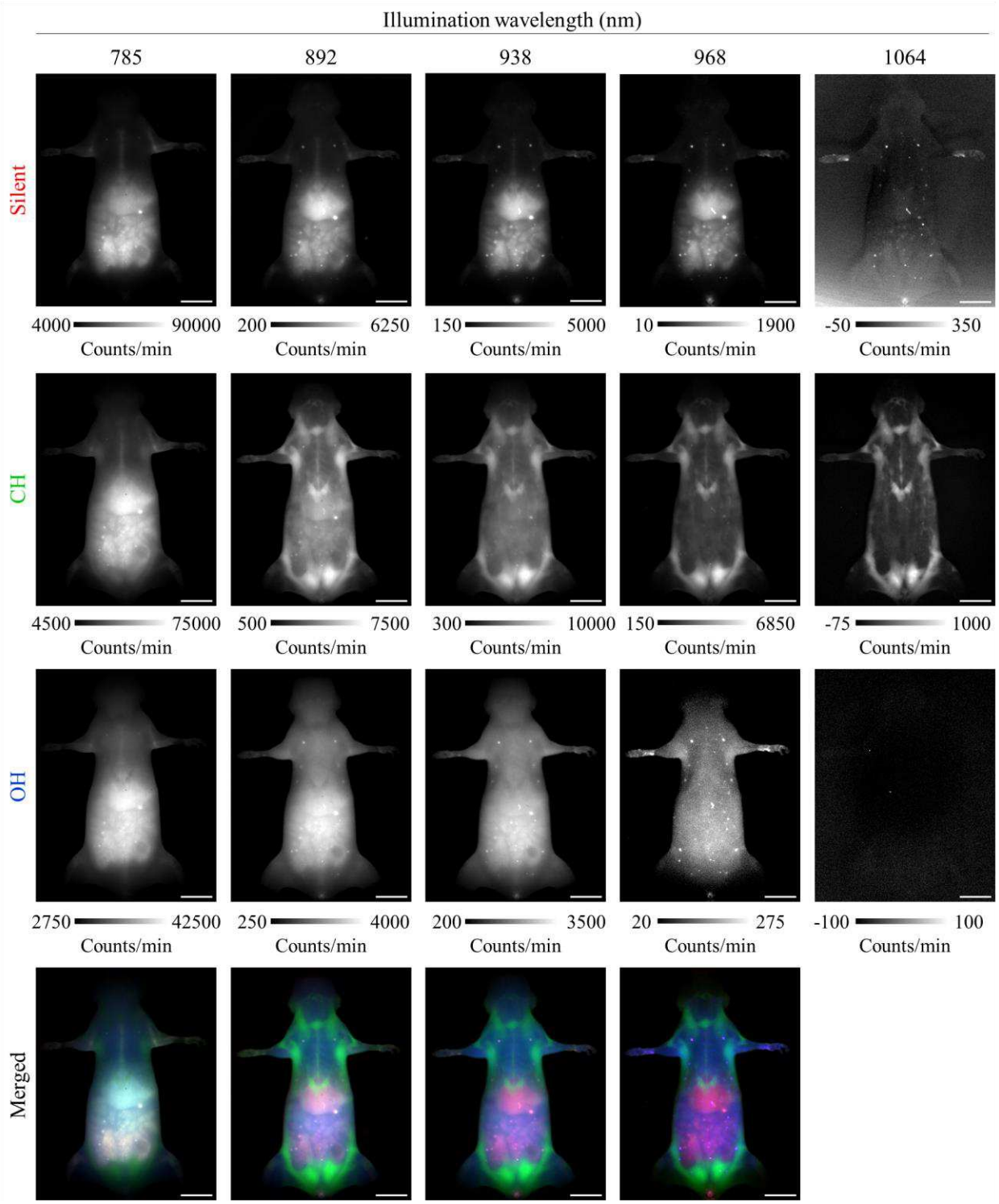


Fig. S 14. Single-band images of the mouse images shown in Figure 2 a-b (ventral view), with the addition of 1064 nm illumination, which was not shown in Figure 2 a as a merged image because its OH region lies beyond the detector limit. The data are representative of 2 mice. Imaging parameters are listed in the caption of Figure 2. Scale bars: 1 cm.

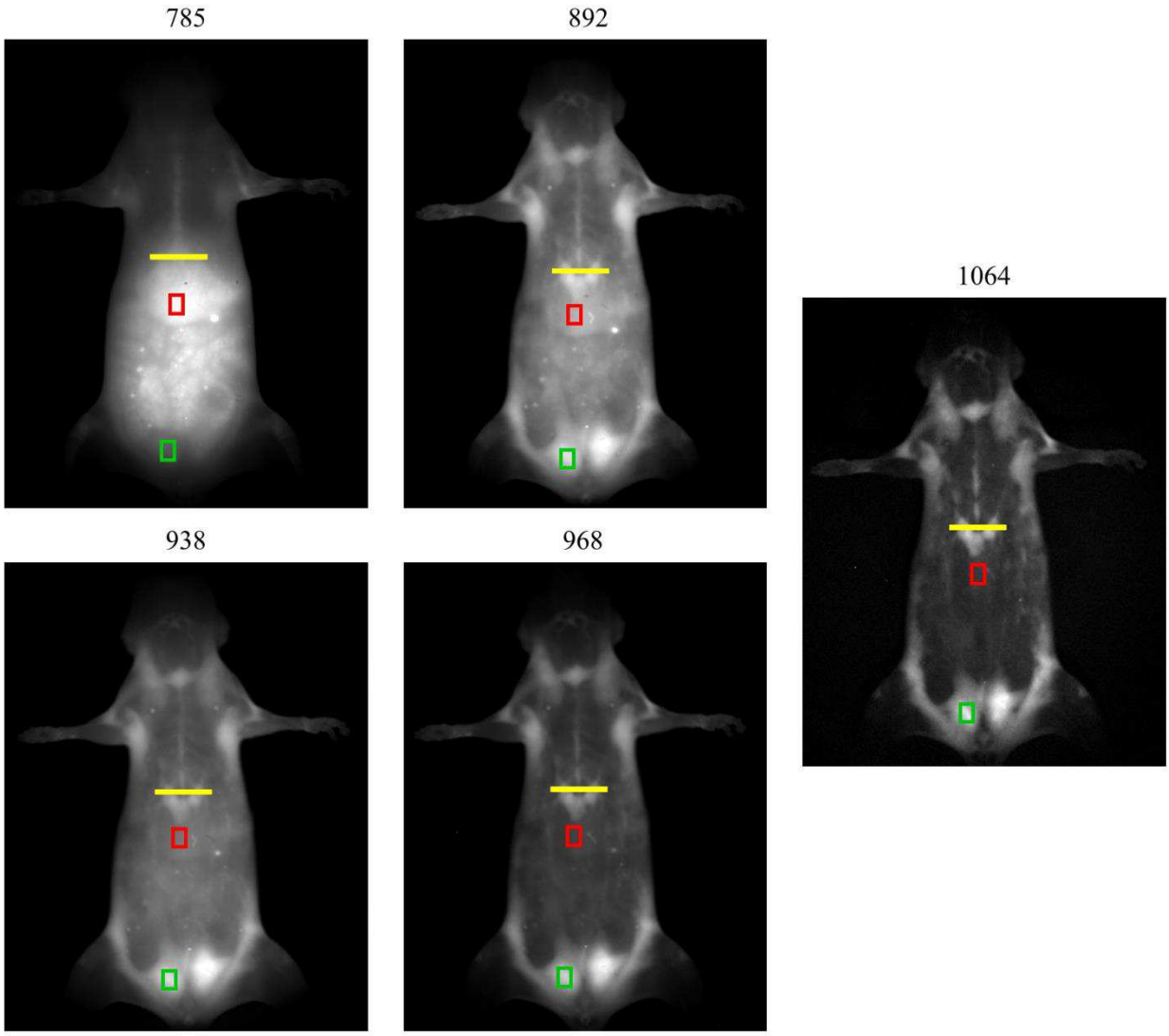


Fig. S 15. Regions of interest (ROIs) used for data extraction for Figure 2 c-d overlaid with the CH SWIR Raman images shown in Figure 2 b and Fig. S 14 (ventral view). The yellow line represents the ROI from which the line profiles shown in Figure 2 c were extracted. In addition, the red and green rectangles respectively represent the ROIs from which the mean values of fat pad and liver were extracted for Figure 2 d.

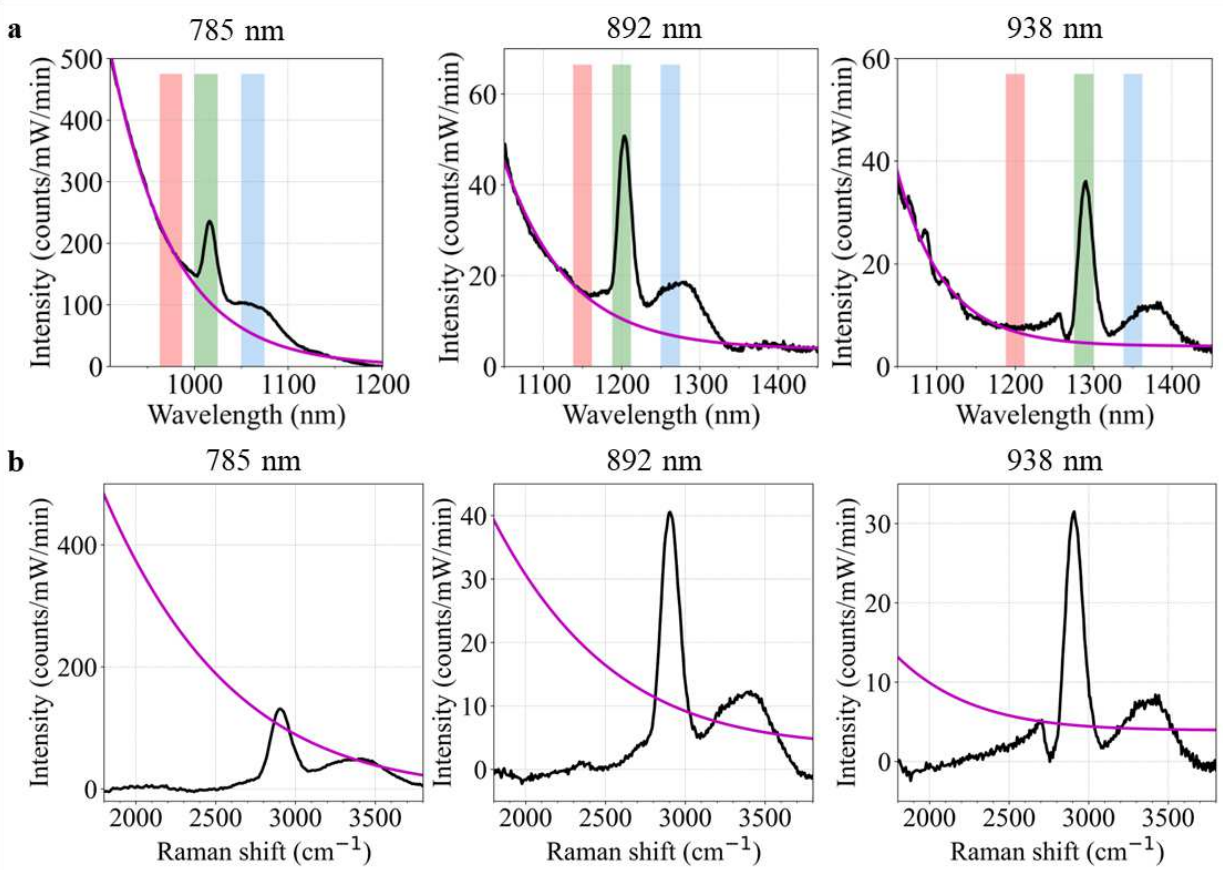


Fig. S 16. Autofluorescence fitting and Raman signal extraction from *in vivo* spectral measurements. **a)** Emission spectra from skin overlying adipose tissue at 785, 892, and 938 nm excitation (black curve, same data as Fig. S 8), with single-exponential fits (magenta) to the autofluorescence background. Fitting regions were selected in spectral windows free of Raman peaks: 910-980 nm and 1125-1200 nm for 785 nm excitation; 1050-1170 nm and 1350-1475 nm for 892 nm excitation; 1050-1225 nm and 1440-1475 nm for 938 nm excitation. Shaded bands indicate the transmission windows of the band-pass filters used in the wide-field imaging system (red: silent, green: CH, blue: OH). **b)** Background-subtracted Raman spectra obtained by subtracting the exponential fit from the measured emission spectra. The residual Raman component, comprising the CH and OH bands, becomes increasingly pronounced as the illumination wavelength increases.

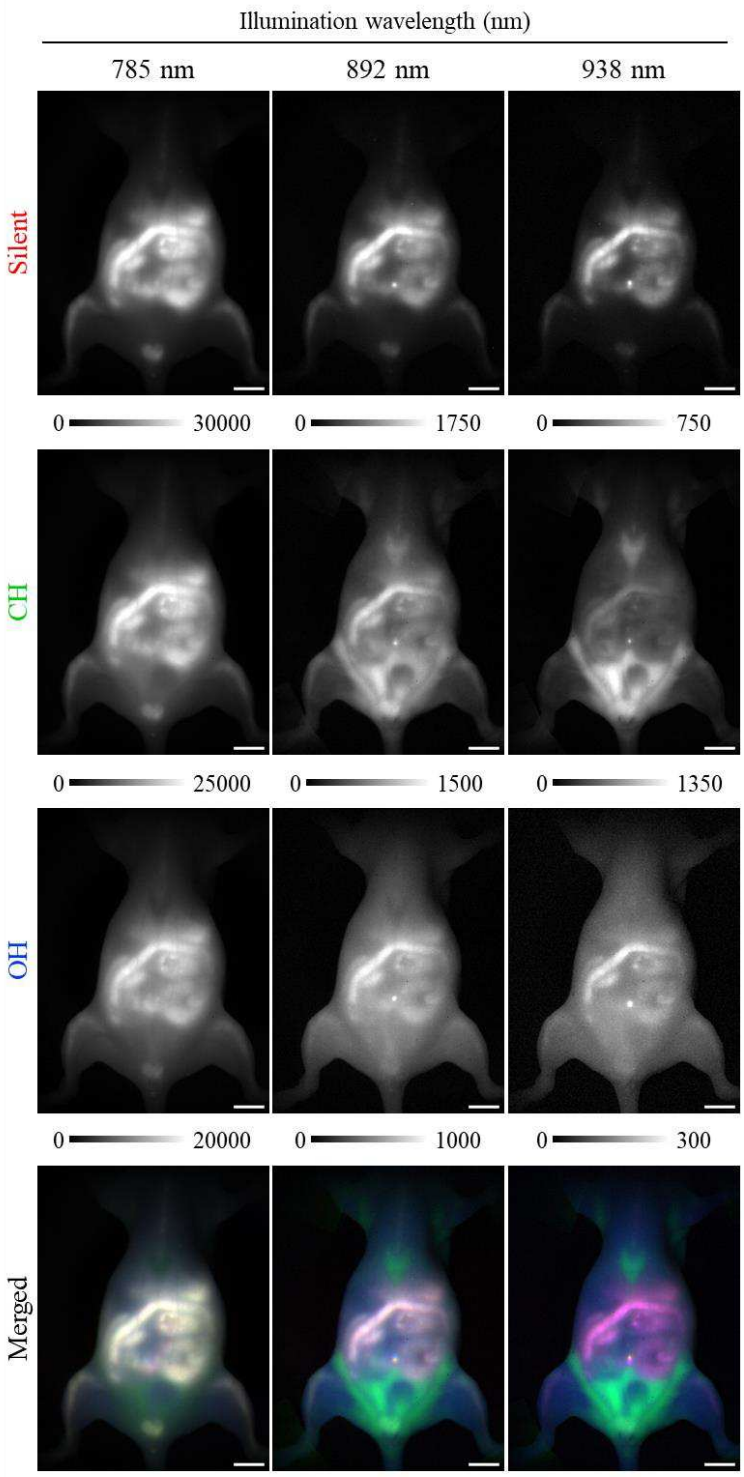


Fig. S 17. *In vivo* wide-field SWIR Raman images acquired from the same mice used for the spectral measurements in Fig. S 8 and Fig. S 16. Color bars values are given in counts/min. Images were acquired using System 2 in free-run mode. Imaging parameters: 785 nm (237 mW/cm²) illumination, 0.1 s per-frame exposure; band-pass filters: silent: BP975-25, CH: BP1012.5-25, OH: BP1062.5-25; 892 nm (233 mW/cm²) illumination, 1000 ms exposure; filters: silent: BP1150-25, CH: BP1200-25, OH: BP1262.5-25; 938 nm (289 mW/cm²) illumination, 2000 ms exposure; filters: silent: BP1200-25, CH: BP1287.5-25, OH: BP1362.5-25. Scale bars: 1 cm.

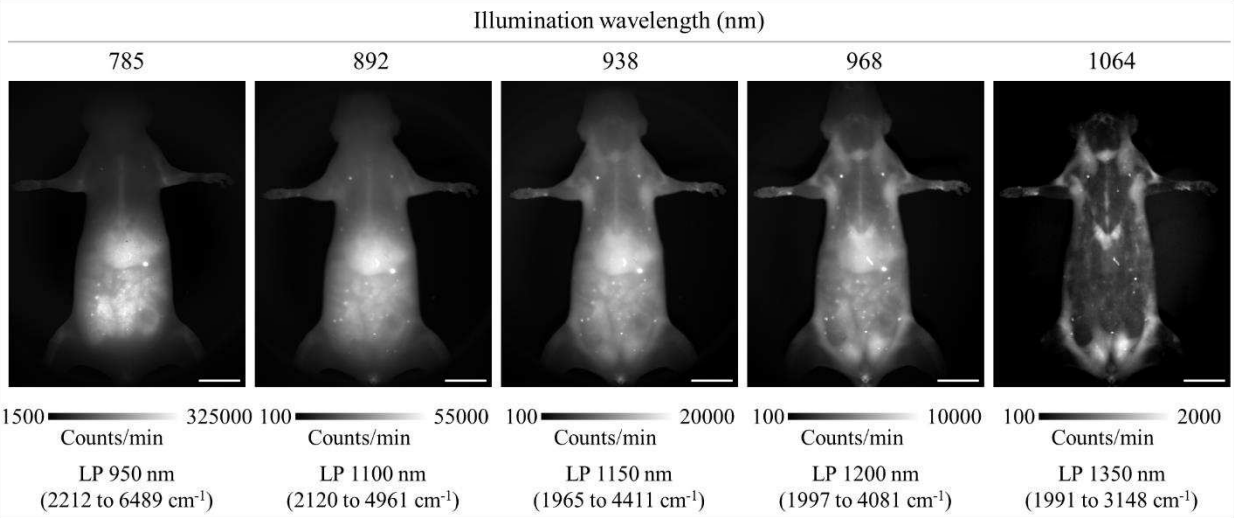


Fig. S 18. Images acquired using long-pass (LP) filters, after illumination at the same wavelengths as in Figure 2 a-b and Fig. S 9 (ventral view). These LP filters cover wavelengths comprising the incident wavelength + Raman shift corresponding to wavenumbers above 1965 cm^{-1} (the detection range, in wavenumbers, is shown in parenthesis, considering the detection limit of the camera as 1600 nm). As a consequence, these LP images detected the added signal from Raman-silent, CH and OH Raman bands for each illumination wavelength within a single frame. The OH band after illumination at 1064 nm lies beyond the detector's limit, so it does not contribute to the wide-band signal. The wavenumbers displayed here were rounded to the nearest integer**.** The same mouse used in Figure 2 a and Fig. S 14 was imaged. The data are representative of 2 mice. Images were acquired using System 1 in free-run mode. Imaging parameters: 785 nm (138 mW/cm²) illumination, 10 s per-frame exposure, filter: LP950; 892 nm (145 mW/cm²) illumination, 30 s exposure, filter: LP1100; 938 nm (153 mW/cm²) illumination, 30 s exposure, filter: LP1150; 968 nm (152 mW/cm²) illumination, 45 s exposure, filter: LP1200; 1064 nm (178 mW/cm²) illumination, 60 s exposure, filter: LP1350.Scale bars: 1 cm.

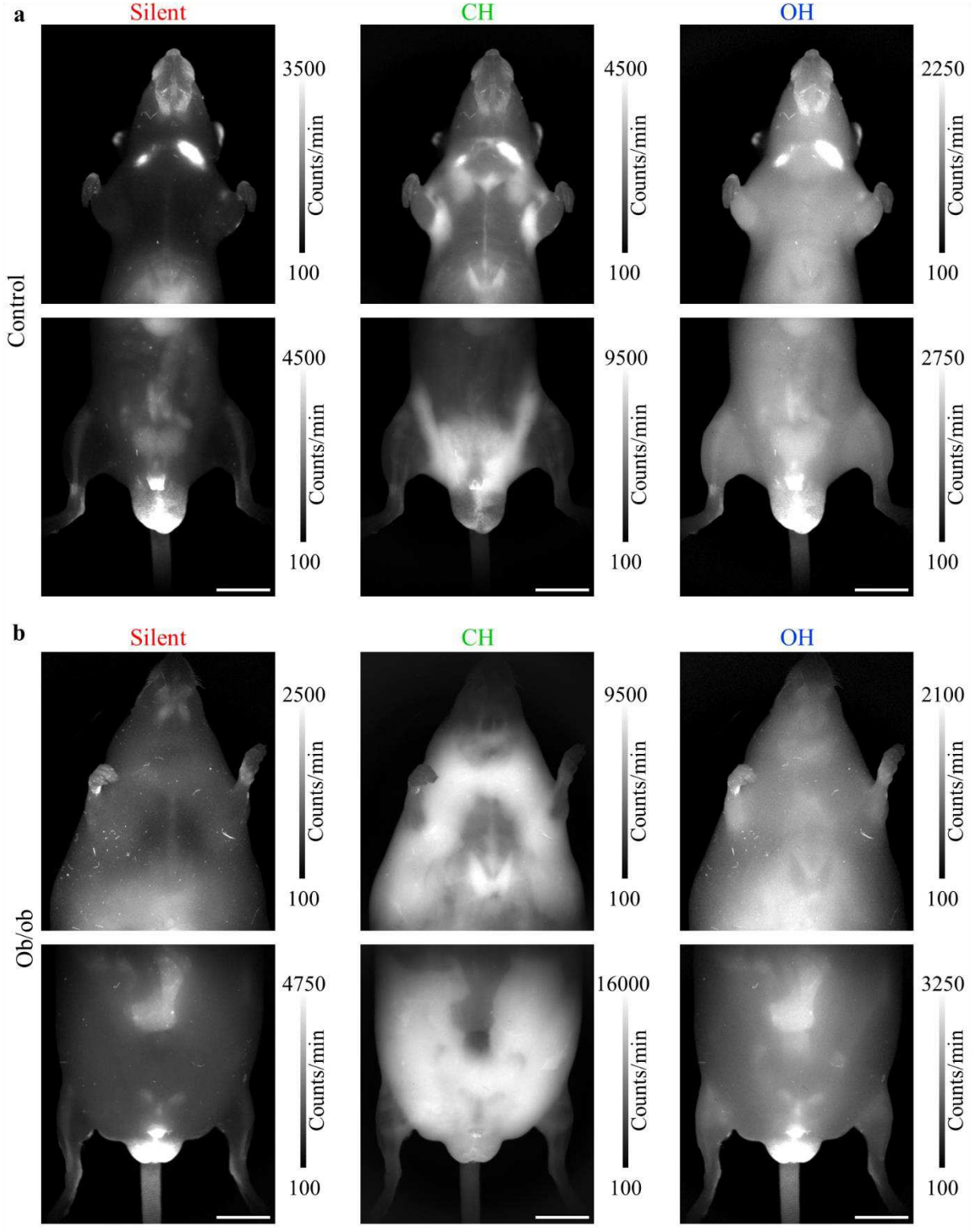


Fig. S 19. Single-band images of the mice shown in Figure 3 a. Representative of 2 mice per group. Note that these mice are from pigmented strains, and pigment-derived autofluorescence can introduce measurement artifacts (see Supplementary Note 4). Imaging parameters are listed in the caption of Figure 3 a. Scale bars: 1 cm.

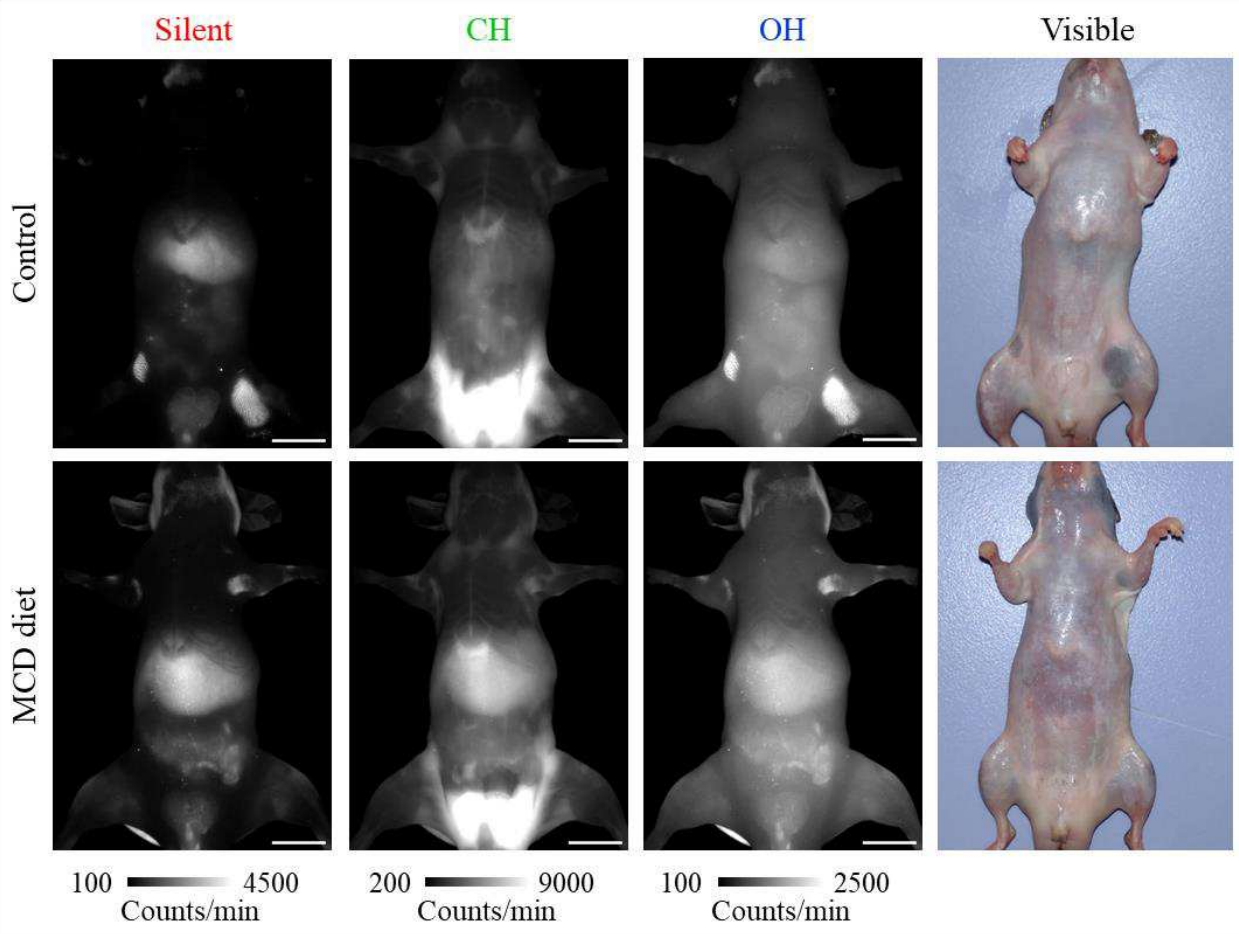


Fig. S 20. Single-band images of the mice in Figure 3 b-c (ventral view), along with visible images. The data are representative of 4 mice per group, and the other replicates are shown in Fig. S 21, while the region of interest (ROI) selected for liver CH Raman intensity measurements (Figure 3 d) are shown in Fig. S 22. Note that these mice are from a pigmented strain, and pigment-derived autofluorescence can introduce measurement artifacts (see Supplementary Note 4). Images were acquired using System 1 in free-run mode, with imaging parameters: 938 nm illumination (159 mW/cm²), 45 s per-frame exposure; band-pass (BP) filters: BP1200-25 (silent), BP1287.5-25 (CH), BP1350-25 (OH). Scale bars: 1 cm.

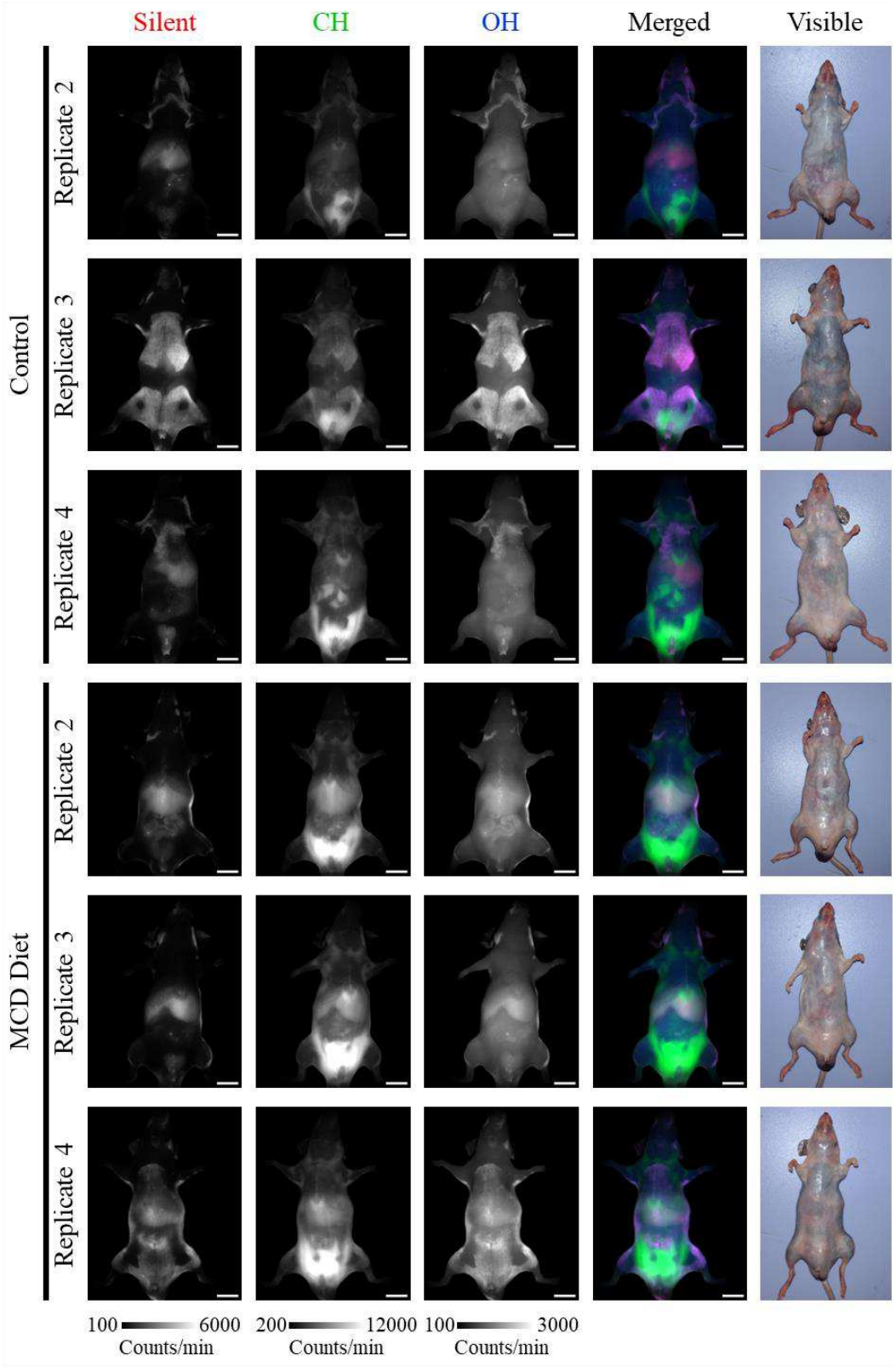


Fig. S 21. Single-band, merged, and visible images of biological replicates of mice under a diet deficient in methionine and choline (MCD) or on a normal diet (control), corresponding to the experiment shown in Figure 3 b-d and Fig. S 20. Autofluorescent patches observed in some animals are attributed to signal from pigmented skin (**Supplementary Note 4**). Images were

acquired using System 1 in free-run mode, with imaging parameters: 938 nm illumination (159 mW/cm²), 45 s per-frame exposure; band-pass (BP) filters: BP1200-25 (silent), BP1287.5-25 (CH), BP1350-25 (OH). Scale bars: 1 cm.

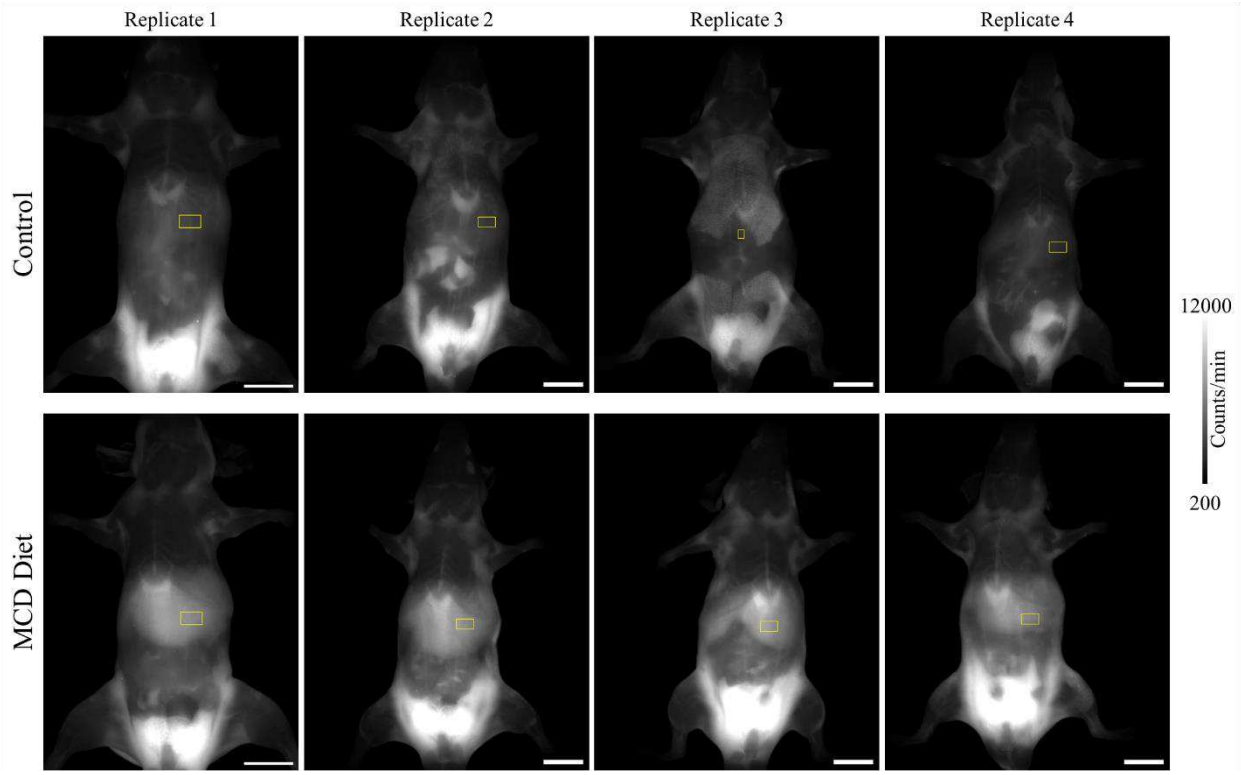


Fig. S 22. Regions of interest (ROIs, yellow rectangles) used for data extraction for Figure 3 d overlaid with the CH SWIR Raman images (ventral view) shown in Figure 3 b-c and Fig. S 21. Given the strong presence of pigmentation autofluorescence on the skin area covering the liver of replicate 3 (control), a small ROI was selected to avoid the interference of pigmentation onto the measured CH region intensity. To keep the ROI size consistent, similarly sized and positioned ROIs were selected for the other replicates. Scale bars: 1 cm.

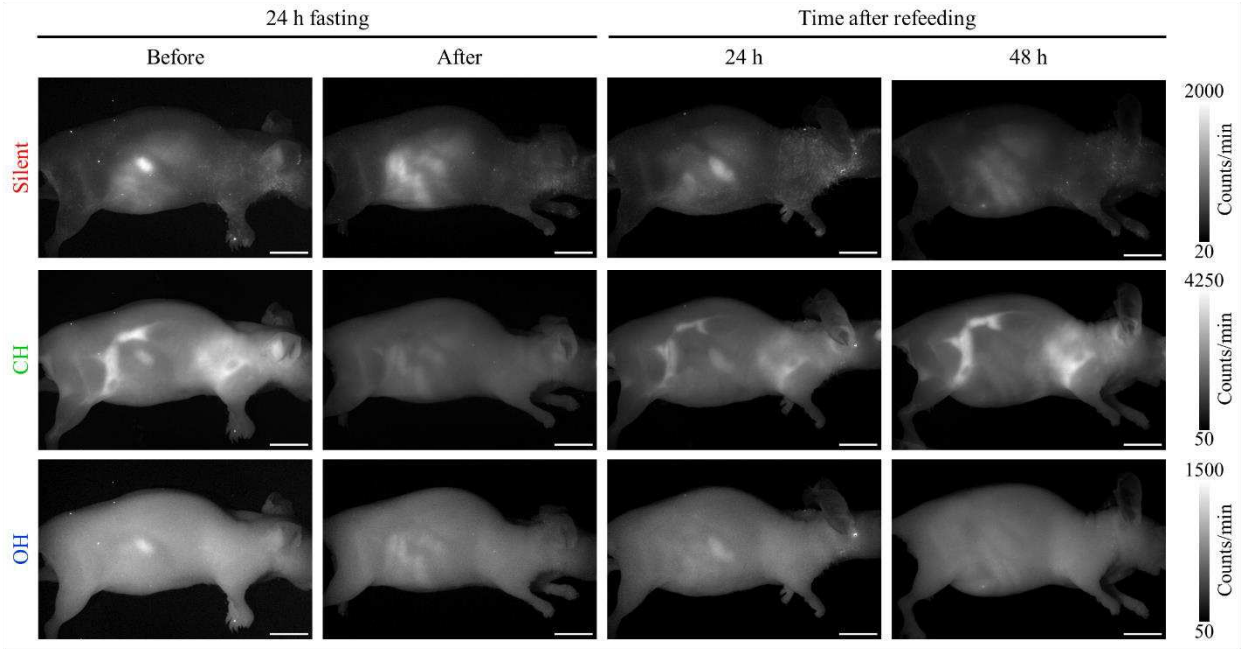


Fig. S 23. Single-band images (right lateral view) of the anesthetized mouse images shown in Figure 3 e. Images were acquired using System 1 in free-run mode, with imaging parameters: 938 nm illumination (143 mW/cm²), 30 s per-frame exposure; band-pass (BP) filters: BP1143.75-12.5 (silent), BP1287.5-25 (CH), BP1362.5-25 (OH). Scale bars: 1 cm.

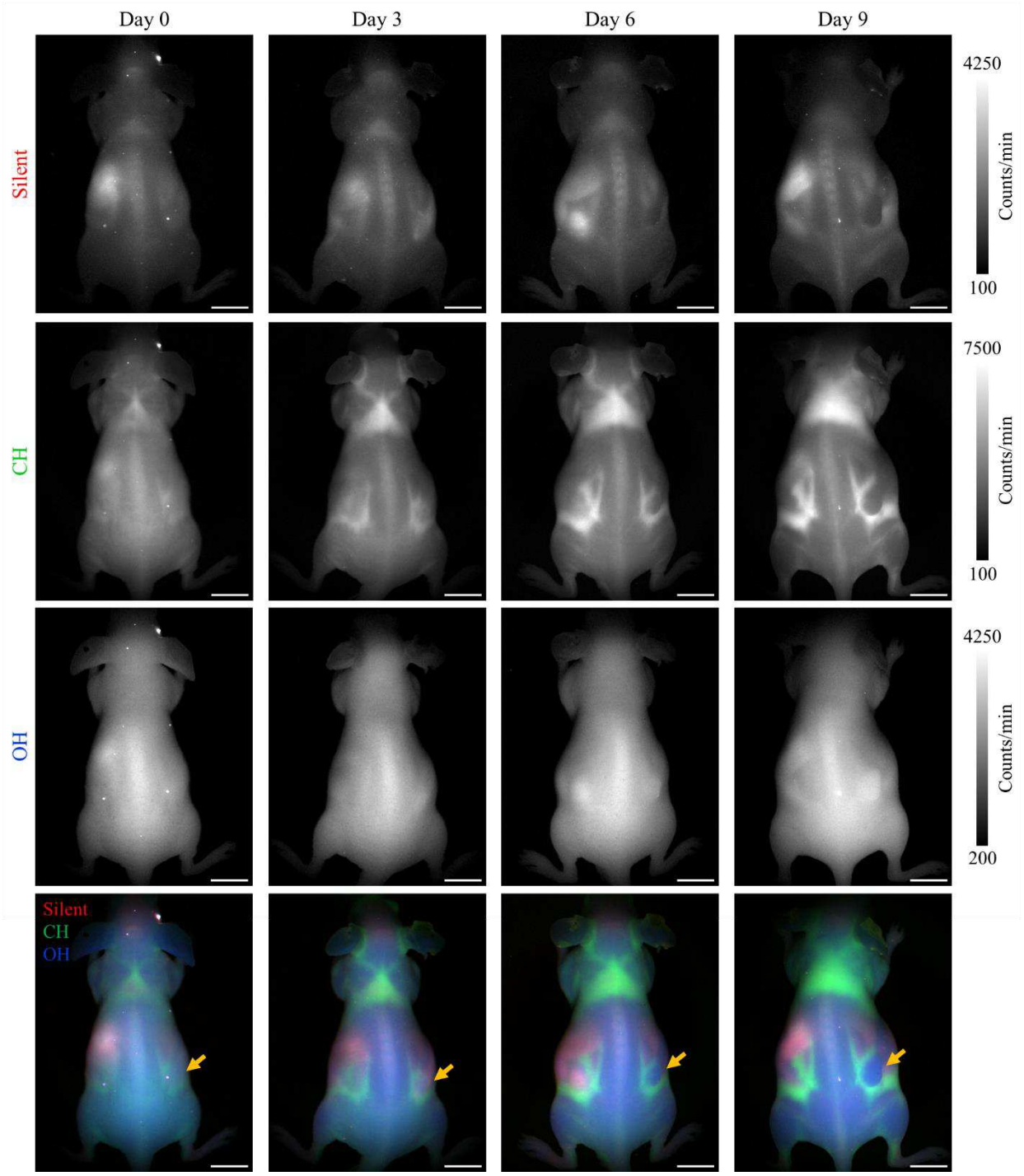


Fig. S 24. SWIR Raman imaging of anesthetized mice bearing subcutaneous xenografts of 4T1 breast cancer cells in the right flank. Animals were imaged at the indicated number of days relative to tumor cell implantation. The arrow indicates the growing tumor. Results are representative of four animals. Images were acquired using System 1 in free-run mode. Imaging parameters: 892 nm (124 mW/cm²) illumination, 10 s per-frame exposure; band-pass (BP) filters: BP1150-25 (silent), BP1200-25 (CH), BP1300-25 (OH). Scale bars: 1 cm.

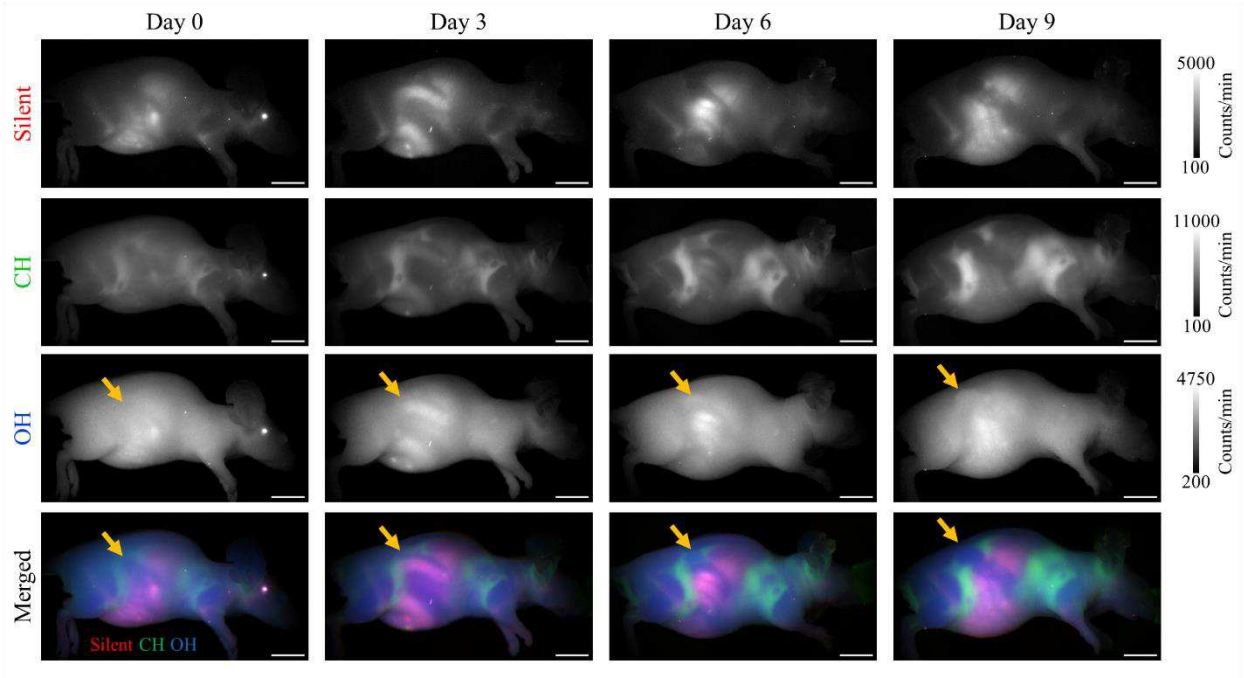


Fig. S 25. Right lateral view of the mouse shown in Fig. S 24. The arrow indicates the tumor location. Results are representative of four animals. Images were acquired using System 1 in free-run mode. Imaging parameters: 892 nm (124 mW/cm²) illumination, 10 s per-frame exposure; band-pass (BP) filters: BP1150-25 (silent), BP1200-25 (CH), BP1300-25 (OH). Scale bars: 1 cm.

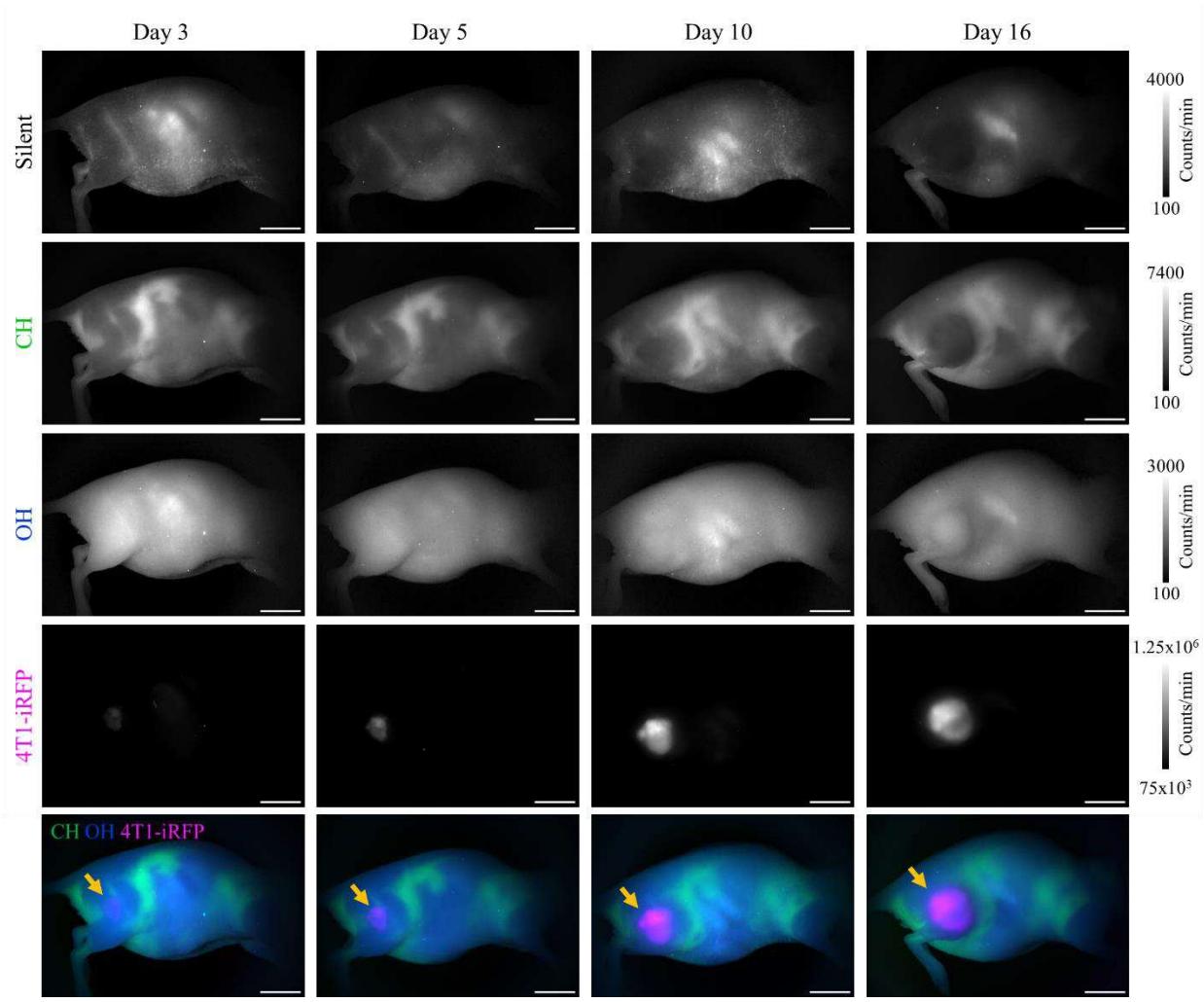


Fig. S 26. Combination of wide-field Raman imaging and fluorescence imaging of mice like those in Fig. S 25, except that the 4T1 tumor cells were expressing the fluorescent protein iRFP720 and were injected onto the right leg. Results are representative of two animals. Images were acquired using System 1 in free-run mode. Imaging parameters: 4T1-iRFP: 672 nm illumination (89 mW/cm² on Days 3 and 5; 92 mW/cm² on Days 10 and 16), 1 s per-frame exposure, long-pass (LP) filter: LP1100; SWIR Raman: 892 nm (106 mW/cm² on Days 3 and 5; 104 mW/cm² on Days 10 and 16) illumination, 20 s exposure; band-pass (BP) filters: BP1150-25 (silent), BP1200-25 (CH), BP1300-25 (OH). Scale bars: 1 cm.

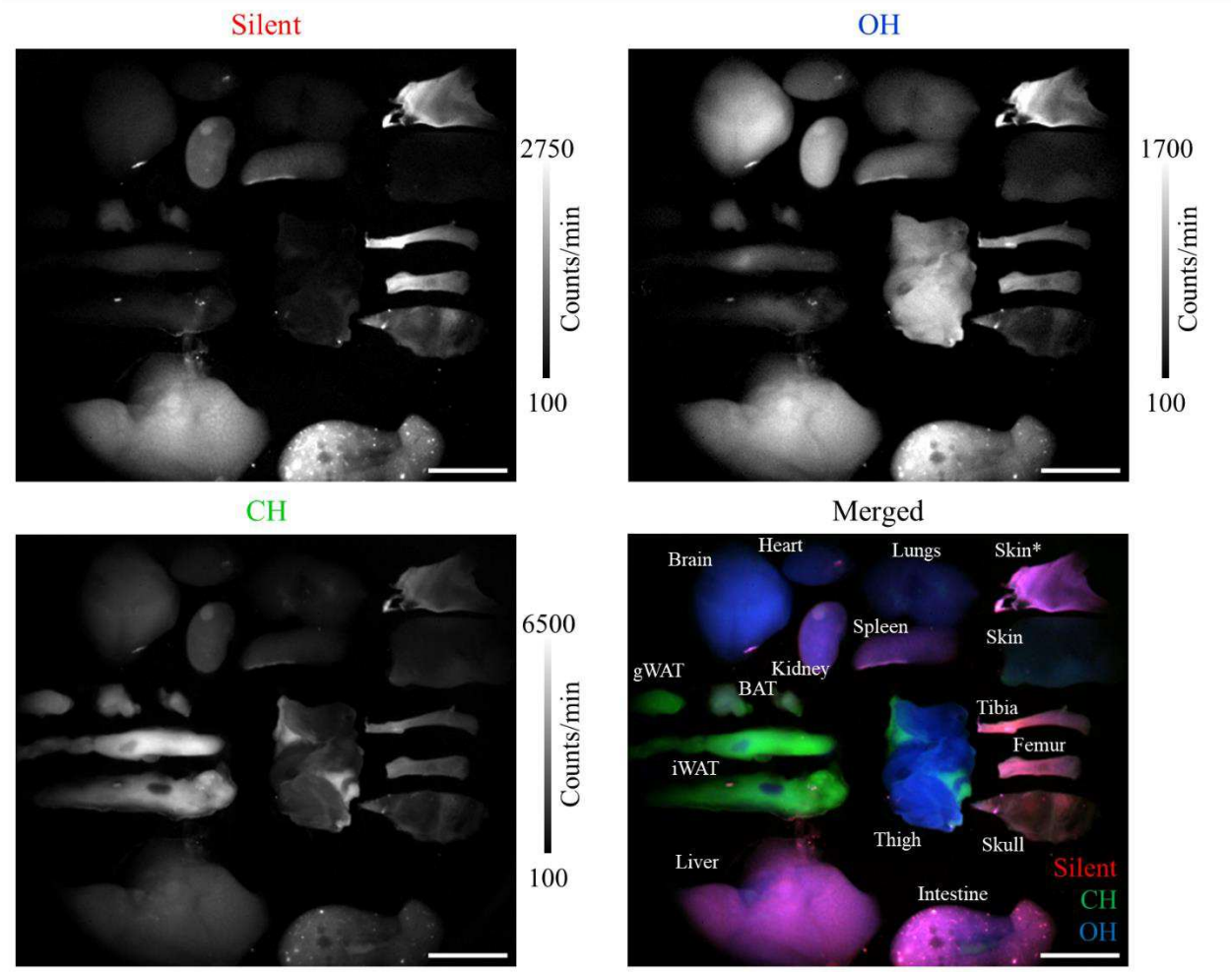


Fig. S 27. Wide-field SWIR Raman imaging of organs from a healthy C57BL/6J mouse upon 892 nm illumination. Legend: BAT, brown adipose tissue; gWAT, gonadal white adipose tissue; iWAT, inguinal white adipose tissue; skin*, skin with melanin patch. The data are representative of 2 mice. Images were acquired using System 1 in free-run mode. Imaging parameters: 892 nm (172 mW/cm²) illumination, 30 s per-frame exposure; band-pass (BP) filters: BP1150-25 (silent), BP1200-25 (CH), BP1300-25 (OH). Scale bars: 1 cm.

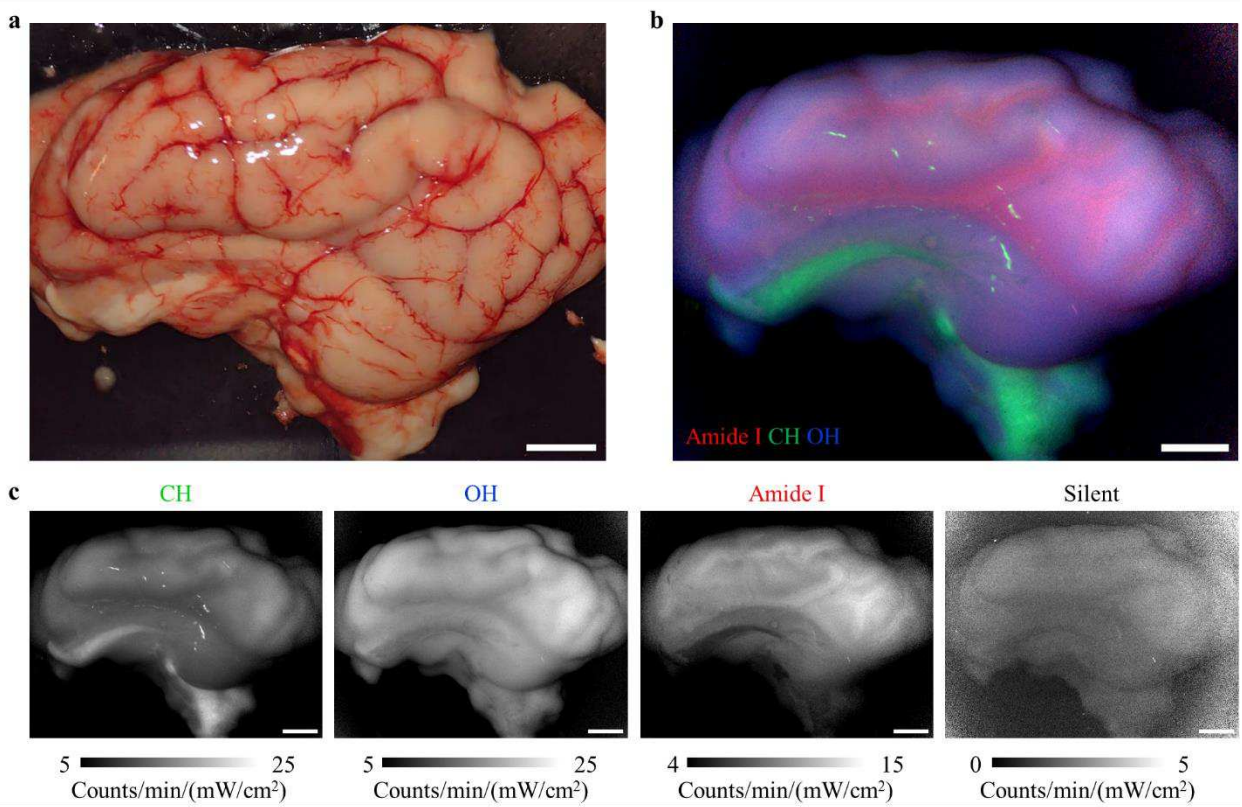


Fig. S 28. Porcine brain outer cortex (lateral view of the left hemisphere) imaged **(a)** in the visible and **(b-c)** using SWIR Raman imaging. Images were acquired using System 1 in free-run mode. Imaging parameters: 938 nm (115 mW/cm²) illumination, 30 s per-frame exposure; band-pass (BP) filters: BP1112.5-25 (Amide I), BP1200-25 (silent), BP1287.5-25 (CH), BP1350-50 (OH). Scale bars: 1 cm.

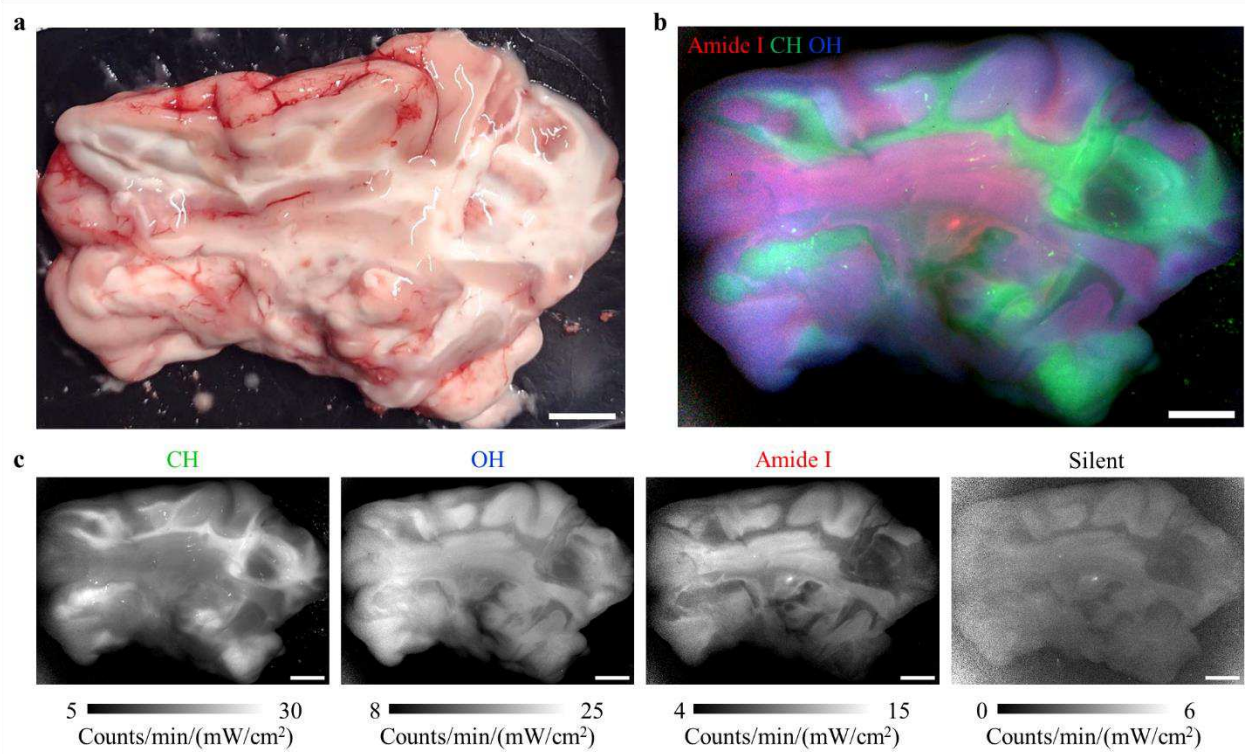


Fig. S 29. Longitudinal section of the porcine left hemisphere (lateral view) showed in Fig. S 28, imaged **(a)** in the visible and **(b-c)** using SWIR Raman imaging. Images were acquired using System 1 in free-run mode. Imaging parameters: 938 nm (115 mW/cm²) illumination, 30 s per-frame exposure; band-pass (BP) filters: BP1112.5-25 (Amide I), BP1200-25 (silent), BP1287.5-25 (CH), BP1350-50 (OH). Scale bars: 1 cm.

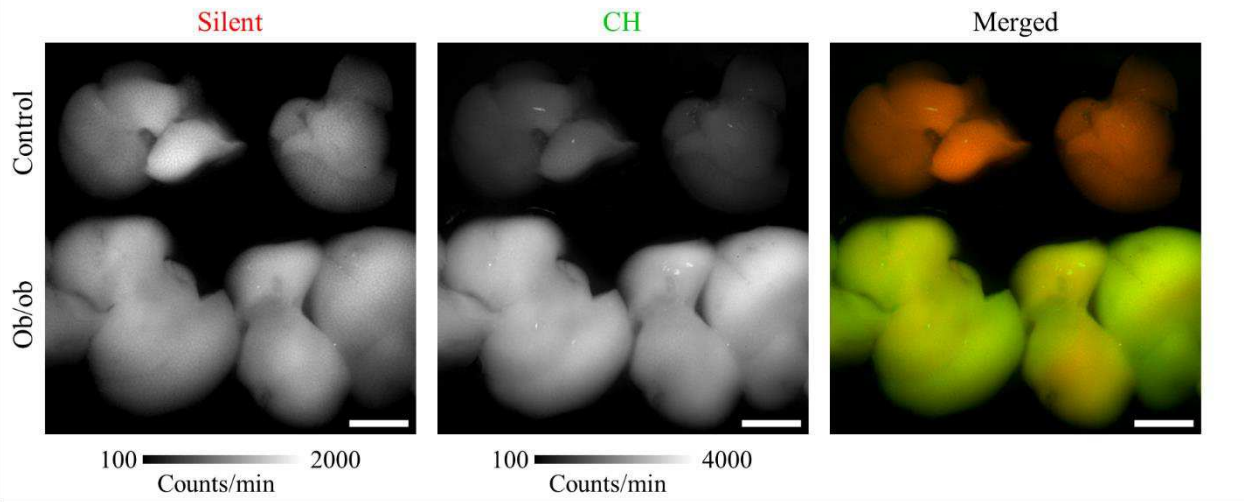


Fig. S 30. Wide-field Raman imaging of livers excised from genetically obese mice (Ob/Ob) and lean C57BL/6J mice (Control). Two whole livers per group are shown. Images were acquired using System 1 in free-run mode. Imaging parameters: 938 nm (96 mW/cm²) illumination, 60 s per-frame exposure; band-pass (BP) filters: BP1143.75-12.5 (silent), BP1287.5-25 (CH). Scale bars: 1 cm.

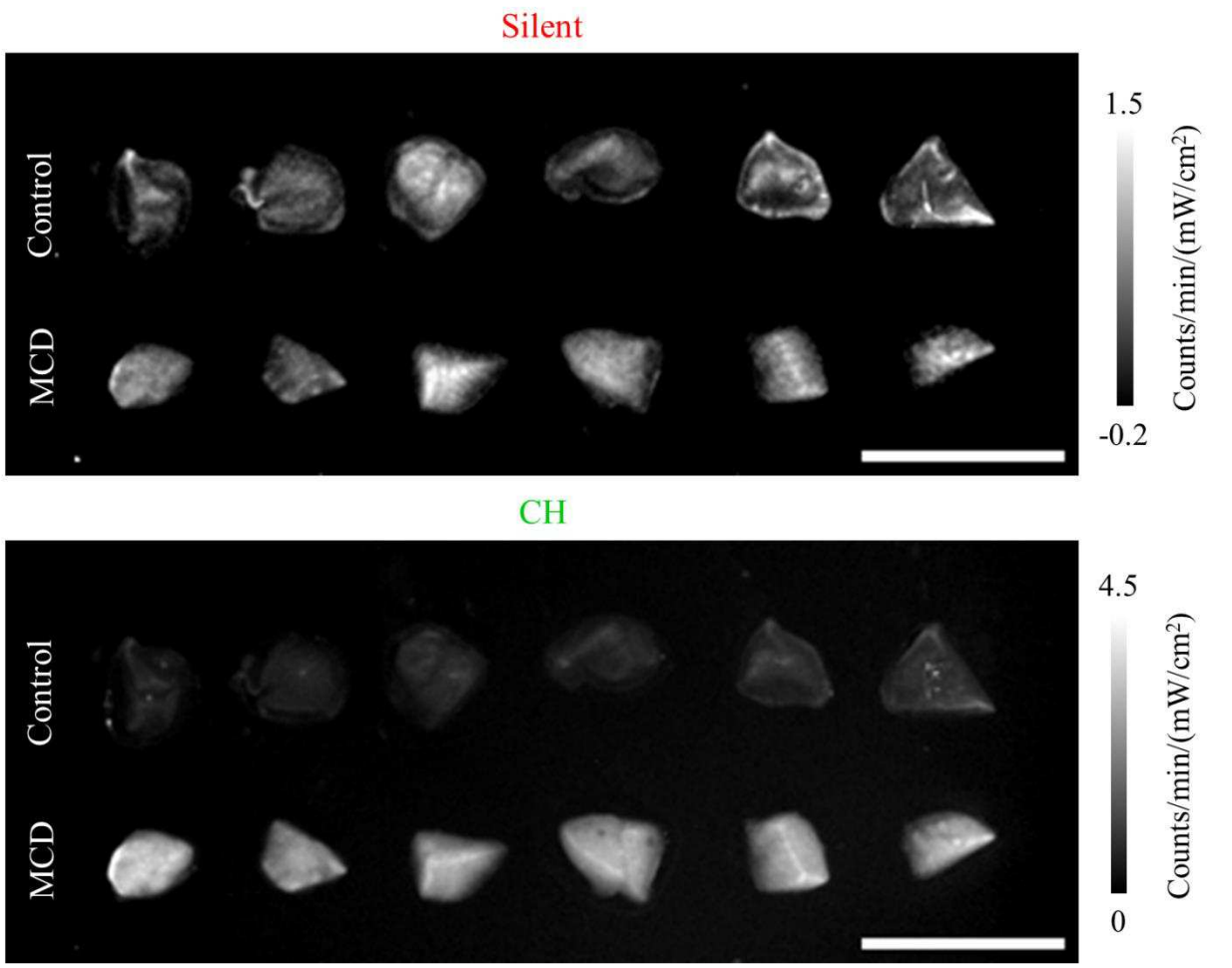


Fig. S 31. Single-band images of the unfixed dissected livers pieces shown in Figure 4 a. Samples from six mice per group are shown. MCD, methionine-choline diet. Images were acquired using System 1 in free-run mode. Imaging parameters: 1064 nm (115 mW/cm²) illumination, 600 s per-frame exposure; band-pass (BP) filters: BP1337.5-25 (silent), BP1550-50 (CH). Scale bars: 1 cm.

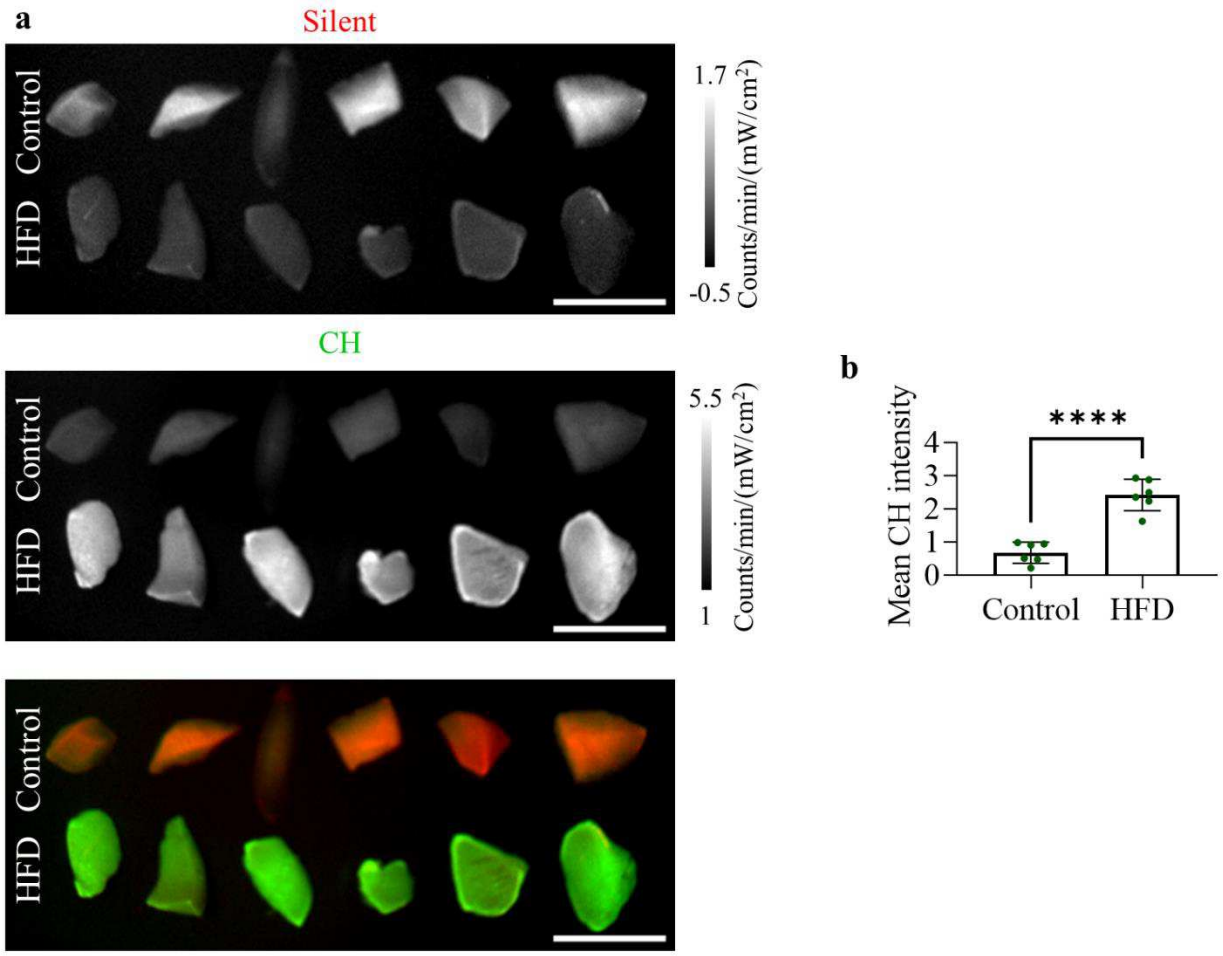


Fig. S 32. Liver samples from mice induced either to a high fat diet (HFD) for 12 weeks or to a control diet (n = 6 per group). **a)** Samples illuminated at 1064 nm and imaged in the silent (red) and CH (green) Raman regions. **b)** Quantification of mean CH Raman intensity based on the imaging [counts/min/(mW/cm2)]. Differences between the groups were statistically analyzed using an unpaired, two-tailed t test. **** indicates P-value < 0.0001. Images were acquired using System 1 in free-run mode. Imaging parameters: 1064 nm (115 mW/cm²) illumination, 600 s per-frame exposure; band-pass (BP) filters: BP1337.5-25 (silent), BP1550-50 (CH). Scale bars: 1 cm.

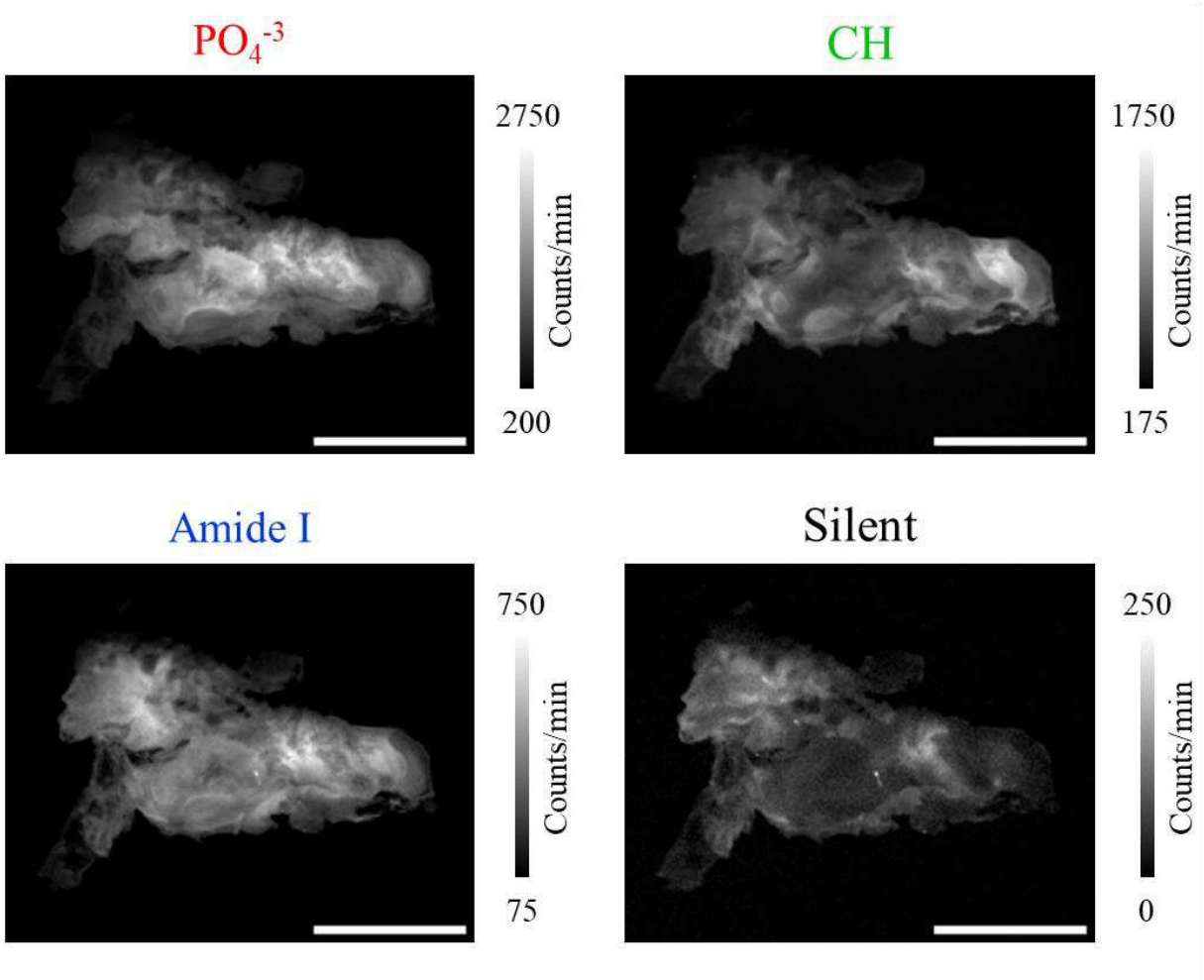


Fig. S 33. Single-band images of the atherosclerotic plaque shown in Figure 4 e, with the addition of an image of the silent region. Images were acquired using System 1 in free-run mode. Imaging parameters: 1064 nm illumination (177 mW/cm²), 300 s per-frame exposure; band-pass (BP) filters: BP1187.5-25 (PO_4^{-3}), BP1287.5-25 (Amide I), BP1337.5-25 (silent), and BP1550-50 (CH). Scale bars: 1 cm.

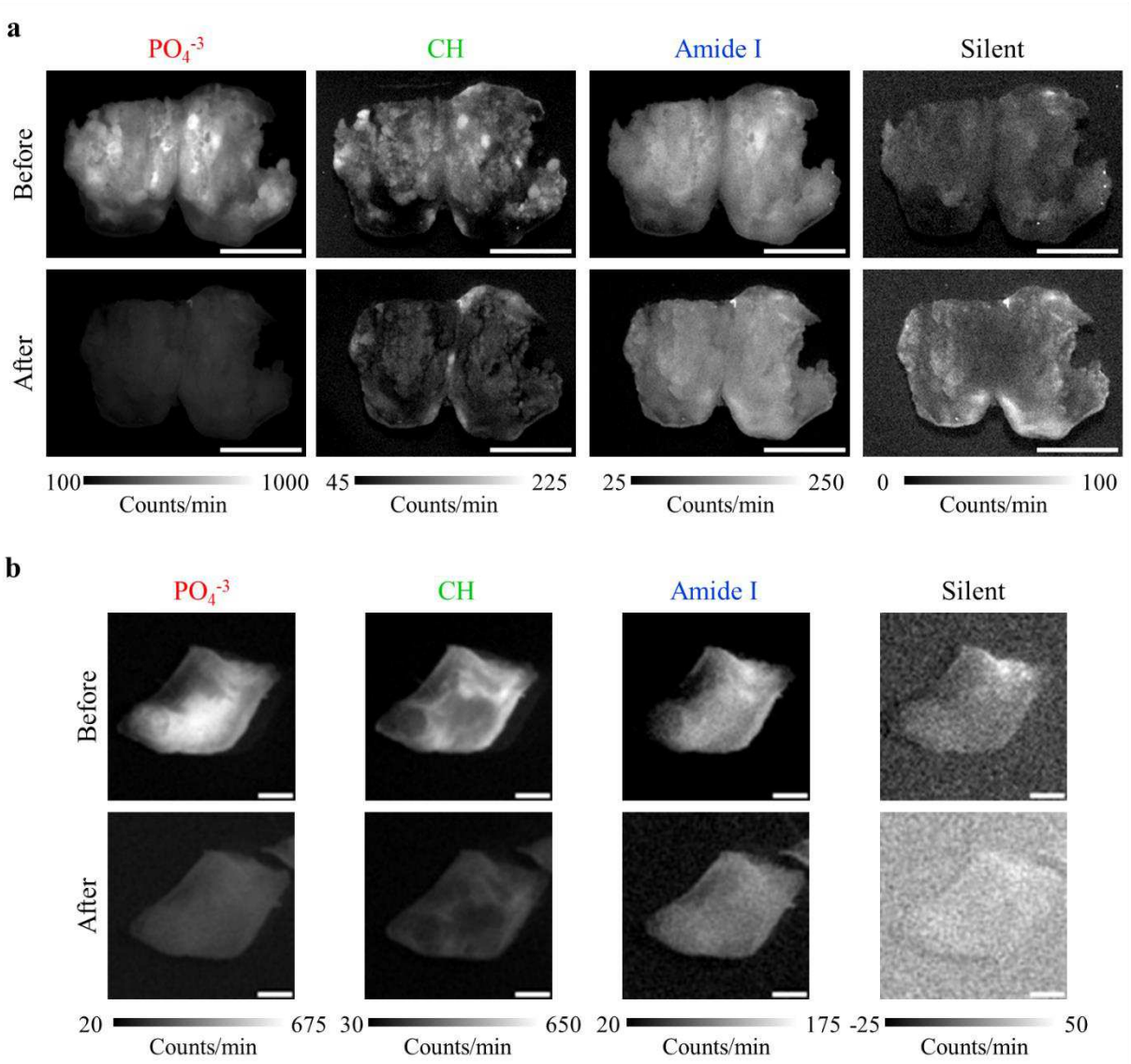


Fig. S 34. Single-band images of the atherosclerotic plaques in (**a**) Figure 4 f (femoral artery) and (**b**) in Figure 4 g (carotid artery), with the addition of an image of the silent region. Scale bars: **(a)** 1 cm, **(b)** 0.2 cm. Images were acquired using System 1 in free-run mode. Imaging parameters: 1064 nm illumination (163 mW/cm²), 300 s per-frame exposure; band-pass (BP) filters: BP1187.5-25 (PO_4^{-3}), BP1287.5-25 (Amide I), BP1337.5-25 (silent), and BP1550-50 (CH).

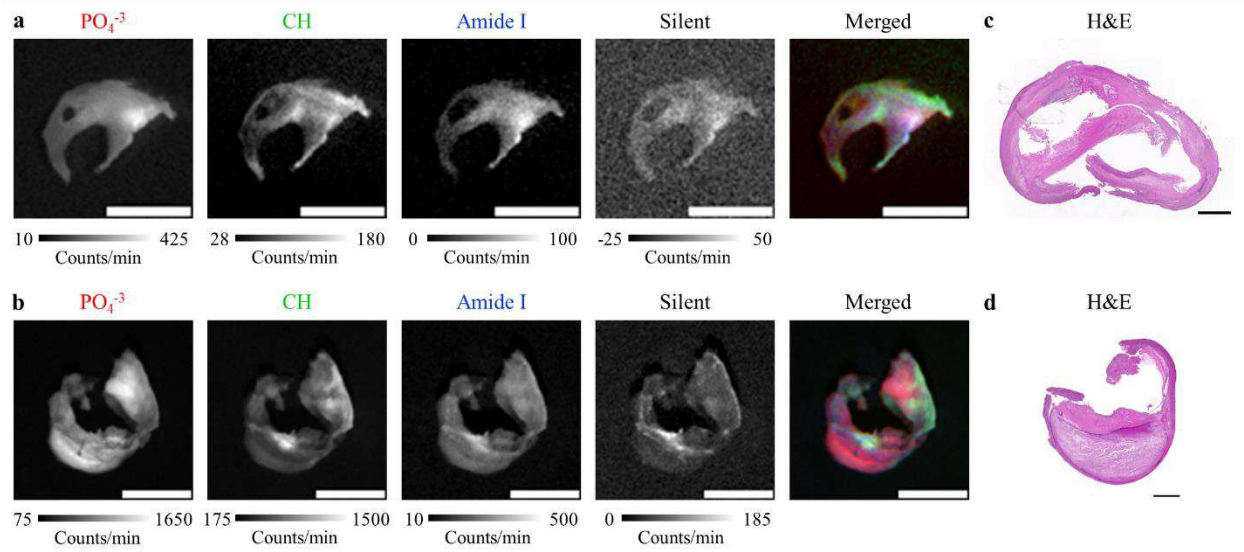


Fig. S 35. **a-b)** Biopsied human atherosclerotic plaques from carotid arteries illuminated at 1064 nm and imaged in the PO_4^{-3} (red), CH (green), and Amide I (blue) Raman bands. The silent region is also shown individually, but not in the merged image. **c-d**) Histological section stained with hematoxylin and eosin (H&E) adjacent to the unfixed samples shown in panels **(a)-(b)**. Images were acquired using System 1 in free-run mode. Imaging parameters: 1064 nm illumination (163 mW/cm² for panel (a); 176 mW/cm² for panel (b)), 300 s per-frame exposure; band-pass (BP) filters (BP): BP1187.5-25 (PO4-3), BP1287.5-25 (Amide I), BP1362.5-25 (silent), and BP1550-50 (CH).Scale bars: **(a)-(b)** 0.5 cm, **(c)-(d)** 0.1 cm.

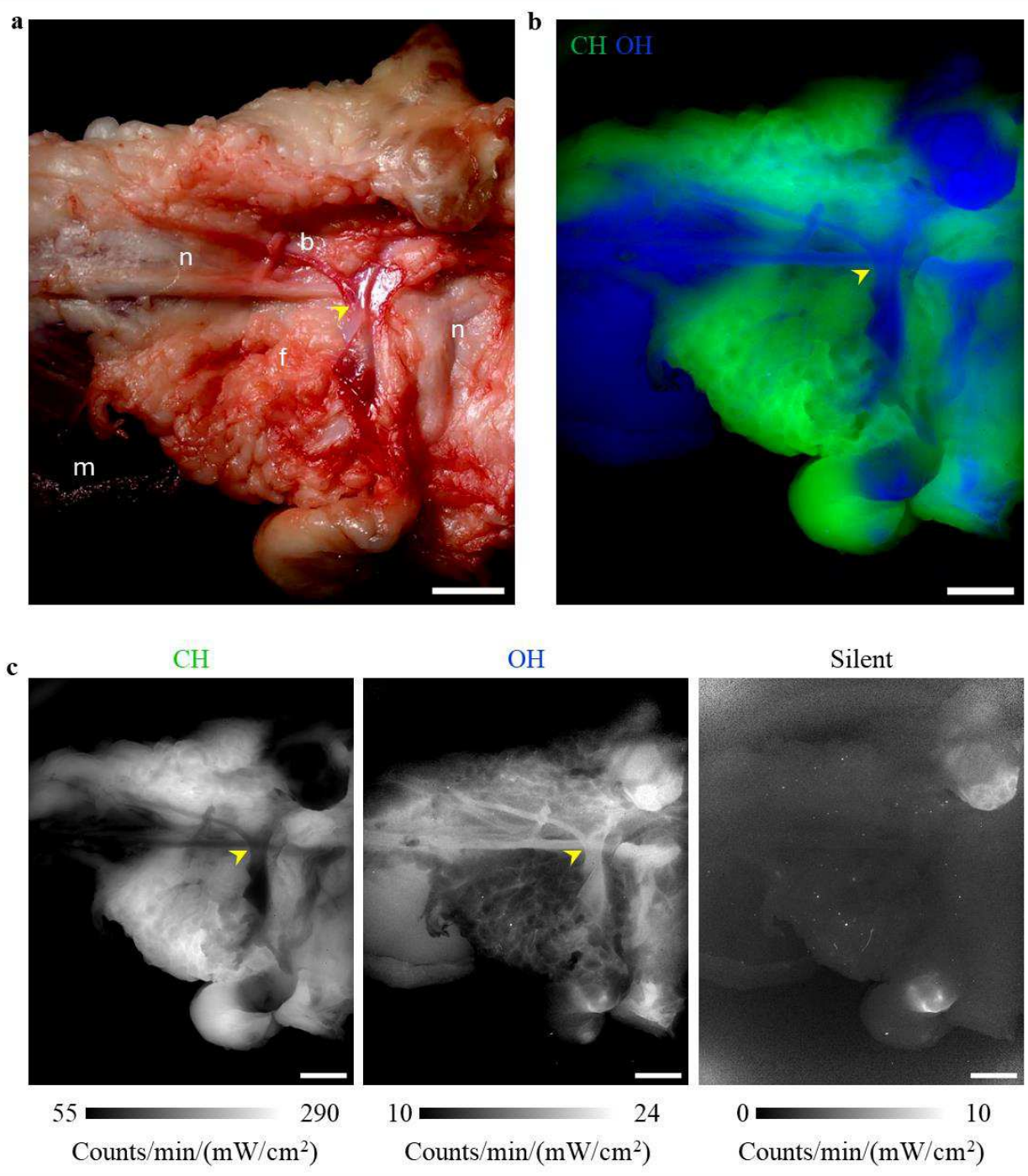


Fig. S 36. Nerve identification in fatty tissue of a porcine surgical model using SWIR Raman imaging. **a-c)** A porcine facial nerve was exposed, and imaged (a) in the visible and (b-c) using SWIR Raman imaging. The contrast of facial nerve to fatty tissue was obtained using the OH 5(blue) and CH (green) Raman imaging regions, revealing hidden parts of the nerve (yellow arrow head). The displayed contrast was optimized separately for each scattering band. Images were acquired using System 1 in free-run mode. Imaging parameters: 938 nm (115 mW/cm²) illumination, 60 s per-frame exposure; band-pass (BP) filters: BP1200-25 (silent), BP1287.5-25 (CH), and BP1350-50 (OH). Legend: facial nerve (n), blood vessel (b), muscle (m), fatty tissue (f). Scale bars: 1 cm.

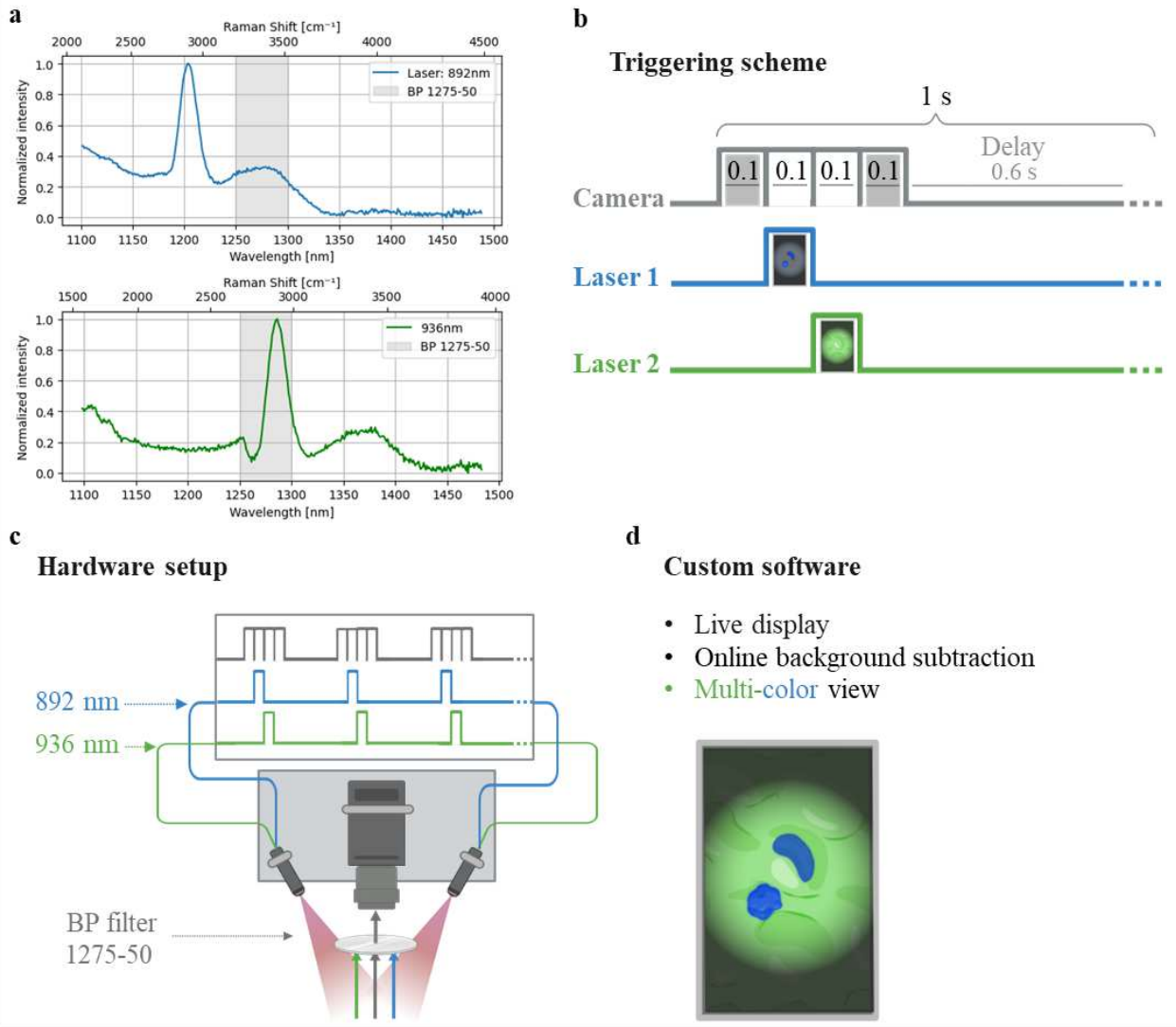


Fig. S 37. Real-time wide-field SWIR Raman imaging system. **a)** Spectral basis for single-window dual-band acquisition scheme. Emission spectra acquired from skin overlying a subcutaneous fat pad *in vivo* (same anatomical region A from Fig. S 7). The lower x-axis indicates detected wavelength, and the upper x-axis shows the corresponding Raman shift for each illumination wavelength. The shaded region denotes the transmission window of the BP1275-50 bandpass filter. Under 892 nm excitation, the OH Raman band (3210-3518 cm^{-1}) shifts into the detection window (top). Under 936 nm, the CH band shifts into the same detection window, capturing the spectral range between 2684 and 2991 cm^{-1} (bottom). **b)** Acquisition triggering scheme. Each 1000 ms cycle consists of a 100 ms laser-off background exposure, two sequential 100 ms sample exposures (one per laser wavelength), a second 100 ms laser-off background exposure, and a 600 ms laser-off delay to maintain average irradiance within safety limits. The cycle repeats continuously throughout imaging. **c)** Hardware schematic. Two laser units illuminate the sample simultaneously at either 892 nm or 936 nm, implementing the spectral acquisition strategy shown in panel (a). Scattered light is filtered by a BP1275-50 bandpass filter and detected with a compact InGaAs camera. **d)** Real-time image-processing pipeline. Background subtraction is performed independently for each channel, after which CH-band and OH-band images are rendered as a live multicolor composite and displayed ~1 fps.

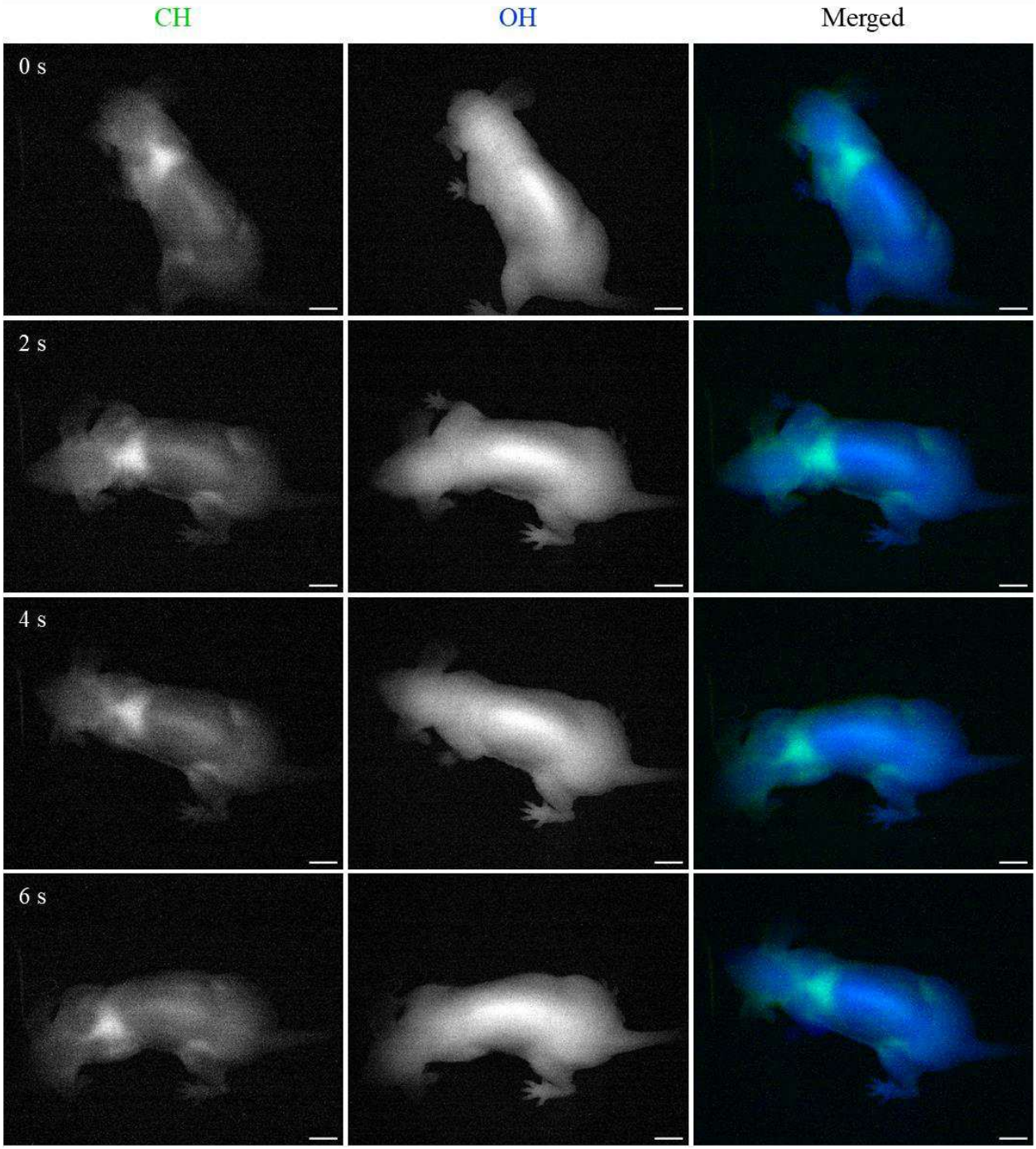


Fig. S 38. SWIR Raman imaging of an awake, freely moving mouse. CH-band (green), OH-band (blue), and merged frames are shown at 0, 2, 4, and 6 s. Despite the rapid and unpredictable motion of the animal, consistent CH- and OH-band contrast is maintained: the dorsal fat pads are highlighted in the CH channel, while the OH channel reflects the body-wide aqueous tissue background. Minor intra-frame motion artifacts are visible but do not prevent anatomical interpretation. Images were acquired using System 2 in triggered mode (10% duty cycle, 0.1 s exposure per channel); single band-pass filter: BP1275-50. Illumination parameters: 892 nm, 514 mW/cm² peak (51.4 mW/cm² time-averaged); 936 nm, 190 mW/cm² peak (19.0 mW/cm² time-averaged). All CH-band images are displayed over a range of 0-315 counts, while all OH-band images are displayed over a range of 0-415 counts. Scale bars: 1 cm.

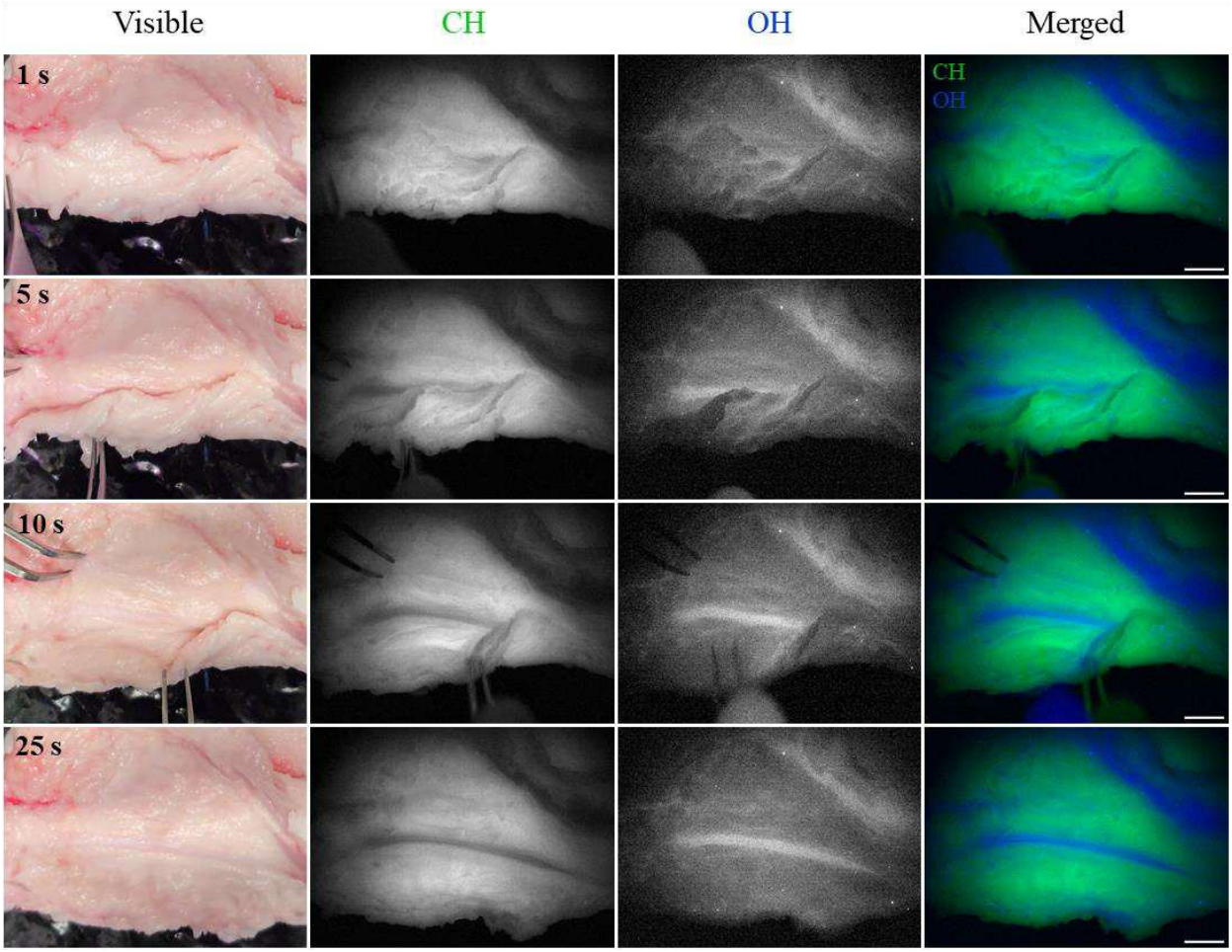


Fig. S 39. Real-time SWIR Raman imaging of a porcine facial nerve during progressive fat removal. Visible light, CH-band, OH-band, and merged frames are shown at 1, 5, 10, and 25 s of dissection. At early timepoints, the field is dominated by adipose tissue, appearing CH-high and OH-low in the merged image. As fat is incrementally removed and the nerve is exposed, OH-band signal progressively emerges along the nerve trajectory while local CH-band signal diminishes, providing continuous real-time feedback on tissue composition as layers are removed. Images were acquired using System 2 in triggered mode (10% duty cycle, 0.1 s exposure per channel); single band-pass filter: BP1275-50. Illumination parameters: 892 nm, 755 mW/cm² peak (75.5 mW/cm² time-averaged); 936 nm, 559 mW/cm² peak (55.9 mW/cm² time-averaged). All CH-band images are displayed over a range of 0-1430 counts, while all OH-band images are displayed over a range of 0-375 counts. Scale bars: 1 cm.

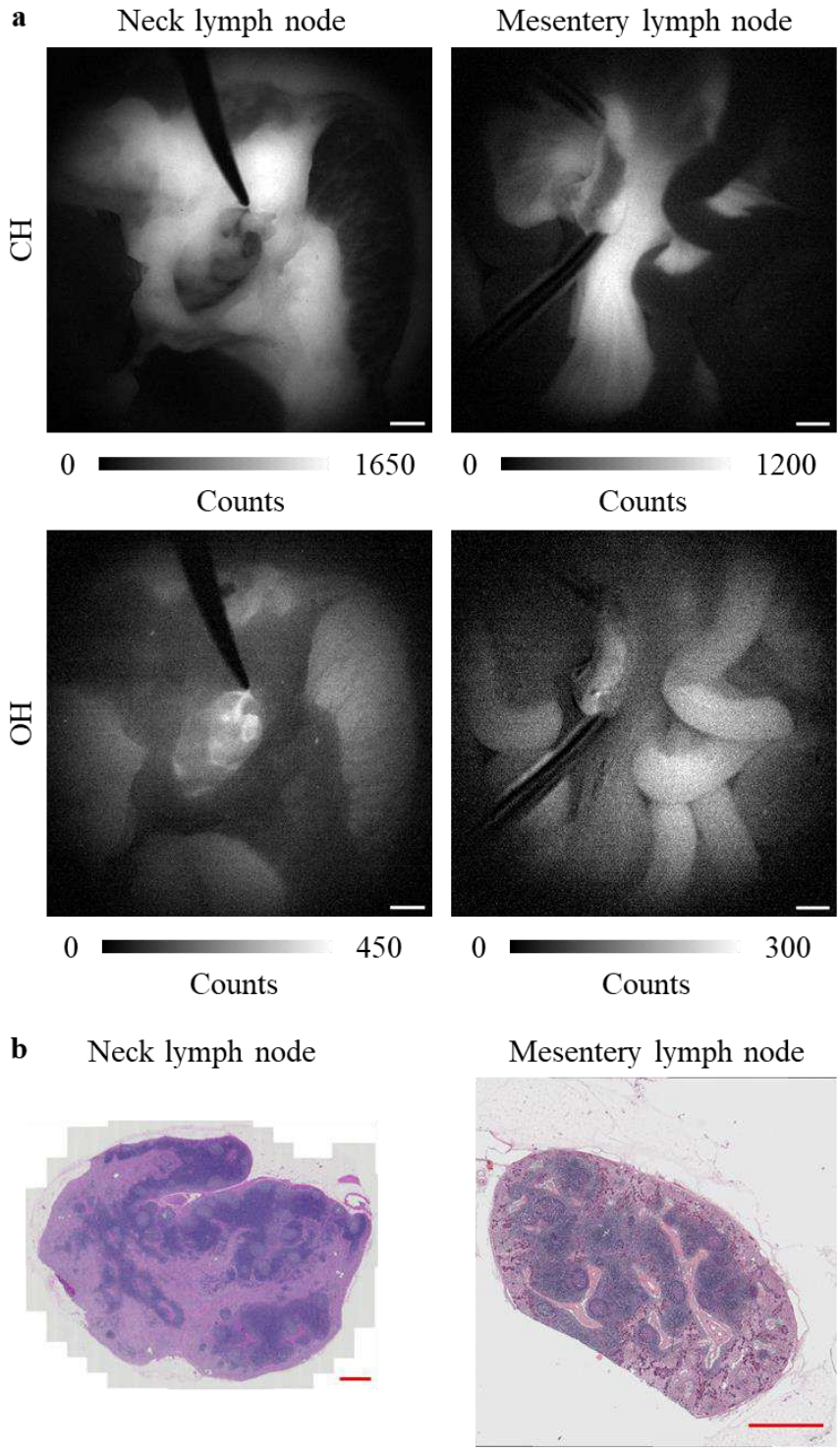


Fig. S 40. a) Single-band images of the porcine surgical model demonstration shown in Figure 5 c-d. All images were acquired with an exposure time of 0.1 s per frame using a BP1275-50 band-pass filter to define the detection window. CH-band images were acquired under 936 nm illumination and OH-band images under 892 nm illumination. Images were acquired using System 2 in triggered mode with the imaging parameters listed in the caption of Figure 5 c-d **b)** Histological assessment of the resected lymph nodes using hematoxylin and eosin (H&E) staining confirmed tissue identity. Scale bars: (a) 1 cm; (b) 0.1 cm.

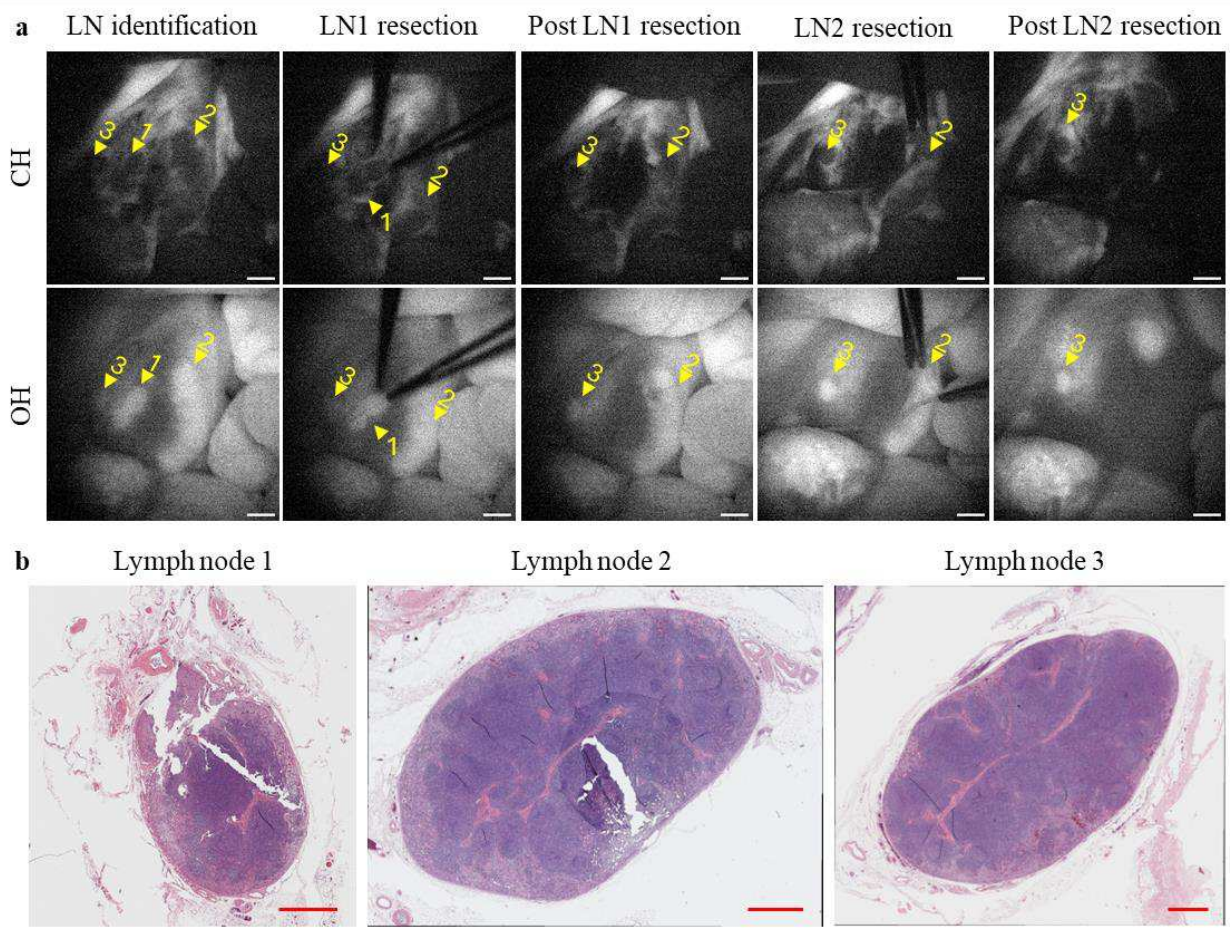


Fig. S 41. a) Single-band images of the surgery demonstration on a living pig shown in Figure 5 e. SWIR Raman contrast enables visualization of lymph nodes that are difficult to discern under white-light illumination and provides continuous guidance throughout dissection and resection. Images were acquired using System 2 in triggered mode (10% duty cycle, 0.1 s exposure per channel); single band-pass filter: BP1275-50. Illumination parameters: OH: 892 nm, 700 mW/cm² peak (70 mW/cm² time-averaged); CH: 936 nm, 465 mW/cm² peak (46.5 mW/cm² time-averaged). All Raman images are displayed over a range of 0-350 counts. **b)** Histological assessment of the resected lymph nodes using hematoxylin and eosin (H&E) staining confirmed tissue identity. Scale bars: (a) 1 cm; (b) 0.1 cm.

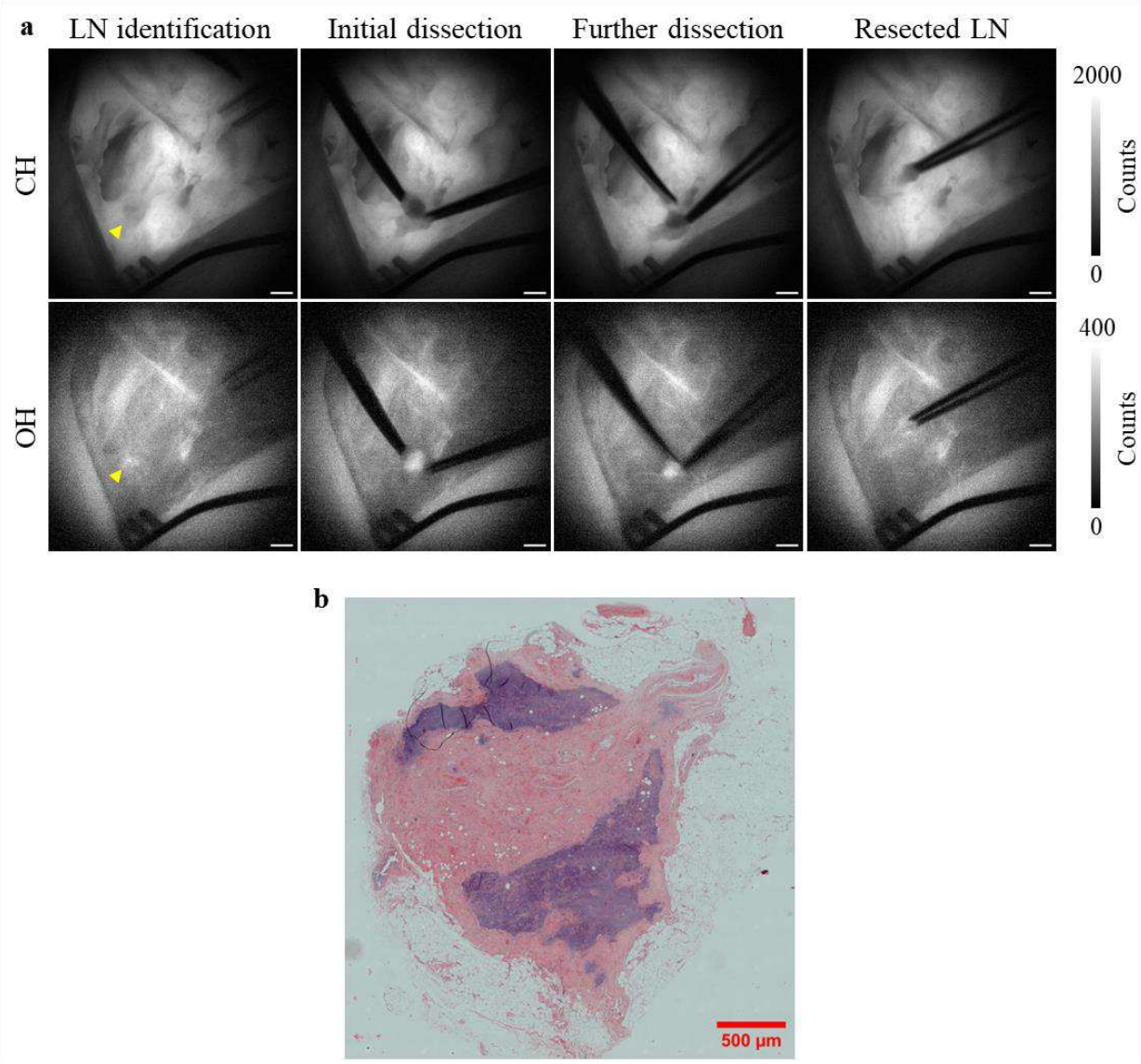


Fig. S 42. a) Single-band images of the human body donor lymph node resection frames shown in Figure 6. b). **b)** Histological assessment of the resected lymph node using hematoxylin and eosin (H&E) staining confirmed tissue identity. Images were acquired using System 2 in triggered mode (15% duty cycle, 0.15 s exposure per channel); single band-pass filter: BP1275-50. Imaging parameters: OH: 892 nm, 524 mW/cm² peak (78.6 mW/cm² time-averaged); CH: 936 nm, 384 mW/cm² peak (57.6 mW/cm² time-averaged). Scale bar**s**: (a) 1 cm; (b) 500 µm.

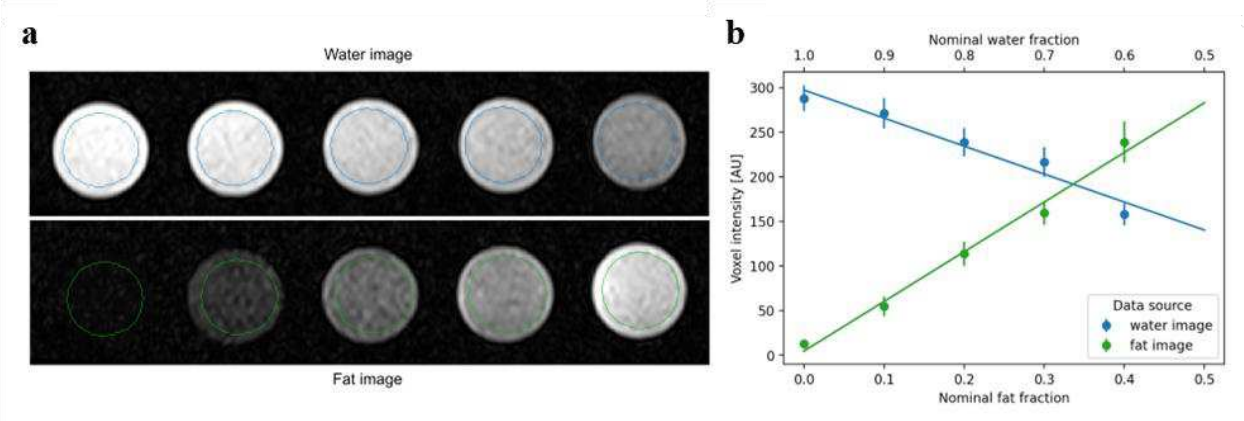


Fig. S 43. Dixon MRI intensity calibration. **a)** Water and fat images taken from a segmented phantom representing five mixtures of agarose and peanut oil. Contrast has been adjusted to an intensity range of 0 - 300 units. Regions of interest from which voxel intensities were extracted are shown as thin colored outlines. **b)** Water and fat image intensities (mean ± SD) plotted against their nominal concentrations alongside linear approximations.

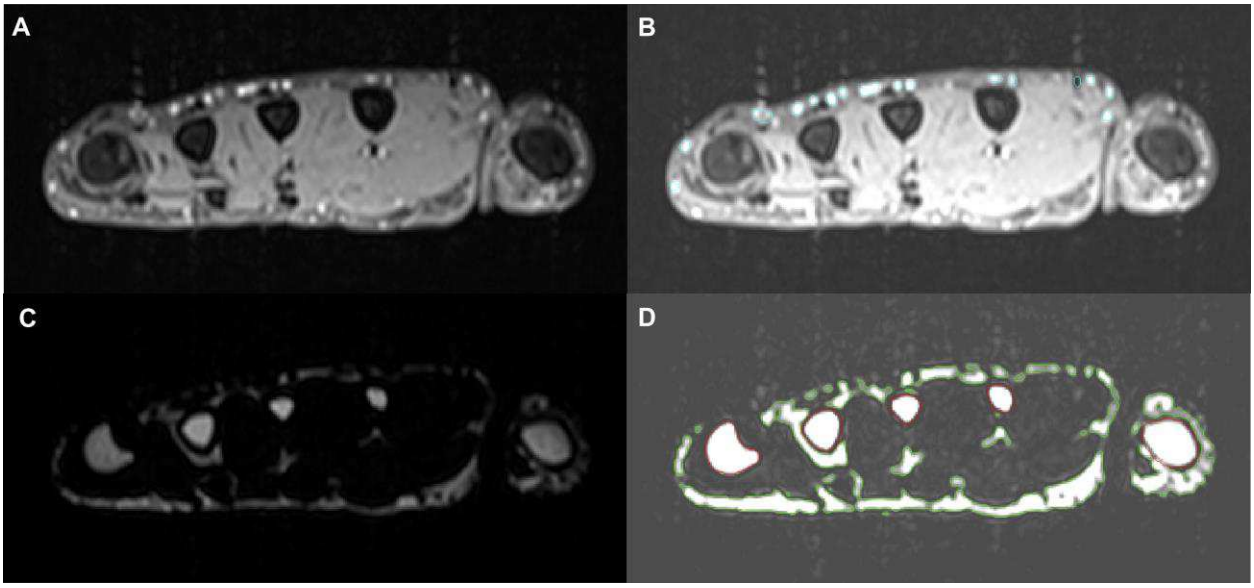


Fig. S 44. MRI structure segmentation. **a-b)** Axial water images. (a) Displayed with contrast adjusted to show 0 - 300 units. (b) Same image with a more inclusive contrast to appreciate flow and pulsation artefacts. Illustrative vessel segmentations are superimposed as cyan outlines. **c-d)** Fat image at same slice location of panels (a)-(b). (c) Display contrast as panel (a). (d) Fat image repeated with bone segmentations (red) and a selection of non-lean tissue (fat fraction exceeds 10%) after bone removal (green).

Supplementary Note 1. Empirical basis for the autofluorescence and Raman scattering trends shown in the graphical abstract

The autofluorescence and Raman scattering curves shown in the graphical abstract are schematic illustrations of general wavelength trends, not a universal quantitative model. Autofluorescence varies strongly across tissue types, therefore no single curve or crossing point can be broadly applied.

To ground these trends in empirical data, we calculated the ratio between CH-band signal intensity in liver regions of interest (autofluorescence-dominated) and fat pad regions (gonadal adipose tissue; Raman-dominated) at five excitation wavelengths (785, 892, 938, 968, and 1064 nm) using the whole-mouse Raman imaging dataset shown in Figure 2 (**Fig. S 45 a-c**). Comparing signals acquired within the same emission window at each excitation wavelength causes instrument- and absorption-related effects to cancel in the ratio, isolating autofluorescence-to-Raman contrast. This within-window comparison is particularly important in the SWIR regime, where tissue absorption by water and lipids varies strongly across the spectrum.

Since Raman intensity scales as $\frac{1}{\lambda_{exc} \cdot \lambda_{det}^3}$, where λ_{exc} is the excitation wavelength and λ_{det} is the detection wavelength corresponding to the CH-band Raman shift (~2900 cm^{-1}) at each excitation, multiplying the autofluorescence-to-Raman ratio by this factor (normalized to 785 nm) removes the Raman wavelength dependency, yielding a quantity proportional to autofluorescence intensity alone. A power law was fitted to this quantity ($y = ax^k$, $A = 8.45 \times 10^{40}$, $k = -13.98$, $R^2 = 0.99$). The $\frac{1}{\lambda_{exc} \cdot \lambda_{det}^3}$ Raman reference curve was anchored at 892 nm, the first experimentally observed wavelength at which the Raman-to-autofluorescence ratio exceeds 1 (**Figure 2 d**). The fitted parameters are tissue-specific and should not be interpreted as universal constants.

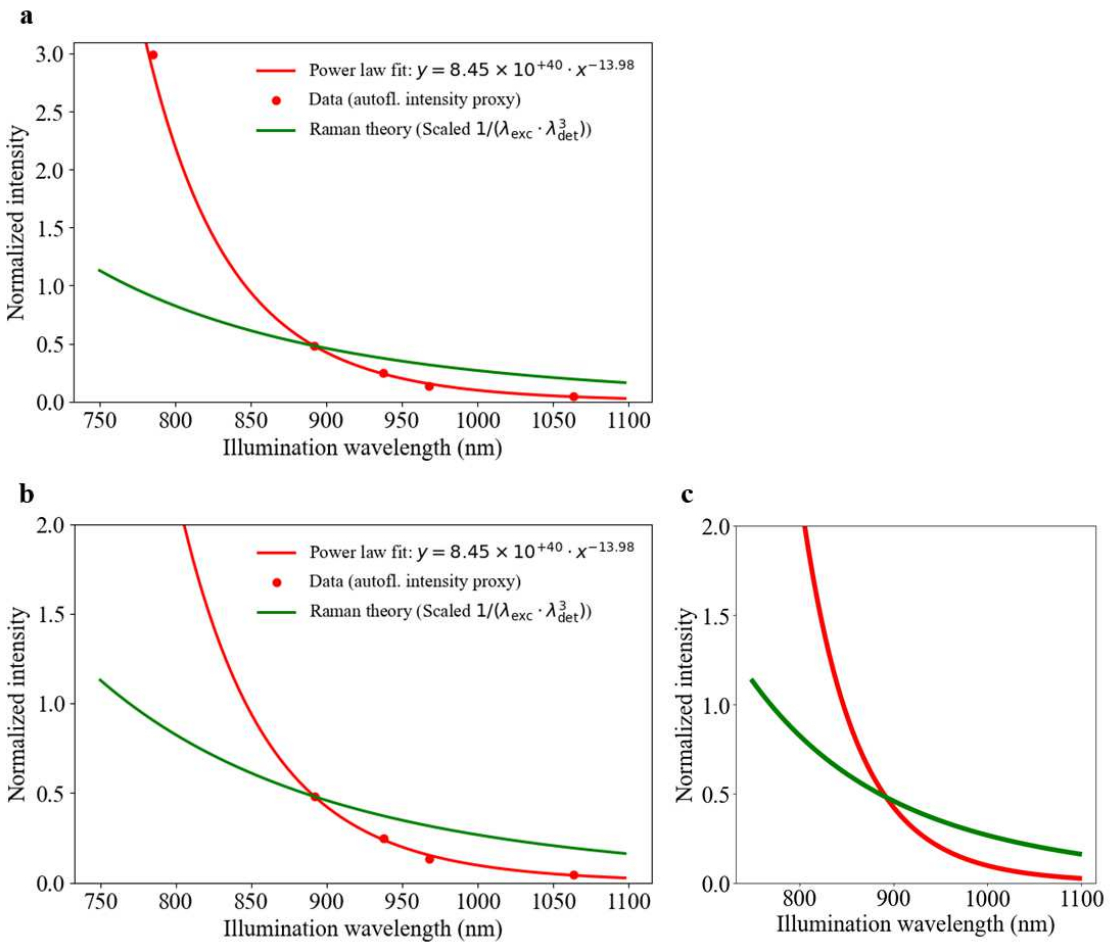


Fig. S 45. Empirical basis for the autofluorescence and Raman scattering trends shown in the graphical abstract. Red dots: autofluorescence intensity proxy derived from the liver/fat pad CH-band ratio corrected for a Raman scaling factor, where λ_{exc} is the excitation wavelength and λ_{det} is the detection wavelength of the CH Raman band (~2900 cm^{-1}). Red curve: power law fit. Green curve: $\frac{1}{\lambda_{exc} \cdot \lambda_{det}^3}$ Raman reference, anchored at 892 nm. a) Full y-axis range. b) Adjusted y-axis range. c) Both curves matched to the visual baseline of the graphical abstract schematic.

Supplementary Note 2. Biochemical basis of CH/OH contrast in SWIR Raman imaging

The contrast observed in SWIR Raman images arises from the relative contribution of CH and OH vibrational signal intensities across tissue types. Both vibrational modes are present in all biological tissues, as CH bonds are ubiquitous in lipids, proteins, and carbohydrates, while the OH signal is dominated by water and other hydroxyl-containing molecules. The resulting two-band contrast, whether visualized as a pseudocolor composite or a CH/OH ratio image, is therefore ratiometric and reflects relative biochemical composition rather than the exclusive presence of any single molecular class, as shown in our cross-modal comparison with MRI (**Fig. S 12** and **Fig. S 13**) and observations across multiple tissue types including excised organs (e.g., **Figure 4**, **Fig**. **S 5**, and **Fig. S 27**)

This interpretation is consistent with the known biochemical composition of the imaged tissues. Adipose tissue is the most lipid-rich tissue in the body, containing approximately 72-88% lipid and only 10-26% water by wet weight [66-68]. This high lipid density generates a strong, dominant CH signal, establishing adipose as the high-CH reference point in any imaging field that includes it.

Nerve tissue often contains a lipid-rich myelin sheath that contributes to the CH signal. However, the overall lipid fraction of fresh, hydrated nerves is substantially diluted by water contained within connective tissue and intra- and extracellular compartments. Human brain tissue, often regarded as the one the most lipid-rich tissues after adipose tissue, contains only ~10% lipids and ~80% water by wet weight [69,70]. Peripheral nerves exhibit a similar composition: animal studies report ~11-18% fat fraction and ~66-75% water by wet weight [71,72]. Healthy lymph nodes are likewise highly hydrated tissues, composed predominantly of water, proteins, and immune cells, with substantially lower lipid content than adipose tissue.

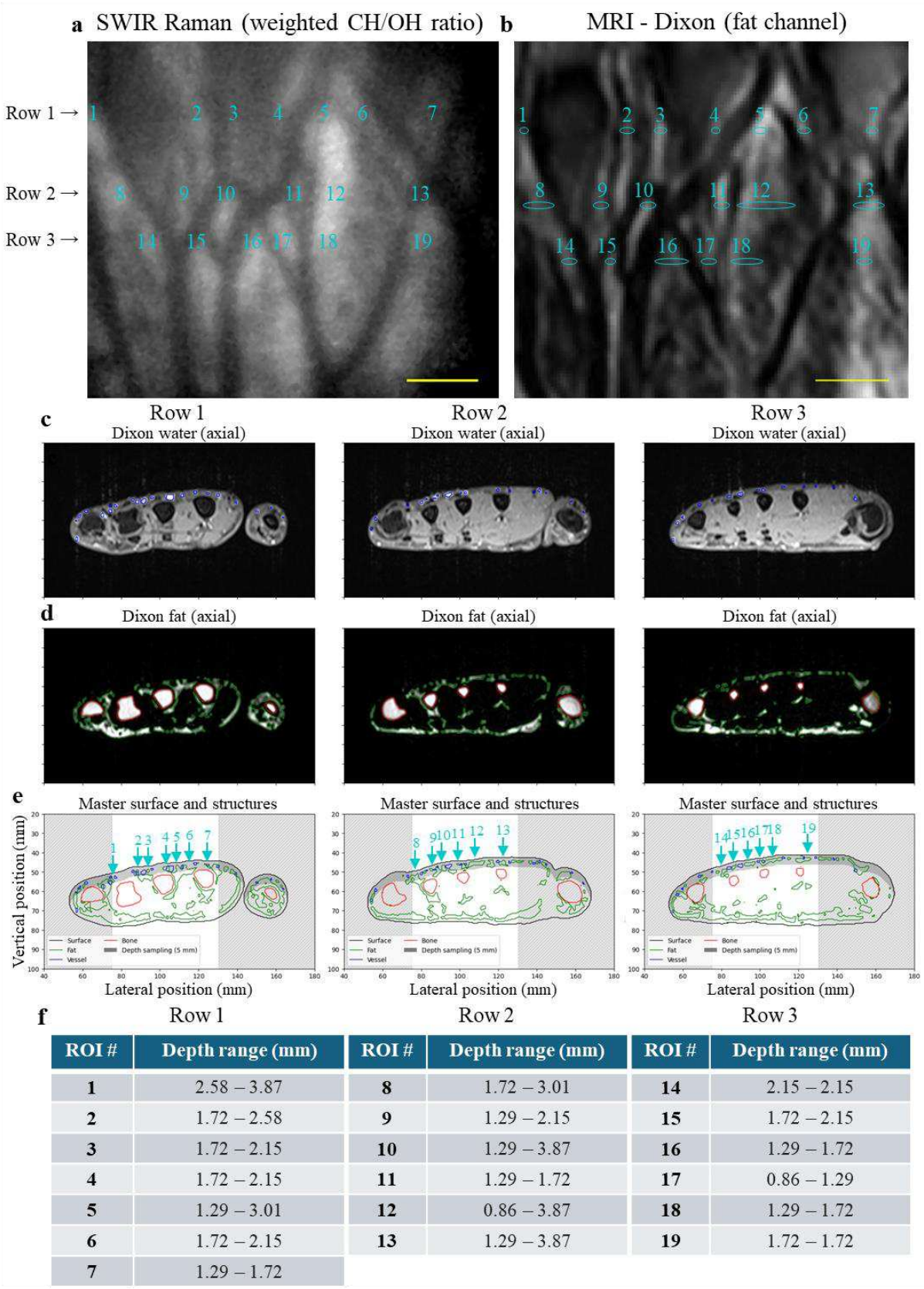
When nerves and lymph nodes are imaging within adipose-rich surgical fields, their higher water content produces elevated OH-band intensity relative to surrounding fat. Adipose tissue, conversely, contributes little OH signal while producing a strong CH response. The resulting CH/OH contrast therefore reflects these composition differences and provides a mechanistic basis for label-free tissue differentiation in SWIR Raman imaging.

Supplementary Note 3. **Depth estimation of subcutaneous fat pads**

To characterize the depth of subcutaneous fat deposits observed in the Raman images of the human hand (**Figure 1 e-f**, **Fig. S 11** and **Fig. S 12**), CH/OH-bright structures were cross-mapped to Dixon MRI fat segmentations, which provide independent anatomical localization and quantitative depth information (**Fig. S 46 a-b**).

Three axial MRI sections corresponding to transverse anatomical rows across the dorsal metacarpal region were analyzed (**Fig. S 46 c-e)**. Within each row, subcutaneous fat pads and superficial vessels were identified in the MRI fat and water images. The vessels served as shared anatomical landmarks for registration between the Raman and MRI fields of view, enabling fat deposits visible in the Raman CH/OH ratio images to be matched to their corresponding MRI structures. Minor variations in vessel orientation between the two modalities likely stem from subtle changes in hand positioning. Using this approach, 19 ROIs were identified across the three rows.

For each ROI, depth was defined as the range of depths occupied by the uppermost boundary of the corresponding fat pad across the MRI voxels lying along a transverse line through the ellipse drawn on the MRI image (**Fig. S 46 b**; voxel size: 0.43 mm). Depth was measured relative to the skin surface using the surface representation described in the Methods section. Across all 19 ROIs, the upper fat-pad boundary was located between 0.86 and 3.87 mm below the skin surface (**Fig. S 46 f**). These values represent conservative lower bounds on the imaging depth of the SWIR Raman signal: CH-band contrast is already detectable at these depths, and the true reach of the signal may extend further into tissue.



f

Row 1		Row 2		Row 3	
ROI #	**Depth range (mm)**	**ROI #**	**Depth range (mm)**	**ROI #**	**Depth range (mm)**
1	2.58 – 3.87	**8**	1.72 – 3.01	**14**	2.15 – 2.15
2	1.72 – 2.58	**9**	1.29 – 2.15	**15**	1.72 – 2.15
3	1.72 – 2.15	**10**	1.29 – 3.87	**16**	1.29 – 1.72
4	1.72 – 2.15	**11**	1.29 – 1.72	**17**	0.86 – 1.29
5	1.29 – 3.01	**12**	0.86 – 3.87	**18**	1.29 – 1.72
6	1.72 – 2.15	**13**	1.29 – 3.87	**19**	1.72 – 1.72
7	1.29 – 1.72				

Fig. S 46. MRI-guided depth localization of subcutaneous fat structures detected by SWIR Raman imaging of a human left hand. **a)** Weighted CH/OH ratio image of the dorsal hand surface, with

19 ROIs (cyan numerals) placed over regions of elevated Raman contrast corresponding to putative subcutaneous fat pads. The original SWIR Raman images were acquired using System 2 in free-run mode: 1 s per-frame exposure with a single BP1275-50 filter used for both CH (936 nm illumination at 289 mW/cm²) and OH (892 nm at 258 mW/cm²) bands. **b)** Coronal Dixon fat MRI projection of the same hand, with corresponding ROI ellipses overlaid. ROIs are arranged in three transverse rows ordered distal to proximal (row 1: ROIs 1-7; row 2: ROIs 8-13; and row 3: ROIs 14-19), corresponding to the three axial planes shown in panels (c)-(d). Minor differences in apparent vessel orientation between MRI and Raman images likely reflect small changes in hand positioning between acquisitions. **c-e)** Axial Dixon MRI sections at the three row positions. (c) Water images with surface vessel segmentation (blue). (d) Fat images with bone-excluded fat segmentation (green: fat; red: bone). (e) Anatomical contour maps derived from the segmentations in panels (c)-(d), with projected ROI locations indicated. The gray-shaded band in the contour maps denotes the 5 mm depth mark. **f)** MRI-derived depth ranges, ordered by row. ROIs 14 and 19 have identical minimum and maximum values, indicating that all enclosed voxels fell at the same depth within the resolution of the MRI acquisition. Scale bars: 1 cm.

Supplementary Note 4. Skin pigmentation as a source of autofluorescence in whole-body Raman imaging

Skin pigmentation in mice produces strong, broad NIR autofluorescence that elevates the baseline across Raman detection windows and can partially or fully suppress the Raman signal in affected regions [40]. This effect is particularly pronounced in epi-illumination geometries, where excitation light interacts with the skin surface before reaching deeper tissues, causing autofluorescence from pigmented areas to obscure Raman features originating from underlying structures.

Across our datasets, autofluorescence from most tissues decreases substantially at 892-938 nm illumination, allowing Raman contrast to dominate the detected signal (e.g. **Figure 2** and **Fig. S 27**). Pigmented skin was an exception: even at 938 nm, pigmented patches remain a major contributor to the background, preventing detection of Raman signals from underlying structures (**Fig. S 47**). This is directly visible in the silent-band images, where regions appearing darker in visible-light photographs correspond to areas of elevated silent-band autofluorescence and reduced Raman contrast. Representative emission spectra from pigmented and unpigmented skin regions further illustrate this, with pigmented regions exhibiting stronger autofluorescence under 938 nm excitation (**Fig. S 48**).

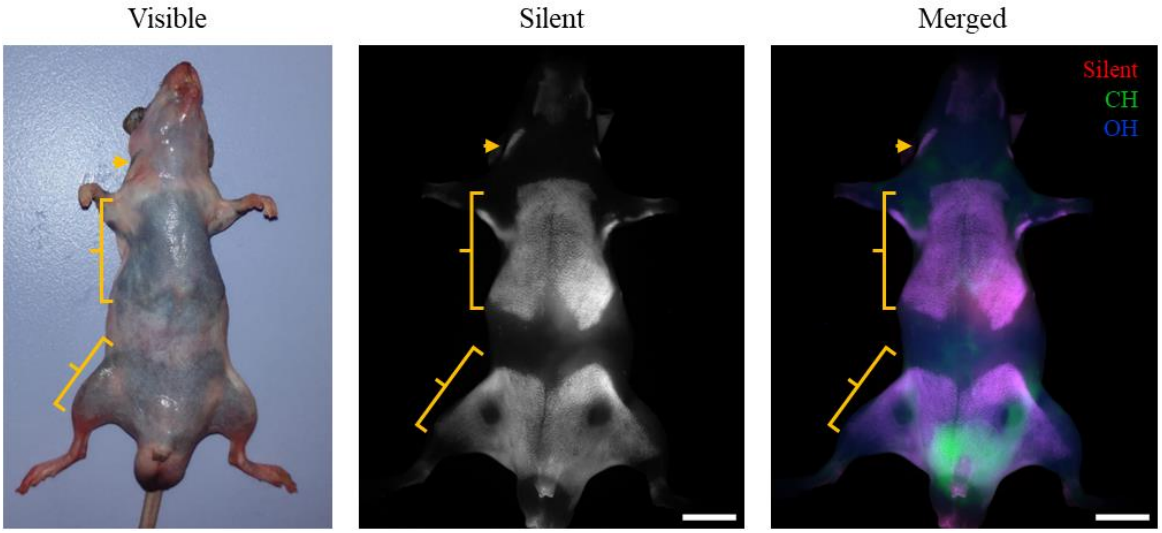


Fig. S 47. Whole-body visible and SWIR Raman images of a C57BL/6N mouse (control replicate 3 from Fig. S 21), illustrating the effect of skin pigmentation on signal detection. Pigmented regions (orange brackets and arrowhead) appear brighter in the silent-band image due to elevated autofluorescence, which affects local Raman contrast in the merged image. Illumination wavelength: 938 nm. Scale bars: 1 cm.

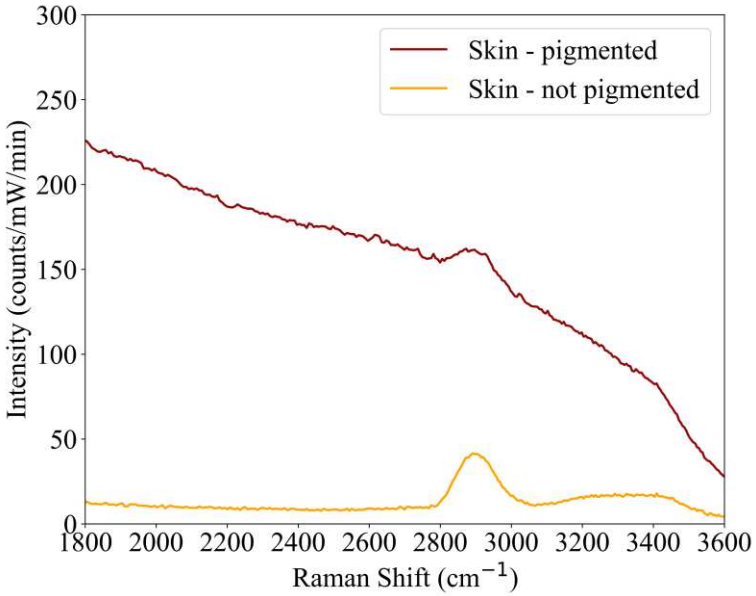


Fig. S 48. Emission spectra under 938 nm excitation from excised pigmented (dark red) and unpigmented (orange) skin regions of a C57BL/6J mouse. Pigmented skin exhibits broadband autofluorescence background that suppresses Raman signal; unpigmented skin shows clear CH and OH Raman peaks with minimal background.

This effect is most evident in the MCD diet dataset (**Fig. S 20** and **Fig. S 21**), where animals from a pigmented strain (C57BL/6N) showed variable pigmentation patterns across individuals. Where pigmented patches were present, localized autofluorescence contributed to the Raman detection bands, and ROI placement for quantitative analysis was adjusted accordingly (**Fig. S 22**). In control replicate 3, a large pigmented patch covered the chest region, precluding an ROI of identical size to the other replicates without including pigmentation-contaminated signal. The ROI was therefore placed in an unpigmented region overlying the liver and was necessarily smaller. Despite this, the extracted CH Raman values were consistent across replicates (**Figure 3 d**), confirming that liver CH contrast was reliably captured independent of ROI size. Inter-individual differences observed in whole-body images therefore reflect variation in skin pigmentation, not differences in the underlying tissue Raman response.

Hair presents an analogous surface interference: it is both highly reflective and strongly autofluorescent in the NIR [73,74], and its presence would cause CH and OH Raman signals to reflect hair composition rather than underlying tissue. When imaging furred mouse strains, hair was removed prior to imaging using depilatory cream, a standard preparation step in whole-body fluorescence imaging [20].

Finally, we note that skin pigmentation and hair are not limitations for intraoperative and *ex vivo* settings, where they are absent from the field of view.

Supplementary Note 5. Comparing measured Raman signal to expected photons

Raman scattering is an intrinsically weak effect, therefore conventional Raman microscopy compensates for this by using tightly focused laser beams (high photon flux, ~10^6-10^8 W/cm²), enabling sufficient signal collection from individual cells and subcellular structures. Our system operates in a fundamentally different regime: wide-field macroscopic illumination at low irradiance (~0.15 W/cm²) over a large field of view, with millimeter-scale sampling depths. Despite an irradiance that is 7-9 orders of magnitude lower, the interrogated volume per pixel is ~8 orders of magnitude larger, such that the total number of Raman scattering events contributing to each pixel signal is comparable.

The scale of this tradeoff can be illustrated by comparing the number of molecules contained within the respective sampling volumes. A confocal Raman system with a spot diameter of 0.5 µm and a sampling depth of 2 µm has a voxel volume of ~0.39 µm³, containing approximately 2.5×10^8 lipid molecules (assuming a lipid density of 0.9 g/cm³ and molecular weight of 860 g/mol). In contrast, although the physical camera pixel measures 20 µm × 20 µm, the imaging optics project each image pixel onto a sampling area of approximately 200 µm × 200 µm. Combined with a sampling depth of ~2 mm, this corresponds to a voxel volume of ~8×10^7 µm³ and ~5×10^{16} lipid molecules, approximately 8 orders of magnitude more molecules than the confocal sampling volume.

On a per-image-pixel basis, the wide-field system delivers approximately 0.06 mW of excitation power (0.15 W/cm² over 4×10^{-4} cm²), compared to ~10 mW in a typical confocal measurement, a difference of about two to three orders of magnitude. Each molecule therefore experiences a far lower excitation density, but the vastly larger number of molecules per pixel more than compensates: the integrated signal generation capacity (irradiance × number of molecules) is approximately 6-fold higher in the wide-field regime.

To evaluate whether the Raman signals reported in our imaging experiments are physically plausible at the detector, we calculated the Raman contribution to the measured signal at a few regions of interest (ROIs) from the dataset in **Figure 2** (**Fig. S 49**) and compared it to a simplified empirical photon-budget model.

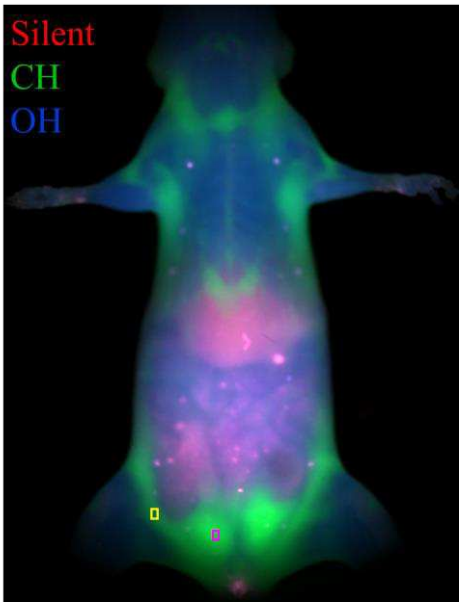


Fig. S 49. Representative 938 nm dataset showing silent (red), CH (green), and OH (blue) signals. Colored boxes indicate the ROIs used for comparison with the theoretical model in Fig. S 50: inguinal white adipose tissue (iWAT, yellow), and gonadal adipose tissue (gWAT, magenta).

Estimating the Raman signal fraction

The Raman contribution to the measured signal was estimated by decomposing the detected counts into Raman and autofluorescence components. For a given imaging band:

$$N_{image}^{Raman} = N_{image}^{(Raman+fl)} \cdot \frac{S_{Raman}}{S_{Raman} + S_{fl}}$$

where $N_{image}^{(Raman+fl)}$ denotes the measured counts in the Raman imaging band (after correction for dark, exposure time, and irradiance), and S_{Raman} and S_{fl} represent the respective Raman and autofluorescence signal contributions within the same detection band.

Using the silent band to estimate the autofluorescence background, the Raman fraction can be lower bounded as:

$$\frac{S_{Raman}}{S_{Raman} + S_{fl}} \geq \frac{N_{image}^{(Raman+fl)} - N_{image}^{(silent)} \cdot \frac{\Delta\lambda_{(Raman+fl)}}{\Delta\lambda_{(silent)}}}{N_{image}^{(Raman+fl)}}$$

where $N_{image}^{(silent)}$ is the silent band measured counts, and $\Delta\lambda_{Raman+fl}$ and $\Delta\lambda_{silent}$ are the corresponding detection bandwidths (nm). Because tissue autofluorescence generally decreases with increasing wavelength, this correction slightly overestimates the fluorescence contribution in the red-shifted Raman band, providing a conservative lower bound of the Raman fraction.

Model parameters

Our photon-budget model captures the dominant factors governing Raman signal generation and detection in the wide-field imaging system, including incident photon flux, detector quantum efficiency, gain, collection solid angle, optical transmission, molecular abundance within the sampled volume, Raman scattering cross-sections, and tissue attenuation.

The predicted Raman counts per image pixel, N_{model}, are expressed as:

$$
\begin{aligned}
N_{model} = {} & N_{ex_photons} \cdot t_{exp} \cdot A_{pixel} && \text{[Imaging setup: illumination]} \\
& \cdot \frac{QE(\lambda_{sc})}{gain} \cdot \Omega_{det} \cdot T_{optics} \cdot F_{band} && \text{[Imaging setup: detection]} \\
& \cdot N_{molecule} \cdot \frac{d\sigma}{d\Omega}(\lambda) && \text{[Raman-active molecule properties]} \\
& \cdot T_{skin}(\lambda_{ex}) \cdot T_{skin}(\lambda_{sc}) \cdot T_{tissue}(\lambda_{ex}, \lambda_{sc}) && \text{[Tissue transmission]}
\end{aligned}
$$

where:

- $N_{ex_photons} = \frac{I_{ex}\,\lambda_{ex}}{hc}$ is the number of incident photons per cm^2 per second, where I_{ex} is the excitation laser irradiance at the sample surface, $\lambda_{ex}$is the excitation wavelength, h is Planck's constant, and c is the speed of light.
- t_{exp} is the exposure time.
- A_{pixel} is the projected sample area represented by a single camera pixel.
- $QE(\lambda_{sc})$ is the detector quantum efficiency at the Raman-scattered wavelengths.
- $gain$ is the camera's photoelectron-to-count conversion factor.
- Ω_{det} is the collection solid angle.
- T_{optics} is the total optical transmittance of the imaging path.
- F_{band} is the fraction of the Raman band transmitted by the imaging filter.
- $N_{molecule}$is the number of Raman-active molecules within the effective sampling volume, calculated as

$$\frac{F_{molecule} \cdot \rho_{molecule} \cdot d_{tissue} \cdot N_A}{M_{molecule}}$$

  where $F_{molecule}$ is the mass fraction of the target molecular species, $\rho_{molecule}$ its physical density, d_{tissue} the effective sampling depth, N_A Avogadro's number, and $M_{molecule}$ the molar mass.
- $\frac{d\sigma}{d\Omega}(\lambda)$ is the differential Raman scattering cross-section per molecule (cm^2/sr), describing the probability that an incident photon is Raman-scattered into a unit solid angle.
- $T_{skin}(\lambda_{ex}), T_{skin}(\lambda_{sc})$ are the skin transmittances at the excitation and Raman-scattered wavelengths, respectively.
- $T_{tissue} = \int_0^{d_{tissue}} 10^{-[\mu_{molecule}(\lambda_{ex}) + \mu_{molecule}(\lambda_{sc})]\cdot z}\, dz$ accounts for cumulative tissue absorption at both the excitation and scattering wavelengths as a function of depth z, where $\mu_{molecule}$is the absorption coefficient (cm^{-1}) of the dominant Raman-active species (lipid or water) at wavelength λ. Scattering within the tissue is neglected in this model.

For all simulations, a standardized excitation irradiance of $I_{ex} = 1$ mW/cm² was used to match the power-density-normalized experimental dataset. Similarly, the exposure time $t_{exp} = 60$ s is a fixed factor to scale the incident photon rate to match the per-minute normalization of the data. The projected area $A_{pixel} = 4 \times 10^{-4}$ cm^2 corresponds to an effective sampling area of 200 µm × 200 µm, which accounts for the 20 µm physical pixel size and the system magnification. Additional model parameters were: $gain = 7.79$, specified by the manufacturer's characterization; $\Omega_{det} = 5.65 \times 10^{-3}$, defined by the Ø25.4 mm camera lens diameter located 300 mm from the sample; and $T_{optics} \approx 0.91$, corresponding to four filters at 99% transmission each and one lens at 95% transmission. The detector $QE(\lambda_{sc})$ followed the manufacturer's specifications.

For the CH band, $F_{band} = 1$. For the OH band, $F_{band} = 0.2$ to account for partial transmission of the broader OH stretching band.

For adipose tissue CH-band measurements, the lipid parameters were $F_{lipid} = 0.8$ (lipid mass fraction in adipose tissue), $\rho_{lipid} = 0.9$ g/cm^3, $M_{lipid} \approx 860$ g/mol (representative molar mass of a mammalian adipose triglyceride). Effective sampling depths were $d_{tissue} = 0.2$ cm for inguinal white adipose tissue (iWAT) and $d_{tissue} = 0.6$ cm for gonadal white adipose tissue (gWAT). For OH-band measurements in muscle tissue, $F_{water} = 0.7$, $\rho_{water} = 1.0$ g/cm^3, $M_{water} = 18$ g/mol, and $d_{tissue} = 0.2$ cm were used.

Skin transmittance was estimated using the Kubelka-Munk photon transport model, based on transmittance and reflectance measurements of BALB/c female mouse skin (thickness 0.52 mm) reported by Sabino et al. [75] over the 700-1400 nm range. Absorption and reduced scattering coefficients were derived from these data. For wavelengths above 800 nm, the absorption coefficient was modeled as a weighted sum of 70% water, 20% lipid, and 10% collagen absorption coefficients, plus a slowly decaying baseline ($\propto \lambda^{-0.4}$, 2.4 cm^{-1} at 700 nm, 1.7 cm^{-1} at 1600 nm). Absorption spectra were taken from published sources for water [76], collagen [77], and lipid [78,79]. The reduced scattering coefficient was fitted to a power-law function ($\mu_s'(\lambda) = a\lambda^b$, where $b = -1.54$). These parameters were then used to recalculate skin transmittance over 700-1600 nm using the Kubelka-Munk model, yielding good agreement with the Sabino et al. [75] values within the measured wavelength range. Raman scattering originating from the skin itself was neglected.

Model calibration and comparison with experimental data

The differential Raman scattering cross-section for the CH bands at 785 nm was determined by calibrating the model to the experimentally measured signal from gWAT. This yielded $\frac{d\sigma}{d\Omega}(\lambda = 785\ nm) = 6.2 \times 10^{-29}$ cm²/sr per molecule, consistent with literature values reported for high-wavenumber CH stretching modes [80]. Cross-sections at other wavelengths were scaled according to $\frac{d\sigma}{d\Omega} \propto \frac{1}{\lambda_{ex}\lambda_{sc}^3}$. For the OH band, a differential cross-section of $\frac{d\sigma}{d\Omega}(\lambda = 532\ nm) = 5.74 \times 10^{-30}$ cm²/sr per molecule was obtained from a standard 90° scattering reference [81] and scaled using the same $\frac{d\sigma}{d\Omega} \propto \frac{1}{\lambda_{ex}\lambda_{sc}^3}$ wavelength dependence.

Using these parameters, the model predicts Raman count levels that are in quantitative agreement with the experimentally measured signals in both CH and OH Raman band analysis (**Fig. S 50**). In both cases, the spectral trend follows the expected $\frac{1}{\lambda_{ex}\lambda_{sc}^3}$ dependence, modulated by wavelength-dependent tissue absorption and detector response. Overall, the model reproduced both the magnitude and wavelength dependence of the measured counts, indicating that the detected signals are consistent with physical expectations.

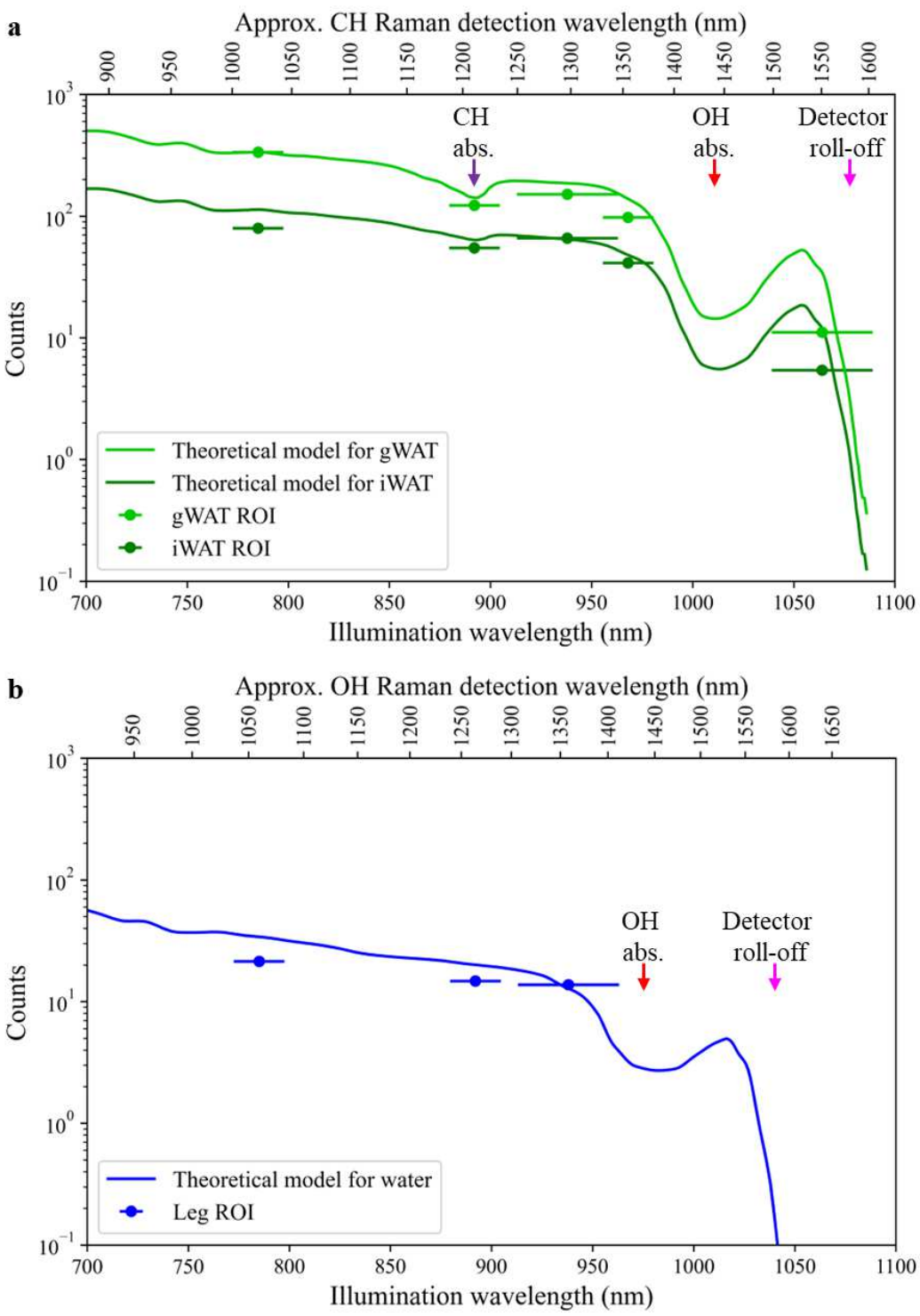


Fig. S 50. Photon budget model for CH and OH Raman signals. **a)** Measured Raman counts (dots) from gonadal white adipose tissue (gWAT, light green) and inguinal white adipose tissue (iWAT, dark green) ROIs shown in Fig. S 49 as a function of illumination wavelength (bottom axis) and approximate corresponding detection wavelength for the CH Raman shift (top axis; converted from 2950 cm^{-1}). Solid lines show the theoretical photon budget model for each ROI. The model is calibrated to experimental gWAT data at 785 nm using a baseline cross-section of $\mathbf{6.2 \times 10^{-29}}$

cm²/sr per molecule; all other wavelengths are scaled according to the $\frac{1}{\lambda_{ex}\lambda_{sc}^3}$ relationship. The higher count levels in gWAT relative to iWAT reflect the greater effective sampling depth (0.6 cm vs. 0.2 cm). **b)** Measured Raman counts (blue dots) from a leg ROI as a function of illumination wavelength and approximate corresponding detection wavelength for the OH Raman shift (top axis; converted from 3300 cm^{-1}), with the corresponding theoretical model (solid blue line) for muscle tissue. The OH cross-section is anchored to literature values at 532 nm ($\mathbf{5.74 \times 10^{-30}}$ cm²/sr per molecule) and follows the same wavelength-scaling framework from panel (a) with the same $\frac{1}{\lambda_{ex}\lambda_{sc}^3}$ scaling applied. Annotations indicate the CH absorption feature (~1210 nm, purple arrow), OH absorption feature (~1440 nm, red arrow), and InGaAs detector roll-off (~1575 nm, magenta arrow). Error bars represent the spectral bandwidth of the filters used for imaging data acquisition.

Supplementary Movies

Supplementary Movie 1. Awake mouse imaging. Green: CH; blue: OH. Acquired at 1 fps; played at 1 fps (original speed). Scale bar: 1 cm.

Supplementary Movie 2. Porcine neck lymph node resection. Green: CH; blue: OH. Acquired at 1 fps; played at 1 fps (original speed). Scale bar: 1 cm.

Supplementary Movie 3. Porcine neck lymph node resection. Green: CH; blue: OH. Acquired at 1 fps; played at 10 fps (10x speed). Scale bar: 1 cm.

Supplementary Movie 4. Intraoperative resection of mesenteric lymph nodes in a living pig. Green: CH; blue: OH. Acquired at 1 fps; played at 1 fps (original speed). Scale bar: 1 cm.

Supplementary Movie 5. Intraoperative resection of mesenteric lymph nodes in a living pig. Green: CH; blue: OH. Acquired at 1 fps; played at 10 fps (10x speed). Scale bar: 1 cm.

Supplementary Movie 6. Intraoperative resection of an inguinal lymph node in a human body donor. Green: CH; blue: OH. Acquired at 1 fps; played at 1 fps (original speed). Scale bar: 1 cm.

Supplementary Movie 7. Intraoperative resection of an inguinal lymph node in a human body donor. Green: CH; blue: OH. Acquired at 1 fps; played at 10 fps (10x speed). Scale bar: 1 cm.

Supplementary References

20 Saif, M. *et al.* Non-invasive monitoring of chronic liver disease via near-infrared and shortwave-infrared imaging of endogenous lipofuscin. *Nat Biomed Eng* **4**, 801-813 (2020). https://doi.org/10.1038/s41551-020-0569-y

40 del Rosal, B., Thomas, G., Mahadevan-Jansen, A. & Stoddart, P. R. in *Near Infrared-Emitting Nanoparticles for Biomedical Applications* (eds Antonio Benayas, Eva Hemmer, Guosong Hong, & Daniel Jaque) 21-47 (Springer International Publishing, 2020).

42 International Commission on Non-Ionizing Radiation, P. ICNIRP Guidelines on Limits of Exposure to Laser Radiation of Wavelengths between 180 nm and 1,000 mum. *Health Phys* **105**, 271-295 (2013). https://doi.org/10.1097/HP.0b013e3182983fd4

64 Wang, Y. L. Noise-induced systematic errors in ratio imaging: serious artefacts and correction with multi-resolution denoising. *J Microsc* **228**, 123-131 (2007). https://doi.org/10.1111/j.1365-2818.2007.01834.x

65 Dixon, W. T. Simple proton spectroscopic imaging. *Radiology* **153**, 189-194 (1984). https://doi.org/10.1148/radiology.153.1.6089263

66 Thomas, L. W. The chemical composition of adipose tissue of man and mice. *Q J Exp Physiol Cogn Med Sci* **47**, 179-188 (1962). https://doi.org/10.1113/expphysiol.1962.sp001589

67 Baker, G. L. Human adipose tissue composition and age. *Am J Clin Nutr* **22**, 829-835 (1969). https://doi.org/10.1093/ajcn/22.7.829

68 Wang, J. & Pierson, R. N., Jr. Disparate hydration of adipose and lean tissue require a new model for body water distribution in man. *J Nutr* **106**, 1687-1693 (1976). https://doi.org/10.1093/jn/106.12.1687

69 Reinoso, R. F., Telfer, B. A. & Rowland, M. Tissue water content in rats measured by desiccation. *J Pharmacol Toxicol Methods* **38**, 87-92 (1997). https://doi.org/10.1016/s1056-8719(97)00053-1

70 O'Brien, J. S. & Sampson, E. L. Lipid composition of the normal human brain: gray matter, white matter, and myelin. *J Lipid Res* **6**, 537-544 (1965).

71 Finean, J. B. The role of water in the structure of peripheral nerve myelin. *J Biophys Biochem Cytol* **3**, 95-102 (1957). https://doi.org/10.1083/jcb.3.1.95

72 Wadhwani, K. C. *et al.* Prevention of nerve edema and increased blood-nerve barrier permeability-surface area product in galactosemic rats by aldose reductase or thromboxane synthetase inhibitors. *Diabetes* **38**, 1469-1477 (1989). https://doi.org/10.2337/diab.38.11.1469

73 Del Rosal, B., Villa, I., Jaque, D. & Sanz-Rodriguez, F. In vivo autofluorescence in the biological windows: the role of pigmentation. *Journal of biophotonics* **9**, 1059-1067 (2016). https://doi.org/10.1002/jbio.201500271

74 Huang, Z. *et al.* Cutaneous melanin exhibiting fluorescence emission under near-infrared light excitation. *J Biomed Opt* **11**, 34010 (2006). https://doi.org/10.1117/1.2204007

75 Sabino, C. P. *et al.* The optical properties of mouse skin in the visible and near infrared spectral regions. *J Photochem Photobiol B* **160**, 72-78 (2016). https://doi.org/10.1016/j.jphotobiol.2016.03.047

76 Palmer, K. F. & Williams, D. Optical properties of water in the near infrared. *J Opt Soc Am* **64**, 1107-1110 (1974). https://doi.org/10.1364/JOSA.64.001107

77 Sekar, S. K. *et al.* Diffuse optical characterization of collagen absorption from 500 to 1700 nm. *J Biomed Opt* **22**, 15006 (2017). https://doi.org/10.1117/1.JBO.22.1.015006

78 van Veen, R. L. *et al.* Determination of visible near-IR absorption coefficients of mammalian fat using time- and spatially resolved diffuse reflectance and transmission spectroscopy. *J Biomed Opt* **10**, 054004 (2005). https://doi.org/10.1117/1.2085149

79 Nachabe, R. *et al.* Estimation of lipid and water concentrations in scattering media with diffuse optical spectroscopy from 900 to 1,600 nm. *J Biomed Opt* **15**, 037015 (2010). https://doi.org/10.1117/1.3454392

80 McCreery, R. L. in *Raman Spectroscopy for Chemical Analysis* 15-33 (2000).

81 Bray, A., Chapman, R. & Plakhotnik, T. Accurate measurements of the Raman scattering coefficient and the depolarization ratio in liquid water. *Applied optics* **52**, 2503-2510 (2013). https://doi.org/10.1364/AO.52.002503

Supplementary Files

This is a list of supplementary files associated with this preprint. Click to download.

- Suppl.Video1awakemouse1fps.mp4
- Suppl.Video2neckLN1fps.mp4
- Suppl.Video3neckLN10fps.mp4
- Suppl.Video6bodydonor1fps.mp4
- Suppl.Video7bodydonor10fps.mp4
- Suppl.Video4alivemesenteryLN1fps.mp4
- Suppl.Video5alivemesenteryLN10fps.mp4